



Kaluza-Klein Dark Matter Search with the IceCube Neutrino Detector

TECHNISCHE UNIVERSITÄT, MÜNCHEN
LEHRSTUHL E17

Matthias Danninger

Christchurch/Munich 2008



Abstract

Stable weakly interacting massive particles (WIMPs) that are remnants from the ‘hot Big Bang’ are the most promising constituent for a possible solution of the dark matter problem. An attractive WIMP candidate, the lightest Kaluza-Klein particle (LKP), is motivated by theories of universal extra dimensions, following the fundamental pioneering work of Kaluza and Klein. LKPs scatter off nuclei in large celestial bodies, for example the Sun, and become trapped within their deep gravitational wells, leading to high WIMP densities in the object’s core. Pair-wise LKP annihilations are expected to lead to highly energetic neutrino productions, and therefore to a detectable neutrino flux component from the centre of the Sun in the neutrino telescope IceCube. This thesis investigates the possibility to detect muons, created in neutrino interactions in the ice, from LKP annihilations in the core of the Sun with the combined detector array 2007, consisting of AMANDA-II and IceCube22-string. Studies are done with intensive Monte Carlo simulations that are verified against a subset of the total available experimental data from 2007. The expected sensitivity for the detector livetime of 60 days is calculated for the composed LKP neutrino flux, consisting of seven different annihilation channels. Furthermore, a competitive sensitivity, compared to existing direct and indirect search experiments, at the 90% upper confidence level on the spin-dependent cross section of the LKP on protons is calculated.

Contents

Abstract	i
1 Introduction	1
2 Dark Matter and Kaluza-Klein Dark Matter (KK-DM)	5
2.1 Energy and Matter Densities in the Universe	5
2.2 Dark Matter Problem	6
2.3 Extra Dimensions and KK-DM	9
2.3.1 Concept of Universal Extra Dimensions	10
2.3.2 Kaluza-Klein Dark Matter	10
3 Indirect Solar Search for Kaluza-Klein Dark Matter	15
3.1 Accumulation in the Sun	15
3.2 Annihilation of LKP and resulting Neutrinos	16
4 Detection of High Energy Neutrinos	19
4.1 Neutrino-Nucleon Interactions	19
4.2 Čerenkov Radiation	22
4.3 Energy losses of Muons in Ice	22
5 The Combined Detector 2007	25
5.1 From Amanda to IceCube	25
5.1.1 Optical Modules	26
5.1.2 Data Acquisition	29
5.2 Background	31
5.2.1 Atmospheric Muons	31
5.2.2 Atmospheric Neutrinos	32
5.2.3 Solar Neutrinos	32
5.2.4 Galactic Neutrinos	32
5.2.5 Cosmological Neutrinos, GZK Effect	32
5.2.6 Point Source Neutrinos	33
6 Simulation and Reconstruction Methods	35
6.1 Monte Carlo Simulation	35
6.1.1 LKP Signal	38

6.1.2	Muon Background	42
6.1.3	Neutrino Background	42
6.2	Reconstruction Methods	43
6.2.1	First Guess	44
6.2.2	Likelihood Reconstruction	45
6.3	Data Sets	46
7	Analysis	53
7.1	Comparison with Experiment (MC vs Exp)	54
7.2	Cut Selections	54
7.2.1	L0 + L1: First Selection	54
7.2.2	L2: Cut in Solar Region	61
7.2.3	L3: Horizontal Selection	63
7.2.4	L4: Multivariant Background Rejection	64
7.2.5	L5: Solar Search Cone	66
7.3	Sensitivity	70
7.4	Systematics	72
8	Results and Discussion	77
8.1	Comparison to Direct Search Experiments	78
8.2	Comparison to Neutralino Search	80
8.3	Further Optimisations for KK-DM Indirect Search	81
	Summary	85
	Acknowledgements	87
	List of Figures	87
	List of Tables	90
	A Additional Masses	93
	B Good Run List 2007	97
	Bibliography	98
	Statement	105

Chapter 1

Introduction

AUGUST 1956

NEUTRINO FOUND— "A long and exciting adventure in physics has come to a triumphant end. The neutrino has been found. Frederick Reines and Clyde L. Cowan, Jr., of the Los Alamos Scientific Laboratory trapped the ghostly particle in an underground chamber near the Savannah River atomic pile. Phillip Morrison, in the January issue of Scientific American, compared the neutrino to the planet Neptune. The discovery of Neptune was a crowning achievement of classical physics: the motions of other planets showed it had to be there. The neutrino is a similar achievement of modern physics, and its discovery is a vindication of the law of the conservation of energy." [1]

More than 50 years later, physicist are still constantly challenged by the ‘ghostly particle’, only this time there are no doubts about its existence. In various physics research fields like quantum field theory, theoretical particle physics, and theories of universal extra dimensions, the neutrino offers the best chance for experimental proof of new theoretical models beyond the current standard. Enrico Fermi coined the name neutrino meaning ‘little neutral one’, describing the delicate interaction behaviour of neutrinos. Until the 1990s, the neutrino was thought to be a massless particle like the photon. However, more recent observations of neutrino oscillations among their three different flavor states are theoretically explained by finite mass eigenstates, attributing neutrinos a small but finite mass after all. Because of their unique interaction behaviours – neutrinos have no electric charge and hence, interact with other particles only through the weak nuclear force and gravity – they pass through matter virtually unhindered and can therefore be used in high energy astro-particle physics as a carrier of information from distant astrophysical sources to Earth, in order to gain more profound understanding of the most ‘violent’ and peculiar objects in our universe, like black holes, active galactic nuclei, super nova remnants or ultra massive stars, where neutrinos are produced in decays and annihilations of particles. Unlike cosmic protons or other charged particles, neutrinos are not deflected by magnetic fields and compared to photons, they do not scatter and get absorbed in interstellar clouds. Furthermore, neutrinos could be the key

to a solution of the cosmological dark matter problem, favouring a non-baryonic weakly interacting massive particle (WIMP) as the main constituent. These stable heavy particles, with masses ranging from several GeV/c^2 to a few TeV/c^2 , can be gravitationally trapped within massive objects like the Sun, accumulating to high densities, exceeding the mean galactic density by several orders of magnitude in the object's core. A detection of a WIMP induced neutrino signal at energies above the GeV threshold would strongly indicate the existence of dark matter of a WIMP origin and extend our current understanding of the universe.

Neutrinos interact with ordinary matter only weakly through the neutral current and charged current reactions. At high energy scales, the cross sections for these reactions are extremely low and detection is only possible through secondary particles. In order to detect cosmic neutrinos at a sufficiently high rate, Giga ton under-water or under-ice Čerenkov detectors are the most promising solution. Currently the largest neutrino telescope is embedded deep in the East Antarctic Ice Sheet at the geographical South Pole, close to the Amundsen-Scott station, and consists of the old AMANDA-II and the partially constructed IceCube detector array. In 2010, the completed combined detector will consist of more than 5700 optical modules, instrumenting a detector volume of 1 km^3 .

This thesis studies the feasibility of using the combined AMANDA-II and IceCube 22 string detector for an indirect solar search for the lightest Kaluza-Klein particle (LKP), arising from theories of universal extra dimensions. LKPs are theoretically motivated as a viable WIMP, and therefore dark matter candidate, in chapter 2. The method of indirect solar search with neutrino telescopes for LKPs is introduced and verified in chapter 3. Chapter 4 details the physics behind neutrino detection with neutrino telescopes in ice and the combined detector 2007 is described in chapter 5. Elaboration of the Monte Carlo simulations of the detector response and reconstruction algorithms are given in chapter 6. Preliminary comparison of the simulated datasets with experimental data from the 2007 detector are described early in chapter 7, followed by the individual analysis steps, reducing the atmospheric background and optimising the LKP signal to background ratio in the individual cut levels. Furthermore, the sensitivity of the combined detector 2007 for a LKP induced muon flux at the 90% upper confidence level is calculated. As the theory of universal extra dimensions has very few open parameters, and consequently the properties of the LKPs are accurately predicted, a sensitivity on the spin-dependent LKP-on-proton cross section can be derived and is discussed in comparison to other ongoing and future direct search experiments. Chapter 8 describes further optimisation and a comparison with respect to recently published neutralino results. A future plan to continue the analysis is presented in the final outlook section and appendix A.

It doesn't matter how beautiful your theory is,
it doesn't matter how smart you are.
If it doesn't agree with experiment, it's wrong.

Richard P. Feynman

Chapter 2

Dark Matter and Kaluza-Klein Dark Matter (KK-DM)

This chapter introduces the well known dark matter problem in the universe by looking at past and present observations, which ultimately constrain the allowed regions for matter and energy densities in the universe. By means of the observed energy density values, potential dark matter candidates are introduced, in particular weakly interacting massive particles that are motivated by theories of universal extra dimensions.

2.1 Energy and Matter Densities in the Universe

In a cosmological model, Einstein's equations describe the relation between the curvature of spacetime and matter sources. In other words, ignoring the cosmological constant, Λ , the Einstein tensor, $G_{\mu\nu}$ ¹, in equation 2.1, describing the geometry of the Universe, is determined by the energy-momentum tensor, $T_{\mu\nu}$, defined by the Universe's energy and mass content.

$$R_{\mu\nu} - \frac{1}{2}g_{\mu\nu}R + \Lambda g_{\mu\nu} = \kappa T_{\mu\nu} \quad , \quad G_{\mu\nu} = R_{\mu\nu} - \frac{1}{2}g_{\mu\nu}R \quad (2.1)$$

Einstein originally introduced Λ to obtain linearity in the field equations and to get a non-expanding solution. The discovery of an accelerating expansion of the Universe by recent type Ia supernova observations [2] links the cosmological constant with an extra repulsive force, called 'vacuum' or 'dark' energy, which contributes as a source of gravitation fields even in the absence of matter [3]. This so called standard model of cosmology is considered as the underlying theory of cosmology throughout the thesis. There exist however, other recently published models, entirely based on general relativity and the observed matter distribution in the universe that can explain the supernova observations [2] without resorting to dark energy [4]. Cosmological theories assume in general that all rods and clocks across the universe are calibrated

¹ $R_{\mu\nu}$ being the Ricci Tensor and R the Ricci Scalar

identically. The proposed model [5], takes into account the observer's own position within this lumpy universe in order to interpret cosmological distance and time measurements differently.

In order to make predictions for average mass densities a metric is defined, describing the symmetries of the problem. Measurements of the Cosmic Microwave Background (CMB) [6] show that the Universe is isotropic and homogeneous on large scales. Therefore the metric can be expressed in the Robertson-Walker form,

$$ds^2 = -dt^2 + a^2(t) \left[\frac{dr^2}{1 - kr^2} + r^2 d\Omega^2 \right] , \quad k = -1, 0, 1 \quad (2.2)$$

with the scalar factor $a(t)$. Choosing the constant k , denoting the spatial curvature, to be zero, an expression for the critical energy density, ρ_c , in a flat Universe can be derived [7]

$$\rho_c = \frac{3H^2}{8\pi G_N} , \quad (2.3)$$

where the expansion rate of the Universe, H , is the Hubble parameter and G_N is Newton's constant. This allows any energy density, Ω_i , contributing to the total energy of the Universe, Ω (matter or energy), to be expressed in terms of ρ_c ,

$$\Omega_i = \frac{\rho_i}{\rho_c} \quad \text{with} \quad \Omega = \sum_i \Omega_i . \quad (2.4)$$

2.2 Dark Matter Problem

The first indication of large quantities of 'unseen' or dark mass in the halo of galaxies was given by Fritz Zwicky as early as 1933 [8]. He observed that the orbital velocity, v , of objects outside the central region did not follow the expected spectrum derived from Kepler's 3rd law and the visible matter distribution,

$$G_N M(r) = v^2 r \quad \rightarrow \quad v = \sqrt{\frac{G_N M(r)}{r}} \quad (2.5)$$

where $M(r)$ is the mass interior to r .

Figure 2.1, shows a more recent measurement of the orbital velocity distribution. The graph 'disk', taking into account only luminous matter, shows a velocity proportional to $1/\sqrt{r}$ beyond the optical disk. The characteristic flat behaviour of the observed curve, which is equivalent to a constant $v(r)$, implies the existence of a halo with a mass distribution following $M(r) \propto r$ and $\rho \propto 1/r^2$. Observations of our galaxy indicate that dark matter (DM) extends in significant concentrations to the Magellanic Clouds. In addition, gravitational micro lensing of stars in the Magellanic Clouds by the gravitational fields of massive compact halo objects (MACHOS) in between, provides evidence of another form of non-luminous matter. Strict limits

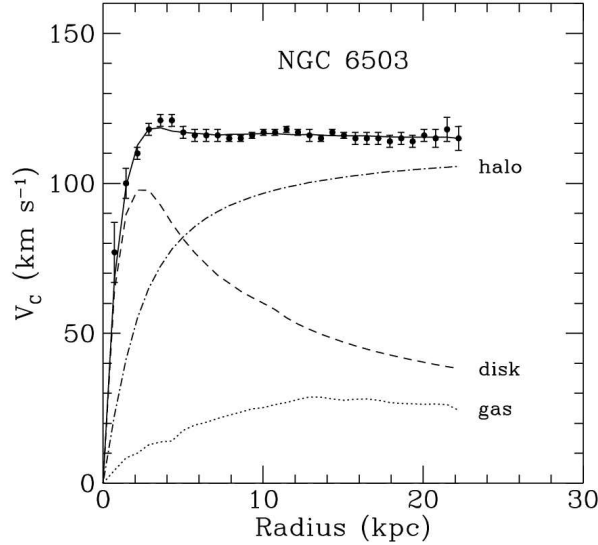


Figure 2.1: *Different contributions to the rotation curve of the NGC 6503 galaxy of visible matter (disk), gas and dark matter (halo) [9].*

on the baryonic density in the Universe are set by the theory of Big Bang nucleosynthesis [10]. Therefore, compact objects like MACHOS or non-illuminated gas clouds can only make up a very small fraction of dark matter. Consequently, the observed orbital velocity spectrum in figure 2.1 cannot be explained by ordinary matter. Although Standard Model neutrinos undoubtedly contribute to dark matter, they are no longer favoured as a dominant dark matter component. Due to their extremely small mass, calculations of the total neutrino relic density show that neutrinos are simply not abundant enough and their maximal contribution to the total energy density ($\Omega_\nu = 0.03_{-0.015}^{+0.015}$) is similar to Ω_b [3].

Following the notation introduced in equation 2.4, the total energy density in the Universe derived from the combined results of WMAP and SDSS LRG [11] is $\Omega = 1.003_{-0.009}^{+0.010}$. This indicates an almost spatially flat Universe with a dark energy content of $\Omega_\Lambda = 0.761_{-0.018}^{+0.017}$ and a total matter density of $\Omega_m = 0.239_{-0.018}^{+0.018}$. Figure 2.2 shows the allowed regions of Ω_m and the fraction of baryonic matter density $\Omega_b = 0.0416_{-0.018}^{+0.019}$ according to [11].

The dark matter density is found as $\Omega_{DM} = 0.197_{-0.015}^{+0.016}$ and is therefore almost five times larger than the density of ordinary matter. Hitherto, the Standard Model (SM) of particle physics cannot provide a viable dark matter candidate. As a consequence, a whole zoo of possible dark matter particles have been introduced in models beyond the SM. They can be divided into hot, warm and cold dark matter, according to the speed of the particles at decoupling. Structure formation of the Universe, studied in numerical N-Body simulations, favour non-relativistic, e.g., cold particles, removing relativistic (hot) and semi-relativistic (warm) dark matter as preferred candidates [12]. The most promising dark matter candidates are Weakly

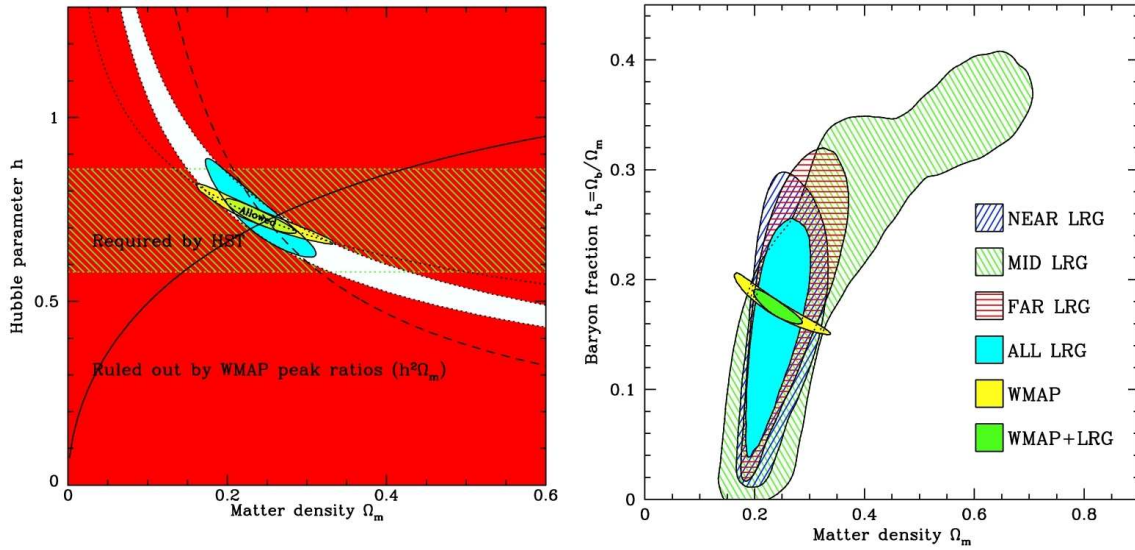


Figure 2.2: Both graphs display the allowed regions for Ω_m derived from the combined results of WMAP and SDSS LRG [11]. On the left side with respect to the Hubble parameter $h = H_0/100\text{kms}^{-1}\text{Mpc}^{-1}$ and on the right in terms of the baryon fraction f_b .

Interacting Massive Particles (WIMPs), which carry no electrical charge and interact only weakly and gravitationally with matter. As products of the hot Big Bang, WIMPs require a lifetime longer than the current age of the Universe and the maximum energy must not exceed the over closure limit of 50 TeV. Constraints at the lower end of the energy spectrum are set by the most recent collider experiments. The most studied WIMP candidate, the neutralino, χ , is introduced by the Minimal Supersymmetric extension of the Standard Model (MSSM). This thesis however, focuses on the Lightest Kaluza-Klein Particle (LKP), introduced in section 2.3.2, which is predicted by theories of Universal Extra Dimensions (UED) (see section 2.3.1).

Calculations of particle dynamics in the early universe can determine whether the predicted WIMPs have a high enough relic abundance in the present universe. Assuming the existence of theoretically motivated WIMPs, their relic density has to be within the observed DM density $\Omega_{DM} = 0.197^{+0.016}_{-0.015}$. Following the calculations of [7], the Boltzmann equation for the particle number density n_{LKP} of the LKP is given by,

$$\frac{dn_{LKP}}{dt} + 3Hn_{LKP} = -\langle\sigma v\rangle \left(n_{LKP}^2 - (n_{LKP}^{eq})^2 \right) \quad (2.6)$$

with $\langle\sigma v\rangle$ being the thermally averaged total annihilation cross section multiplied by the relative velocity. The number density, n_{LKP}^{eq} , at thermal equilibrium for a temperature, T , is given in the non-relativistic limit for massive LKPs with mass

m_{LKP} , using the Maxwell-Boltzmann approximation

$$n_{LKP}^{eq} = g_{LKP} \left(\frac{m_{LKP} T}{2\pi} \right)^{3/2} e^{-m_{LKP}/T} , \quad (2.7)$$

where g_{LKP} is the number of internal degrees of freedom of the LKP. In order to rewrite equation 2.6 in terms of the entropy density in the universe, s , the variables Y and Y^{eq} are introduced,

$$Y_{LKP} \equiv \frac{n_{LKP}}{s} , \quad Y_{LKP}^{eq} \equiv \frac{n_{LKP}^{eq}}{s} \text{ with } s \propto T^3 . \quad (2.8)$$

At temperatures of $T \sim 10^1 - 10^3$ GeV, when the LKPs are beginning to no longer be in thermal equilibrium with the expanding Universe, equation 2.6 is dominated by the expansion rate, H , and annihilation processes into lighter particles are beginning to exceed the number of LKP creations. After the interaction rate, Γ , of the LKP drops below H , annihilation processes freeze out completely. Using the conservation of entropy per comoving volume, sa^3 , equation 2.6 is expressed in terms of the variables from equation 2.8,

$$s\dot{Y}_{LKP} = -\langle\sigma v\rangle s^2 \left(Y_{LKP}^2 - (Y_{LKP}^{eq})^2 \right) , \quad (2.9)$$

with the time derivative \dot{Y}_{LKP} . An analytical solution in two time regions, corresponding to long before freeze-out and long after freeze-out, allows one to express the matter density of LKPs in terms of the critical density of a spatially flat Universe ρ_c

$$\Omega_{LKP} h^2 \approx \frac{3 \times 10^{-27}}{\langle\sigma v\rangle} cm^3 s^{-1} \quad (2.10)$$

$$\langle\sigma v\rangle \approx \frac{1.7 \times 10^{-26}}{m_{LKP}^2 (TeV)} cm^3 s^{-1} . \quad (2.11)$$

Thus, with the total annihilation cross section for the LKPs [13] of equation 2.11, the DM density for the LKP relics in terms of the Hubble parameter, h , is calculated to be $\Omega_{LKP} h^2 \approx 0.17$. This is within good approximation of $\Omega_{DM} h^2 \approx 0.105$ given by [11]. The calculation holds for WIMPs in general, but is here explicitly shown for the case of LKPs, in order to demonstrate that it is a viable DM candidate.

2.3 Extra Dimensions and KK-DM

Our every day world appears to consist of three space dimensions and one time dimension, the 3+1 space-time. The first approach to extend this dimensionality was done by Kaluza [14] and Klein [15], proposing that a unification of electrodynamics and gravitation could be described by a single five dimensional gravitational theory. Based on that concept, various models have been suggested, with possible extra dimensions appearing at higher energy scales.

2.3.1 Concept of Universal Extra Dimensions

In the framework of extra dimensions, the ordinary $3 + 1$ space-time is referred to as the brane, which is embedded in a higher-dimensional $3 + \delta + 1$ space-time called the bulk. There are strong phenomenological motivations, like dynamical electroweak symmetry breaking (EWSB) [16], to have all gauge fields propagating in the bulk. This scenario, with compactified, spatially flat, extra dimensions is called the Universal Extra Dimensions (UED) scenario. The additional compactified dimensions are finite and have periodic boundary conditions. It is shown in [16] that, in the case of one extra dimension, the constraint on the compactification scale is given by $R^{-1} > 300$ GeV, where R is the compactification radius². The main motivation for using the theory of UED in this thesis is the prediction of the LKP as a potential WIMP candidate (section 2.3.2). UED has a relatively small number of free parameters to describe the introduced WIMP, compared to the MSSM model. The most essential parameter is the mass, given by the inverse of the compactification scale R at tree level.

2.3.2 Kaluza-Klein Dark Matter

An example of a class of particles arising from compactified dimensions are ‘pyrgons’ [18]. Pyrgon is the Greek word for ladder or tower, which characterises the particles, in general called KK-particles. Assuming there are KK excitations of SM particles, it is shown in the following that the expected spectrum of particles yields viable DM candidates. A simple example is the case of one circular extra dimension with radius R where a massless quantum field $A(x)$, propagating in the circular extra dimension, determined by R , can also be regarded as a 4-dimensional theory with a tower of mass eigenstates $m_n = n/R$ at tree level. More precisely, $A(x)$ depends on $x = (\mathbf{x}, \mathbf{y})$, where $\mathbf{x} = (x_0, x_1, x_2, x_3)$ is the normal 4-dimensional space-time and \mathbf{y} is the extra dimensional coordinate. Due to the circular shape of the extra dimension, the periodic boundary condition for the \mathbf{y} -coordinate can be expressed as $\mathbf{y} \rightarrow \mathbf{y} + 2\pi R$. Consequently, the field $A(x)$ appears in a set of Fourier expanded modes, which are called KK-states,

$$A(x) = \sum_{n=-\infty}^{\infty} A^{(n)}(\mathbf{x}) e^{i\frac{n\cdot\mathbf{y}}{R}} \quad \text{with } n \in Z; \quad (2.12)$$

The 4-dimensional fields $A^{(n)}(\mathbf{x})$ are the corresponding KK-modes with n being the KK-excitation number. The zero-mode field $A^{(0)}(\mathbf{x})$ corresponds to the usual 4-dimensional state of the SM particles. The extra dimension affects possible observation by an appearance of the same SM particle with different masses, associated with KK-states of increasing mass [19].

The exponential term in equation 2.12 can be identified with a $U(1)$ symmetry in the brane. Thus, the momentum $p \equiv n/R$ is quantised in the extra dimension

²The term radius used in the literature for spatially-flat extra dimensions is misleading. One can regard this as the length of the compactified dimension

and n becomes a good quantum number, the KK-number [17]. This can be also expressed in terms of UED, where the first excitation of KK-particles is,

$$m_{KK}^2 = \frac{1}{R^2} + m_{SM}^2 \quad (2.13)$$

with the mass of the zero-level KK-mode of the SM particle m_{SM} . This indicates a high degree of degeneracy for light SM particles at tree level and the first KK-excitation would not be stable. However, [20] calculates two corrections at loop level and indicates that these radiative corrections can by far exceed the tree level contributions.

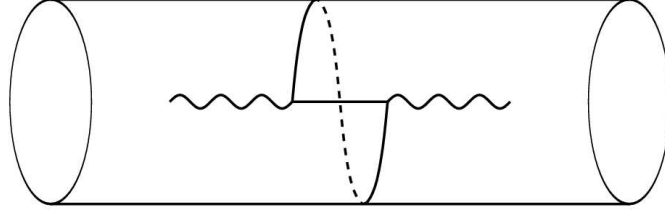


Figure 2.3: *Loop violating Lorentz Invariance in 5 dimensions.* The wavy line on the surface of the cylinder at each side of the loop, represents a particle propagating in ordinary $3 + 1$ space-time. By propagating in the extra dimension (loop), it can be clearly seen that the starting and the finishing point of the loop do not overlap and Lorentz Invariance is therefore violated. [20]

Firstly, additional kinetic terms appear because of the boundary conditions of the compactified extra dimension. The second contribution, explained further in figure 2.3, comes from the violation of the Lorentz Invariance in five dimensions at loop level. This correction results from particles traversing from one side of the finite orbifold to the other. These radiative corrections shift the KK-modes away from their tree level expectations. As a consequence, KK-number conservation breaks and changes to KK-parity conservation ($P_{KK} = (-1)^n$ for the n^{th} KK-mode [17]). [21] motivates an electrically neutral and non-baryonic particle as the most suitable LKP. Therefore, the most promising DM-candidates in UED are given by the first KK-excitations of the neutral gauge bosons, which are an analogue to the SM photon and Z boson. In consensus with enunciating the SM, where EWSB induces mixing between the gauge eigenstates of the gauge bosons B and W , the mass matrix in UED in the $(B^{(n)}, W_3^{(n)})$ basis for the n^{th} excitation can be written as ([17]):

$$\begin{pmatrix} \frac{n^2}{R^2} + \frac{1}{4}g_1^2v^2 + \delta M_1^2 & \frac{1}{4}g_1g_2v^2 \\ \frac{1}{4}g_1g_2v^2 & \frac{n^2}{R^2} + \frac{1}{4}g_2^2v^2 + \delta M_2^2 \end{pmatrix} \quad (2.14)$$

g_1 and g_2 are the $U(1)$ and $SU(2)$ gauge couplings and δM_1^2 and δM_2^2 the radiative corrections to the $B^{(1)}$ and $W^{(1)}$ masses. $v \approx 174$ GeV is the Higgs vacuum expectation value (VEV). In this notation, the SM neutral gauge bosons (γ, Z)

can be described by the mass matrix in the $(B^{(0)}, W_3^{(0)})$ basis. Hence, the mixing angle between the KK gauge bosons is the Weinberg angle, if one neglects the radiative corrections δM_1^2 and δM_2^2 . The LKP is introduced in [21] in the limit of $\delta M_2^2 - \delta M_1^2 \gg g_1 g_2 v^2$, which minimises the mixing angle and maximises the diagonal entries in the mass matrix. Thus, the LKP is stable under decay and expected to consist of entirely $B^{(1)}$. Its coupling to the SM fermions is given by g_1 , and is therefore proportional to the fermion's hypercharge.

The calculation of the relic LKP density, presented in section 2.2, assumes only one particle, the lightest possible SM particle in the first KK-mode, to accredit for the final DM density. This is a good approximation, but too inaccurate to constrain the allowed mass region for the LKPs with recent observations. Therefore, the calculation of the relic density has to be extended to also account for coannihilations. This is especially relevant for the case of particles with masses only slightly greater than $m_{B^{(1)}}$. These particles have an abundance very similar to $n_{B^{(1)}}^{eq}(T)$ in the hot Big Bang, and their freeze out temperatures lie within the same order. Therefore, any relic abundance of higher order will eventually decay into the ground state $B^{(1)}$ and contribute towards the total relic abundance of LKPs. Figure 2.4 takes into account coannihilations with the first excitation of the right-handed electron $e_r^{(1)}$ and links LKP masses with corresponding predictions of $\Omega_{B^{(1)}} h^2$, in order to become an allowed mass region for the LKP. The possible search window of the allowed masses $m_{B^{(1)}}$ is determined by Figure 2.4 and is used further in this thesis. It is the basis for the three sets of simulated signals at 500 GeV/c², 750 GeV/c², and 1000 GeV/c² (see section 6.1).

$$500 \text{ GeV}c^{-2} < m_{B^{(1)}} < 1000 \text{ GeV}c^{-2} . \quad (2.15)$$

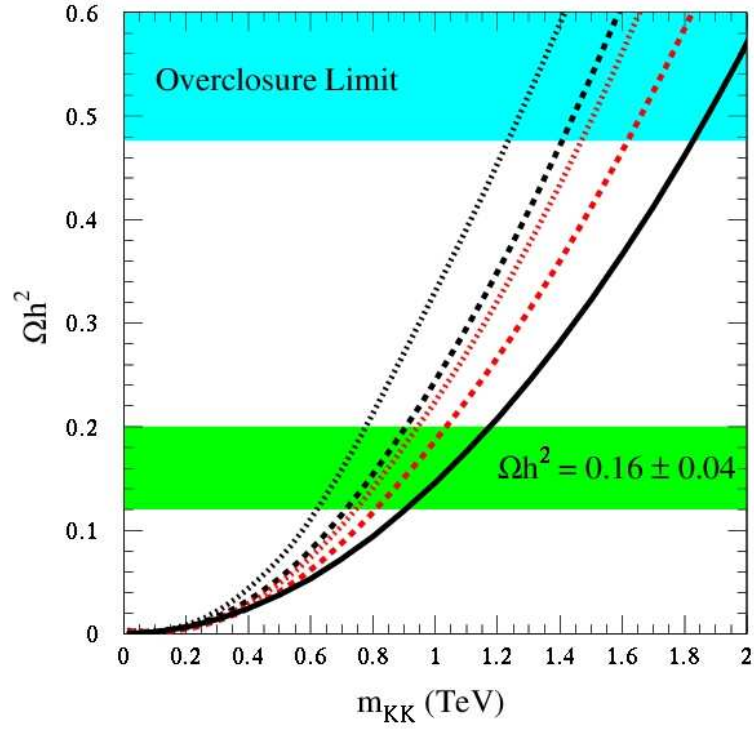


Figure 2.4: Allowed regions for $m_{B^{(1)}}$, here denoted as m_{KK} in TeV with respect to the predicted values for $\Omega_{B^{(1)}}h^2$. The solid line is for the case $B^{(1)}$ only, whereas the dashed (one flavour) and dotted (three flavours) lines also consider coannihilations of the nearly degenerate $e_r^{(1)}$. This is displayed for two relative mass differences $\Delta = 0.01$ (red) and $\Delta = 0.05$ (black) with $\Delta = (m_{e_r^{(1)}} - m_{LKP})/m_{LKP}$. From [21]

Chapter 3

Indirect Solar Search for Kaluza-Klein Dark Matter

Assuming that the local DM-density in our galaxy is about $\rho_{local} = 0.3 \text{ GeV/cm}^3$ [17], each litre of our Milky Way would contain on an average approximately 0.4 $B^{(1)}$ particles. While travelling through the galaxy, the LKPs can scatter off nuclei in stars or planets and become trapped within their deep gravitational wells. Once trapped within such a gravitational potential the LKP's trajectory is similar to that of a comet. Each successive scattering process results in a loss of energy and the LKP gradually describes trajectories closer and closer to the object's core. Thus, the LKPs can be expected to accumulate in the core of the object to densities that exceed ρ_{local} by several orders of magnitude (see section 3.1). The principle of an indirect search demands a relatively highly efficient annihilation of LKPs into detectable particles on Earth. A solar search, performed with neutrino telescopes, like IceCube [22] or Antares [23], looks for an enhanced $\nu_\mu \bar{\nu}_\mu$ flux out of the core of the Sun, which arises from LKP annihilations.

3.1 Accumulation in the Sun

In the case of our solar system, LKPs can scatter via two different processes off nuclei in the sun. One is the spin-independent interaction with contributions from the spin-independent component of the $B^{(1)}$ -on-proton elastic scattering cross section and the $B^{(1)}$ -on-helium elastic scattering cross section. The composed spin-independent capture rate, C_{SI}^\odot , is found to be three to four orders of magnitude smaller than the spin-dependent capture rate, C_{SD}^\odot , in equation 3.1, accounting for the spin-dependent component of the $B^{(1)}$ -on-proton elastic scattering [24]

$$C_{SD}^\odot \simeq 3.35 \times 10^{18} s^{-1} \left(\frac{\rho_{local}}{0.3 \frac{GeV}{cm^3}} \right) \left(\frac{270 \frac{km}{s}}{\bar{v}_{local}} \right)^3 \left(\frac{\sigma_{H,SD}}{10^{-6} pb} \right) \left(\frac{1000 GeV}{m_{B^{(1)}}} \right)^2, \quad (3.1)$$

with the spin-dependent elastic scattering-cross section, $\sigma_{H,SD}$, for $B^{(1)}$ -on-hydrogen, \bar{v}_{local} the root mean square (rms) of the local velocity of dark matter in the halo, and $m_{B^{(1)}}$ the mass of the LKP particle. The solar accretion is largely dominated by the spin-dependent capture rate, C_{SD}^\odot . Therefore, the spin-independent process is ignored in further calculations. The annihilation cross section times the relative $B^{(1)}$ velocity (v) per volume, A^\odot , is given in equation 3.2, where the effective core volume of the sun for LKP, V_{eff} , is approximated by matching the sun's temperature with the gravitational potential energy of one LKP at the core radius [24],

$$A^\odot = \frac{\langle \sigma v \rangle}{V_{eff}} . \quad (3.2)$$

In order to reach equilibrium between the annihilation rate, Γ_A , and the capture rate, C_{SD}^\odot , the relative number of LKPs, N , has to remain constant. Therefore the rate of change of this number, \dot{N} , given in equation 3.3 has to be zero,

$$\dot{N} = C_{SD}^\odot - A^\odot N^2 \stackrel{!}{=} 0 . \quad (3.3)$$

The present annihilation rate, Γ_A , is given by [24] as,

$$\Gamma_A = \frac{1}{2} A^\odot N^2 = \frac{1}{2} C_{SD}^\odot \cdot \tanh^2 \left(t_\odot \sqrt{A^\odot C_{SD}^\odot} \right) \quad (3.4)$$

where $t_\odot = 4.5$ billion years is the age of our solar system. In order to fulfill equation 3.3, the hyperbolic tangent in equation 3.4 is required to be equal to one. Thus, in order to reach equilibrium between the annihilation rate and capture rate of LKPs in the sun the following relation has to be valid:

$$t_\odot \sqrt{A^\odot C_{SD}^\odot} \gg 1 \quad (3.5)$$

For $m_{B^{(1)}}$ within the range obtained in equation 2.15, relation 3.5 can be confirmed, and hereafter it is assumed that the sun either reaches or nearly reaches the above described equilibrium. [25].

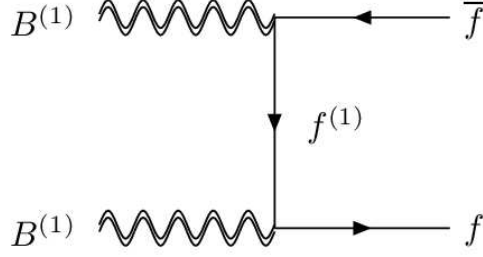
3.2 Annihilation of LKP and resulting Neutrinos

The pair annihilation of $B^{(1)}$ in ordinary matter must preserve momentum and all involved symmetries, expressed in the conservation of quantum numbers, in the same way as SM particles. The KK-Parity, P_{KK} , introduced in section 2.3.2, arises as an additional symmetry. Any SM particle ψ_{SM} has the following eigenvalue,

$$P_{KK} |\psi_{SM}\rangle = 1 |\psi_{SM}\rangle \quad (3.6)$$

whereas

$$P_{KK} |\psi_{B^{(1)}}\rangle = -1 |\psi_{B^{(1)}}\rangle . \quad (3.7)$$

Figure 3.1: Feynman diagram for the $B^{(1)}B^{(1)}$ annihilation

The Feynman diagram describing the $B^{(1)}B^{(1)}$ annihilation process in the sun is shown in figure 3.1. The total $P_{KK} = (-1)(-1) = 1 \cdot 1$ is equal to one for the initial and the final states. Hence, the annihilation is allowed, and for $f\bar{f}$ being any fermion combination from table 3.1, it also accounts for all possible annihilation channels¹. In the good approximation that all heavier KK-modes have the same mass, the relative branching ratios are determined only by the hypercharges of the final fermion states [25]. Neutrinos are the only particles that are able to leave the

	Annihilation Process	Branching ratio
$B^{(1)}B^{(1)}$	$\rightarrow (16)\nu_e\bar{\nu}_e, (17)\nu_\mu\bar{\nu}_\mu, (18)\nu_\tau\bar{\nu}_\tau$	0.012
	$\rightarrow e^+e^-, \mu^+\mu^-, (4)\tau^+\tau^-$	0.20
	$\rightarrow u\bar{u}, (1)c\bar{c}, (3)t\bar{t}$	0.11
	$\rightarrow d\bar{d}, s\bar{s}, (2)b\bar{b}$	0.07
	$\rightarrow \phi\phi^*$	0.023

Table 3.1: Possible channels for the pair annihilation of $B^{(1)}B^{(1)}$ and branching ratios of the final states. Investigated channels are indicated by their individual channel number. Numbers for the branching ratios are from [25].

sun without being completely absorbed. Thus, the direct neutrino channels provide a definite source of monochromatic neutrinos, along with the very short lived particles, which form a secondary source of neutrinos when decaying. Annihilation products, like the combination of $u\bar{u}$, lose too much energy from scattering before decaying to be relevant. Although, short lived particles ($b\bar{b}$, $t\bar{t}$ and $c\bar{c}$) contribute toward the generated neutrino flux, their energy spectrum is broadened and usually referred to as a ‘soft’ spectrum.

Charged current (CC) interactions with the solar medium are the dominant processes that reduce the flux of neutrinos from the core of the sun by LKP annihilations. Muon and electron neutrinos, reacting with the protons in the sun, create

¹The $\phi\phi^*$ channel is neglected in this analysis, due to its small branching ratio but high degree of uncertainty in the mass.

electrons and muons that are instantaneously absorbed. Taus, produced in CC reactions of tau neutrinos, decay again into a tau neutrino of less energy, conserving the original number of generated tau neutrinos. The probability of neutrinos escaping the sun rises significantly for lower energies [25]. Additionally, $\nu_\mu \leftrightarrow \nu_\tau$ oscillation randomises an outgoing muon or tau neutrino flux sufficiently, so an average of both components is observed at the detector [24]. Electron neutrino components, due to oscillation, occur only at energies much lower than the investigated energies.

In summary of all the obtained results and assumptions from chapters 2 and 3, the simulated $\nu_\mu \bar{\nu}_\mu$ spectra, further used in this analysis, and explained in detail in section 6.1, of all chosen annihilation channels, are displayed in figure 3.2 for a LKP mass of $m_{B^{(1)}} = 1000$ GeV.

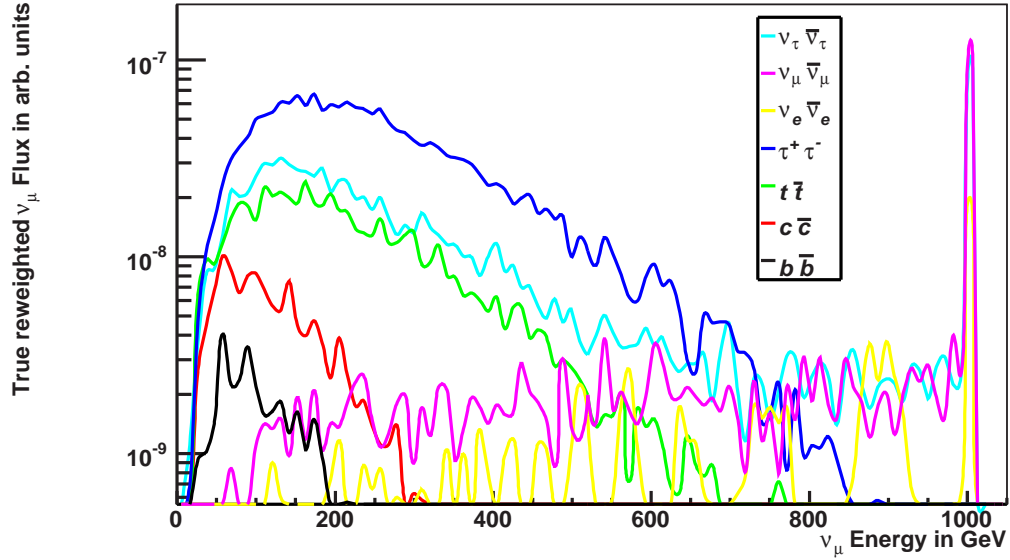


Figure 3.2: The simulated $\nu_\mu \bar{\nu}_\mu$ spectra (neutrinos that actually trigger the detector) resulting from $B^{(1)} B^{(1)}$ ($m_{B^{(1)}} = 1000$ GeV) annihilations in the core of the sun for each channel chosen for this analysis. The characteristic monochromatic peak of the direct neutrino channels is clearly visible, as well as the ‘soft’ spectra of the secondary sources. For details on the simulated signals, see section 6.1.

Chapter 4

Detection of High Energy Neutrinos

Very low fluxes of high-energy neutrinos can only be observed in extremely large detectors called neutrino telescopes, which use a large instrumented detector volume. At the time of this thesis, neutrinos emitted by cosmic point sources and galactic neutrino fluxes in general, have not been positively distinguished from atmospheric neutrino events. IceCube (2010) will use a full cubic kilometer of Antarctic ice as an open detector media, detecting the Čerenkov light radiated by passing charged leptons that are produced in charge current interactions with nuclei inside or close to the detector.

4.1 Neutrino-Nucleon Interactions

Neutrinos interact with nuclei in the ice, predominantly protons from the hydrogen atoms, through two different channels. The charged current interaction (CC) and the neutral current (NC) interaction are summarised in the following equations:

$$\nu_l(\bar{\nu}_l) + N \rightarrow l^-(l^+) + X \quad (CC) \quad (4.1)$$

$$\nu_l(\bar{\nu}_l) + N \rightarrow \nu'_l(\bar{\nu}'_l) + X \quad (NC) \quad (4.2)$$

N is the initial nucleus and X the final hadronic remains of the nucleus, usually a hadronic cascade, also called a hadronic shower. The NC interaction occurs through the exchange of the neutral Z boson, and can in fact be regarded as a scattering of the initial neutrino on the nucleus N . Hadronic showers can result in detectable charged leptons at high energies, but do not contribute at the targeted energies of this study of $10^1 \text{ GeV} \sim 10^3 \text{ GeV}$. This also applies to the hadronic cascades, X , produced in the CC interaction, where charged W bosons are exchanged. Both processes are summarised in the Feynman diagrams of figure 4.1.

Of all charged leptons produced, only the muons and anti muons travel through the detector medium for up to several kilometres, radiating Čerenkov light (see section 4.2). Electrons, roughly 200 times lighter than muons, typically lose their energy in electromagnetic showers within a few metres in ice, which makes them only detectable at energies far above the GeV range. Produced tau leptons decay

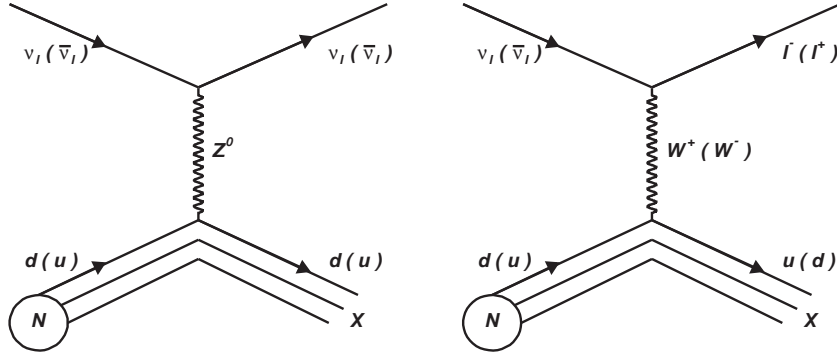


Figure 4.1: The left Feynman diagram illustrates the NC interaction of $\nu_l(\bar{\nu}_l)$ of all flavours with a nucleon N . The right Feynman diagram stands for the CC interaction, creating a charged lepton $l^-(l^+)$. In both diagrams, X , is the final hadronic remains of N .

with a very short lifetime of less than 1 ps into the following secondary particles [26]:

$$\tau^-(\tau^+) \rightarrow X + \nu_\tau(\bar{\nu}_\tau) \quad (4.3)$$

$$\rightarrow \nu_\tau(\bar{\nu}_\tau) + \bar{\nu}_e(\nu_e) + e^-(e^+) \quad (4.4)$$

$$\rightarrow \nu_\tau(\bar{\nu}_\tau) + \bar{\nu}_\mu(\nu_\mu) + \mu^-(\mu^+) \quad (4.5)$$

While muons are produced in the third channel, such tau events are neglected, as only a small fraction of the kinetic energy is transferred to the muon produced via equation 4.5. Hence, the μ^+ and μ^- created in CC interactions from $\bar{\nu}_\mu(\nu_\mu)$ are the only particles considered in this analysis to trigger the detector.

The CC interaction is a deep inelastic scattering process of neutrinos of energy E_ν with a nucleus, N , of mass M_N . This is expressed in the double differential cross section in equations [27],

$$\frac{d^2\sigma_{\nu N}^{CC}}{dx dy} = \frac{2 \cdot G_F^2 M_N E_\nu}{\pi} \cdot \left(\frac{M_W^2}{Q^2 + M_W^2} \right)^2 \cdot [xq(x, Q^2) + x(1-y)^2 \bar{q}(x, Q^2)] \quad (4.6)$$

$$\frac{d^2\sigma_{\bar{\nu} N}^{CC}}{dx dy} = \frac{2 \cdot G_F^2 M_N E_\nu}{\pi} \cdot \left(\frac{M_W^2}{Q^2 + M_W^2} \right)^2 \cdot [x(1-y)^2 q(x, Q^2) + x\bar{q}(x, Q^2)] \quad (4.7)$$

Here, $q(x, Q^2)$ and $\bar{q}(x, Q^2)$ are the parton distribution functions for the quarks and antiquarks depending on the momentum transfer Q^2 . x and y are the Bjorken scaling variables defined in equation 4.8. M_W is the W boson mass and G_F is the Fermi constant.

$$x = \frac{Q^2}{2 \cdot M_N \cdot (E_\nu - E_\mu)} \quad y = \frac{E_\nu - E_\mu}{E_\nu} \quad (4.8)$$

The variable x is the fraction of the momentum of the nucleus carried by the quark and y is the fraction of neutrino energy transferred to the quark. Both scaling variables determine the degree of inelasticity of the interaction. Equations 4.6 and 4.7 differ only in their dependence on y in the quark and anti quark parton functions. At low energies, where the parton functions are dominated by the valence quarks, the deep inelastic neutrino cross section for scattering on protons in Antarctic ice is two to three times larger for the neutrino than for the antineutrino. This is due to helicity suppression of the anti neutrino reaction. In the center of mass (CM) frame, in the limit of $y = 1$, the projection of the total angular momentum along the direction of the anti neutrino's momentum is equal to 1 for the initial states of the anti neutrino reaction. The produced μ^+ is emitted backwards with respect to the initial direction of the anti neutrino's momentum, whereas the momentum of the produced quark is aligned parallel. Therefore, the projection of the total angular momentum of the final states onto the initial anti neutrino momentum is -1 . This flip of the angular momentum is forbidden and the situation is illustrated in figure 4.2. It is easy to see that in the case of the neutrino CC interaction, the projection of the total angular momentum on the neutrino's momentum is conserved. As a result, the case of $y \neq 1$, the CC interaction of the anti neutrino is suppressed by a factor $(1 - y)^2$ for energies below ~ 10 TeV [7]. At very high energies, the cross section is no longer dominated by the valence quarks but by the sea quarks, which are always produced in $q\bar{q}$ pairs. Consequently, both cross sections become equal.

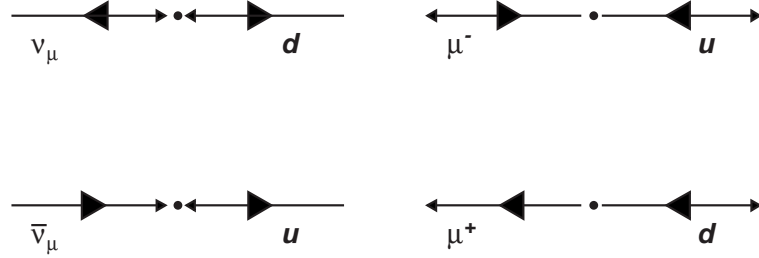


Figure 4.2: This figure illustrates helicity suppression in the $\bar{\nu}_\mu$ CC interaction with N in the limit of $y = 1$. The thin and thick arrows represent, respectively, momentum and spin of the particles. The two top diagrams show the situation in the CM frame for the ν_μ case, where the total angular momentum of the initial states (left) is equal the total angular momentum of the final states (right), which is equal zero. In the lower two diagrams, the situation is shown for the $\bar{\nu}_\mu$ CC interaction, where the total angular momentum for initial (1) (left) has to flip to (-1) (with respect to the CM frame), and is therefore forbidden.

The mean angle between the initial neutrino and the muon path (see equation 4.9) is approximated to be less than 1° for the targeted energy range [28]. Thus, the

directional information of the initial neutrino is well retained.

$$\langle \Theta_{\nu\mu}^2 \rangle \approx \frac{0.7^\circ}{(E_\nu/TeV)^{0.7}} \quad (4.9)$$

4.2 Čerenkov Radiation

The Čerenkov effect occurs when a charged particle travels through a medium with speed, v , higher than the speed of light in that particular medium, i.e., when $v > c/n$ (n is the index of refraction of the medium). Charged particles like the produced leptons polarise the surrounded medium. Due to a particle speed being above the speed of light, the polarisation is anisotropic along the velocity axis. Therefore the emitted moving light cone is shaped like a Mach cone. The cone front has an opening angle, Θ , with the velocity axis, which is energy dependent [29].

$$\cos \Theta_{H^2O} = \frac{c_M}{\nu} = \frac{1}{n(\lambda) \cdot \beta} \quad (4.10)$$

At targeted energies (ultra relativistic limit $\beta = 1$) the opening angle of the cone in water or frozen water (ice) is $\Theta_{H^2O} = 41.2^\circ$, having to first order a constant refracting index of $n = 1.33$ for the visible electromagnetic spectrum. The effect is slightly wavelength dependent and rises with shorter wavelengths, which is why the emission maximum is in the blue at a wavelength of around 475 nm. The number of photons, N_{vis} , emitted due to the Čerenkov effect by a particle of charge ($z \cdot e$), can be estimated with the Frank-Tamm expression, which is given in equation 4.11 per unit wavelength and unit length [30],

$$\frac{d^2 N_{vis}}{dx d\lambda} = \frac{2\pi z^2 \alpha}{\lambda^2} \left(1 - \frac{1}{\beta^2 n^2(\lambda)} \right) . \quad (4.11)$$

Here, $\alpha = 1/137$ is the fine structure constant. A characteristic value for the number of photons emitted by a muon, derived by integrating equation 4.11 over the sensitive range [300nm,600nm] of the photo multiplier tubes (PMT), is 332 per cm track length. This corresponds to an average energy loss due to Čerenkov radiation of ≈ 916 eV/cm.

4.3 Energy losses of Muons in Ice

The average energy loss due to Čerenkov radiation of approximately 916 eV/cm, as calculated above, is not the dominant source of energy loss of a muon in the ice. While passing through the detector, muon losses for muon energies $E_\mu \sim 1$ TeV are dominated by four processes. Ionisation, described by the Bethe-Bloch formula, is nearly energy independent at the GeV range and above, and occurs continuously along the trajectory of the muon [31]. Energy losses through bremsstrahlung, pair production of e^+e^- and photo-nuclear interaction, are energy dependent and can

therefore be used for energy reconstructions above the threshold energy, E_{th} (see figure 4.3). In equation 4.12 all energy dependent contributions of the muon losses are expressed in one parameter $b(E_\mu) \approx b \approx 3 \cdot 10^{-4} \text{m}^{-1}$. Whereas ionisation is described by the parameter $a(E_\mu) \approx a \approx 0.2 \text{ GeV m}^{-1}$ [31],

$$-\frac{dE_\mu}{dx} = a + b \cdot E_\mu \quad \text{and} \quad E_{th} = \frac{a}{b}. \quad (4.12)$$

The resulting muon range, R_μ , for muons at energies in the observed energy window, is approximated by equation 4.13 [32], which leads to a muon range of about 1.8 km for a 500 GeV muon.

$$R_\mu \approx \frac{1}{b} \ln \left(\frac{E_\mu}{E_{th}} + 1 \right) \quad (4.13)$$

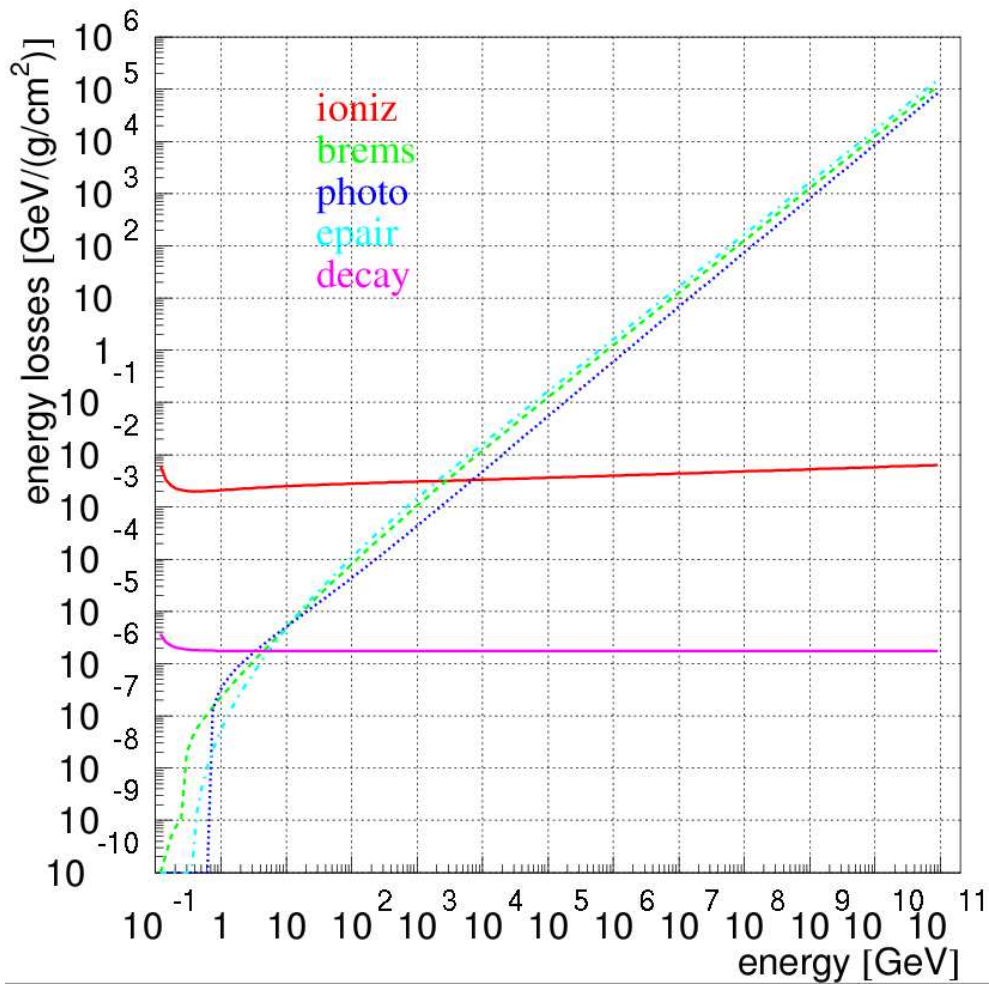


Figure 4.3: Contributions of the different processes leading to muon energy losses in ice as a function of E_μ : decay losses (lower solid line), ionisation (upper solid line), bremsstrahlung (dotted line), photo-nuclear (fine dotted line), and pair production of e^+e^- (dash-dotted line) [33].

Chapter 5

The Combined Detector 2007

AMANDA, the Antarctic Muon And Neutrino Detector Array, is embedded within the much larger detector IceCube. The combined detector array is located deep in the East Antarctic Ice Sheet at the geographical South Pole, close to the Amundsen-Scott station (see figure 5.1). The optical sensors are arranged in a three-dimensional lattice along cables ('strings') and are directed downwards to the center of Earth, thereby minimising atmospheric background from above (see section 5.2).

5.1 From Amanda to IceCube

The first AMANDA strings were deployed during the Austral summer 1993-1994 at depths between 800 m and 1000 m. These strings served as a proof-of-concept for neutrino and muon detection in ice, as the concentration of air bubbles at these depths is too high to reconstruct muon tracks accurately. This detector prototype is called AMANDA-A. At depths lower than 1400 m, the ice is significantly clearer and contains only very few air bubbles. Hence, the scattering length of light increases as well as the absorption length, dominated by insoluble mineral grains. As a consequence of the discovered ice properties, all 19 AMANDA strings (AMANDA-A is not regarded as part of AMANDA) were deployed at depths below 1200 m, in the years 1995 to 2000. String -17 is the only exception, due to deployment problems. The spacing of the in total 677 optical modules (OMs) along the strings ranges from 10 m to 20 m. The strings are ordered within a cylindrical lattice and have horizontal distances to each other, varying from 25 m to 50 m. The total instrumented volume of AMANDA is larger than 10^{-2} km³ [34].

The neutrino observatory IceCube, which is currently under construction, will consist of 4800 digital optical modules (DOMs) installed on 80 strings between 1450 m and 2450 m below the surface [35]. IceCube has with a horizontal spacing of 125 m and vertical spacing of 17 m, a lower density of DOMs but a much larger instrumented volume of 1 km³. IceCube is scheduled to be finished in the Austral summer season 2010-2011. In 2007, 22 strings were operational, embedding AMANDA as a subdetector. The horizontal layout of the combined detector is shown in figure 5.2.

The depth of the different AMANDA strings relative to one IceCube string is shown in figure 5.3.

5.1.1 Optical Modules

The optical modules within both detectors consist of a pressurised glass sphere containing a downwards orientated photo multiplier tube (PMT). The PMTs are in contact with the glass through a transparent silicon gel and have an amplification strength in the order of 10^9 , allowing accurate single photon detections. The glass spheres are transparent for light with wavelengths between 300 nm and 600 nm and have a transmission maximum at 410 nm [34].

AMANDA Optical Module

The PMTs used in AMANDA OMs are 20 cm in diameter. The amplified analogue charge pulse is read out either through optical fibers or twisted coaxial cables. The readout with a twisted pair of cables has a low pulse dispersion, but creates false pulses within the other cables in the bundle, which is called cross talk. The relevant hit information for track reconstructions, such as exact pulse times and initially deployed charges, are extracted at the surface afterwards. Signal run times within the cables have to be considered as a time offset.

IceCube Digital Optical Module

In contrast to the above described AMANDA OMs, the IceCube OMs operate as completely autonomous data acquisition modules by digitising the pulse information within the module (in-ice digitisation). All modules are remotely controlled, independent of each other, and synchronised by a master clock system. Therefore, the digital optical modules (DOMs) timestamp each pulse with the actual ‘in-ice’ time information. The pulse information sent to the surface is not susceptible to cross talk or dispersion like the analogue AMANDA signal. Additionally, the IceCube PMTs have a larger diameter¹ (25 cm) and are therefore more sensitive to Čerenkov light. The actual Čerenkov photons are detected with the PMTs, creating analogue charge signals, which are digitised by a fast Analog-to-Digital converter (FADC) and a set of three advanced transient waveform digitisers (ATWDs). The ATWDs contain three channels with gains of $\frac{1}{4}$, 2 and 16 [34]. The ATWDs sample 128 bins of 3.3 ns width, whereas the FADC samples at a rate of 40 MHz for a time window of 6.4 μ s. This raw IceCube data contains time stamped and digitised waveforms of the measured charge pulses. A DOM that is hit by a Čerenkov photon, sends a signal to the neighbouring DOMs. This enables each DOM individually to check whether the detected hit fullfills the local coincidence (LC) condition, or if it is an

¹Compared to AMANDA, this gain in sensitivity is outweighed by the loss in sensitivity due to the wider spacing of the IceCube DOMs. Overall, E_{th} is higher for IceCube than for AMANDA, which makes AMANDA more sensitive for low energy detection

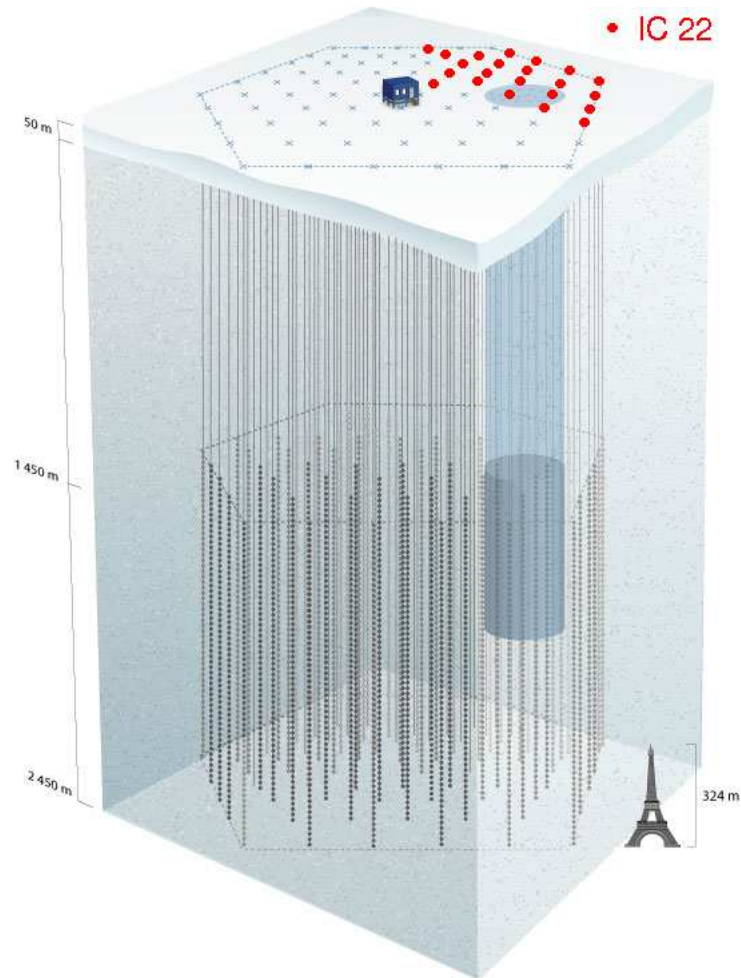


Figure 5.1: *Three dimensional overview of the future IceCube 2010 detector. The red circles indicate the position of the in 2007 active 22 strings. AMANDA is shaded dark [22].*

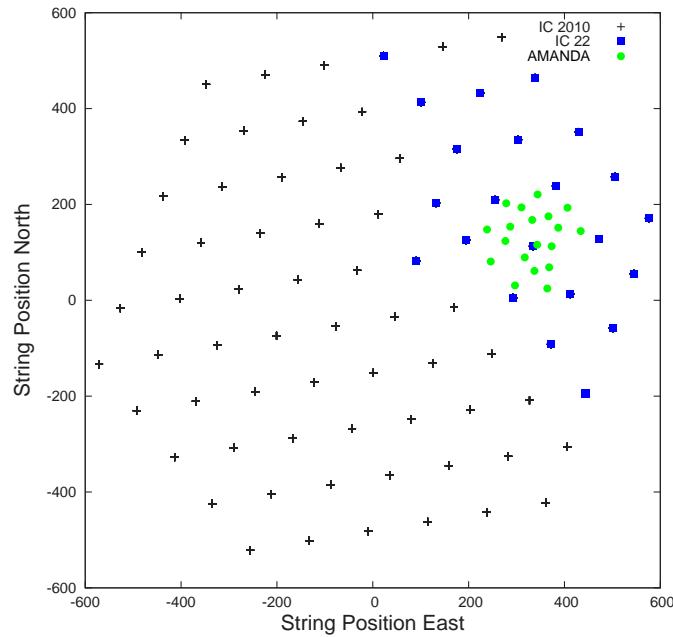


Figure 5.2: *Horizontal layout of the string positions for the combined detector. The 2007 combined detector consists of IC 22 (blue squares) and AMANDA (green circles). The crosses indicate the planned future IceCube strings.*

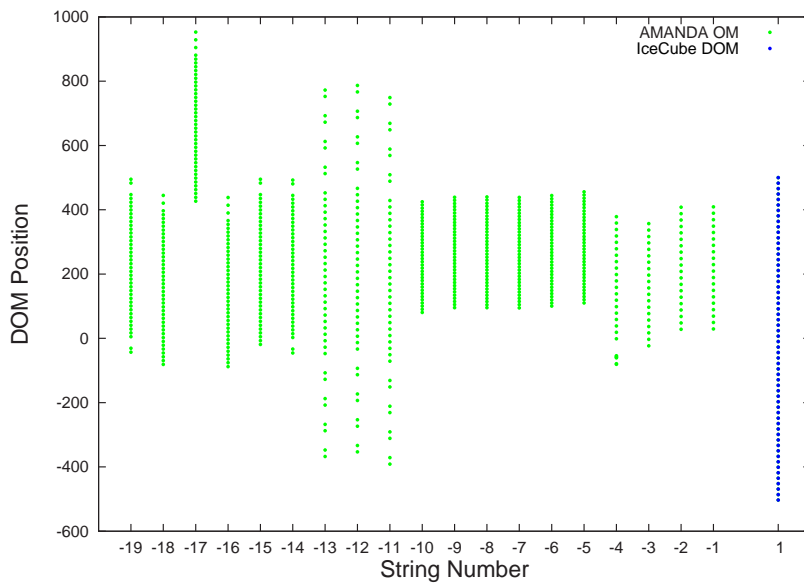


Figure 5.3: *The green strings, labeled by convention from -19 to -1 , represent the AMANDA detector. They are displayed in comparison to one representative IceCube string (blue), as these are all deployed at the same depth and have uniform spacing of DOMs. The zero point marks the origin on the z -axis in the detector coordinate system at an absolute depth of 1730 m from the surface.*

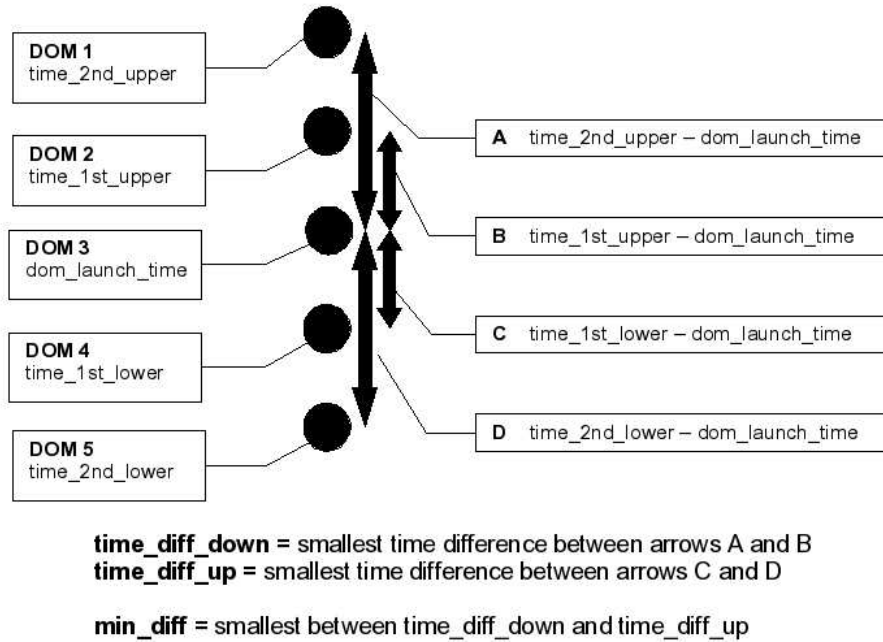


Figure 5.4: Description of the LC span 2 setting for IceCube. DOM 3 is the initially responding DOM. Within two neighbouring DOMs (in this example DOMs 1, 2, 4, 5) another hit has to be detected within a time window, t_{LC} . t_{LC} is set to 1000 ns. If LC is not fulfilled, the hit is regarded as an isolated hit. Figure taken from [36]

isolated hit. LC, with a setting of LC span 2, is explained in detail in figure 5.4. For the generally used LC span 2 setting, it is required that there is an additional DOM hit within two neighbouring DOMs to the initially responding DOM in a maximum time frame defined by a time t_{LC} .

5.1.2 Data Acquisition

The difference in the raw readout signals between both detector arrays (digital vs. analogue) demands separate data acquisition systems (DAQs). Additionally, the IceCube-DAQ and the TWR-DAQ (transient waveform decoder), which is the AMANDA DAQ, have unique, detector specific trigger systems. Events fulfilling trigger conditions are later unified into one single event by the joint event builder (JEB).

TWR-DAQ

Signals which are sent to the surface by the 677 AMANDA OMs, are digitised in the digital multiplicity adder discriminator (DMADD). The DMADD forms a signal of

2.5 μs length if the analogue OM signal passes a configurable pulse discriminator. All generated signals are added together and are tested against three primary trigger conditions. Events with more than 18 hits fulfill the high multiplicity channel, *M18*, and are directly accepted by the TWR-DAQ. The second primary trigger, the *string trigger*, tests the number of hit OMs on one string, *X*, out of all adjacent OMs, *Y*, on a single string. Events actuating the *string trigger* with settings of (6/9) for strings -1 to -4 and (7/11) for strings -5 to -19 are also forthwith accepted. Events passing the low multiplicity pre-trigger, *M13*, are further tested by an additional trigger algorithm. Firstly, this algorithm checks for a minimum of 20 fragments, *F20*, in the signal. Fragments are individual peaks in the recorded pulses, which indicate that at least one module has detected more than one photon separated in time. *F20* events are accepted as well as events passing the second algorithm, the *volume trigger*, which works in a similar way to the IceCube LC condition that cannot be applied initially to the analogue AMANDA signal. If four pairs of hits within spheres of maximum radius 60 m are found, the event is accepted. The TWR-DAQ samples the pulses at a rate of 100 MHz.

IceCube-DAQ

The IceCube trigger system is only software based, since the DOM signals are already digitised. All DOM hits, as described in section 5.1.1, are sent to digital string processors (DSPs). The DSPs report all hits to a central trigger processor. If there is a minimum of 8 hit DOMs within 5 μs , that fulfill the LC condition, IceCube is triggered. This basic multiplicity trigger, called simple majority trigger (*SMT8*), was the only active trigger in 2007. Other software triggers, like a string trigger similar to the AMANDA *string trigger*, are planned and tested, but had not been implemented in 2007.

Joint Event Builder (JEB)

Events that have been triggered individually by the two DAQ systems are merged by the JEB into one frame. In the combined detector 2007, consisting of 22 IceCube strings and 19 AMANDA strings, the TWR-DAQ is set to trigger a forced readout of the IceCube-DAQ. This provides the opportunity to compare the detected low energy events in AMANDA with background detected in IceCube. It also enhances the possibility of a high quality reconstruction, because a recorded event might not have been bright enough to trigger IceCube individually, but can still be detected by several IceCube modules. Forcing a read-out of AMANDA by the IceCube-DAQ is technically not feasible, due to the lack of event buffering in the TWR-DAQ system [37]. The JEB unifies events triggered by the TWR-DAQ and the IceCube-DAQ, if they happen close in time. The created unified event has a time window of ± 8000 ns. The major difficulty, arising out of the detector integration, is to definitely determine whether both events correspond to the same event, or if they are two independent events, happening coincidentally in time.

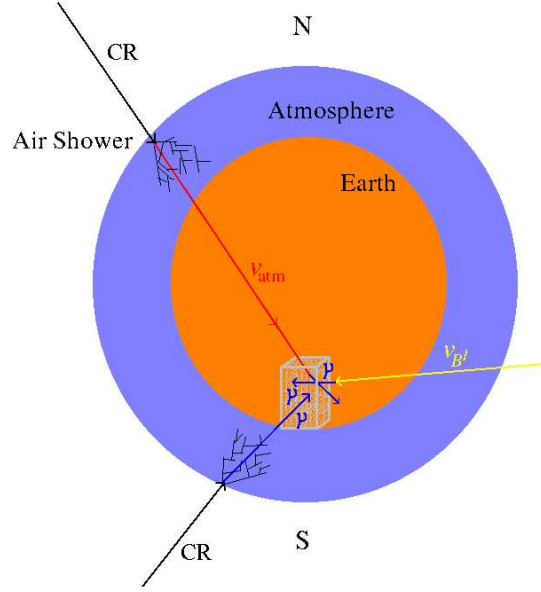


Figure 5.5: *Signal and background muon sources in the combined detector. Atmospheric muons, μ_{atm} , and neutrinos, ν_{atm} , are created in air showers in the Earth's atmosphere by CR interactions with molecules. μ_{atm} can only come from above the detector, due to the limited muon range in medium. Muons created nearby the detector in CC reactions from ν_{atm} have no angular limitation. A signal source for neutrinos is illustrated by a LKP neutrino, $\nu_{B^{(1)}}$, which can only come in an angular range of $\Theta < 23^\circ$ above and below the horizon at the South Pole.*

5.2 Background

The experimental background in the combined detector is dominated by atmospheric muon events, μ_{atm} , from above the South Pole. Although μ_{atm} are triggered roughly 100000 times more often than atmospheric neutrinos, ν_{atm} , their angular distribution makes rejection very efficient. ν_{atm} can travel through Earth unhindered and are therefore indistinguishable from signal events. This scenario is illustrated in figure 5.5 with a LKP neutrino as a possible signal source.

5.2.1 Atmospheric Muons

Cosmic Rays (CRs), consisting of protons, p , alpha particles, He^{2+} , and electrons, e^- , produce highly energetic, ultra relativistic muons in reactions with molecules in the Earth's atmosphere. Muons, created in the resulting air showers, can penetrate the East Antarctic Ice Sheet up to several kilometres deep. The average trigger rate of around 600 Hz for the combined detector is entirely dominated by μ_{atm} . The μ_{atm} energy spectrum follows, in first order, the initial power law spectrum of CRs, which is proportional to $E^{-2.7}$ [38]. μ_{atm} are constrained to a zenith angle range of $0^\circ < \Theta < 90^\circ$. Thus, μ_{atm} show up as strictly downgoing events and can be efficiently rejected by directional cut selections (see also chapter 7).

5.2.2 Atmospheric Neutrinos

CR interactions in the atmosphere also create high energy neutrinos, ν_{atm} . ν_{atm} are produced in decays of secondary air shower particles like μ^\pm , π^\pm , K and other mesons. In the GeV-range, their energy spectrum follows the CR powerlaw spectrum, proportional to $E^{-2.7}$. At energies above 1 TeV, the interaction length of the secondary particles becomes shorter than the decay length, resulting in a steepening of the spectrum ($\propto E^{-3.7}$) [39]. The angular distribution is not perfectly isotropic as the initial CR spectrum might indicate. The horizontal component is slightly enhanced compared to the vertical component. This anisotropy is caused by the non-uniform atmospheric density profile. Particle path lengths in less dense upper layers are increased for horizontally moving particles, whereas for vertical particles, path lengths are decreased. ν_{atm} are the dominant background at higher filter levels (see chapter 7).

5.2.3 Solar Neutrinos

Solar neutrinos², ν_\odot , in this study refer to the neutrinos created in CR showers in the Sun's atmosphere. At targeted energies in the GeV-range, the expected flux is minor compared to the ν_{atm} flux and can therefore be neglected. At energies above the targeted range (10 TeV), the ν_\odot flux is calculated to exceed the ν_{atm} flux [40].

5.2.4 Galactic Neutrinos

Galactic neutrinos are a result of CR interactions with interstellar gas in the galactic disk. The created neutrino flux contributes significantly at very high energies above 100 TeV to the total neutrino background. At lower energies, the contribution is diminutive. Generally, neutrino detectors in the Southern Hemisphere are not ideally positioned for neutrino sources situated in the Southern celestial Hemisphere.

5.2.5 Cosmological Neutrinos, GZK Effect

CRs with energies above $6 \cdot 10^{19}$ eV are energetic enough to produce a delta resonance in the reaction with a photon from the CMB [41]. Equations 5.1 and 5.2 describe the ultra high energy neutrino production resulting out of this resonance.

$$p \cdot \gamma \rightarrow \begin{cases} (1/3)\Delta^+ \rightarrow n\pi^+ \\ (2/3)\Delta^+ \rightarrow p\pi^0 \end{cases} \quad (5.1)$$

$$\pi^+ \rightarrow \nu_\mu + \mu^+ \rightarrow e^+ + \nu_e + \bar{\nu}_\mu \quad (5.2)$$

The created diffuse ultra high energy neutrino flux is modelled to be very low and is also afflicted with a high degree of uncertainty, due to little knowledge about the origins of ultra high energy cosmic rays, and is consequently not considered.

²Here, ν_\odot does not refer to the low energetic solar neutrinos, which are produced in the Sun's fusion processes.

5.2.6 Point Source Neutrinos

Point sources other than the Sun are possible sources of background neutrinos. Theoretical models describing gamma ray bursts (GRBs) and active galactic nuclei (AGN) predict the production of neutrinos by processes accompanying these phenomena. Nevertheless, the estimated diffuse neutrino fluxes are too low to play an important role in the composition of the total neutrino background. However, the large flux of low energetic Supernova neutrinos could possibly be detected in neutrino telescopes by an excessive rise of the background noise. A summary of all discussed sources of neutrino fluxes contributing to the total expected background is shown in figure 5.6.

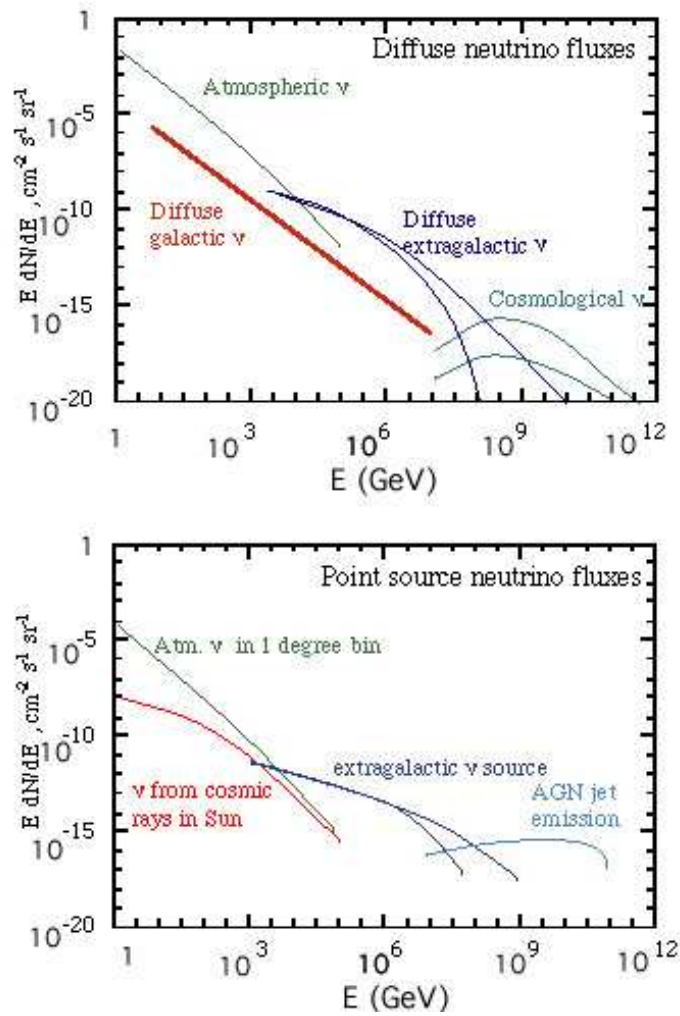


Figure 5.6: Neutrino fluxes from different sources. The upper diagram shows the individual contributions towards the total expected neutrino background from the discussed diffuse sources. The lower diagram illustrates the expected neutrino background fluxes arising from point sources [42].

Chapter 6

Simulation and Reconstruction Methods

This chapter introduces the individual simulation (6.1) and reconstruction steps (6.2) for the different simulated data sets of background sources and signals. Background simulations of physics events are crucial for the detailed understanding of the detector. A certain source of background, e.g., atmospheric muons, is generated and the detector response simulated, in order to compare the simulated background with the experimentally observed, ‘real’ background. This is a viable method of learning about the detector and its physical and technical properties. Expected signal fluxes from selected sources are generally very low, and hence strongly hidden in the background of the experimental data. Only if the experimental detector response is precisely reflected by the simulation, an accurate signal simulation is possible and therefore discoveries of signal events within the experimental data can be made.

The IceCube software framework utilised for this study, is called IceTray [43] and contains all module based simulation, reconstruction, and analysis applications. All applications work as independent code units that can be individually improved, changed or developed.

6.1 Monte Carlo Simulation

The simulation¹ chain for the combined detector (2007) simulation is divided into four major parts:

1. particle generation
2. particle propagation
3. separate simulation of the detector response of IceCube and TWR²
4. combining detector responses in a global trigger

¹Simulation version IceSimV02-00-14 was used in this thesis for all simulations

²The term TWR, describing the waveform digitiser of AMANDA, is used further as a descriptive abbreviation for the AMANDA detector.

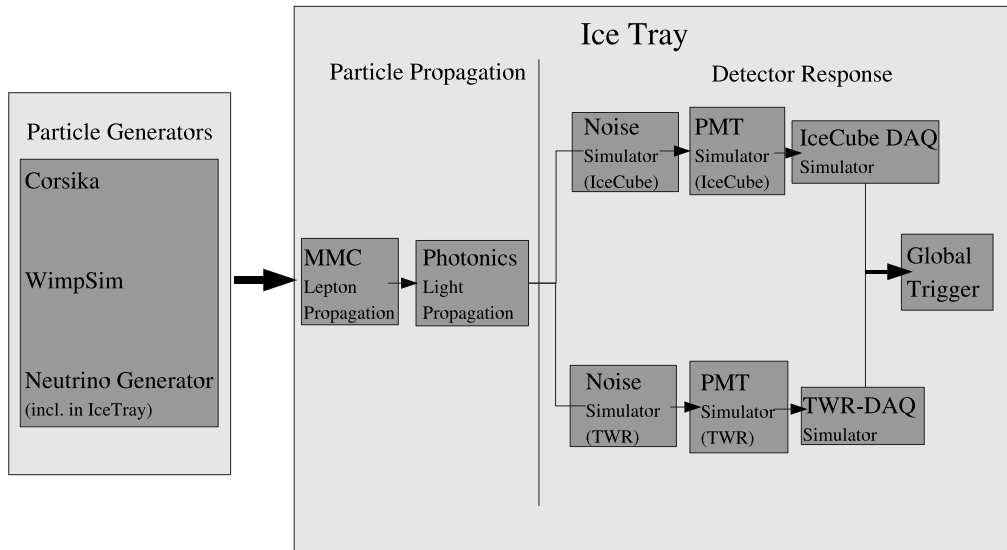


Figure 6.1: *Flow chart of simulation chain. Particles are generated in various particle generators before they are translated to the IceTray framework. Within IceTray, lepton and photon propagation is simulated. The detector response simulation is separated into two streams, IceCube-DAQ and TWR-DAQ, before they are recombined in the global trigger.*

The interconnection of these four parts is illustrated by the flow chart in figure 6.1. Firstly, particles are generated in specific particle generators, which propagate the created neutrinos to the detector location and create primary leptons in the proximity of the detector through interactions described in detail in chapter 4. The second simulation step is the propagation of the created primary and secondary charged particles and resulting photons to the detector modules. The third step, the simulation of the detector response, is divided into two separate streams, according to the different signal processing methods of the AMANDA and IceCube OMs, explained in chapter 5.1.2. Both streams are reunited in the final simulation step by the global trigger, which combines physical events from both detectors into one frame.

The second part of the simulation chain, the propagation of the secondary particles (see figure 6.1), which is embedded in IceTray, is independent of the selected type of particle generator, and therefore the same for all simulated datasets. Thus, the simulated datasets, divided into the different particle generators, are introduced after the uniform simulation steps are outlined.

MMC

MMC, the Muon Monte Carlo propagation program [33], which has been implemented into the IceTray framework, propagates the produced leptons through the sensitive area of the detector. It distinguishes between several different media, like air, shallow ice, deep ice and the bedrock. Primary charged particles lose energy along their tracks through ionisation, bremsstrahlung, pair production of e^+e^- , and photo-nuclear interactions (as detailed in 4.3). Within the sensitive area of the detector, secondary particles of energies higher than 0.5 GeV, created in the above listed processes, are treated as individual particles.

Photonics

Photonics is a photon tracking Monte Carlo package, which calculates photon fluxes and resulting time distributions in a medium surrounding a light source. The light emitted by charged primary and secondary particles is affected by scattering and absorption in ice. In shallower ice layers, above 1300 m, scattering of photons is predominantly caused by air bubbles. At actual detector depths, the pressure in the ice is extremely high. Therefore, air bubbles are rare and have little influence on the scattering length. Generally, the Antarctic ice does not have a smooth distribution of scattering and absorption centres, like insoluble particles and crystals. The so called dust layers reflect the atmospheric compositions several 100,000 years ago. Figure 6.2 shows the scattering profile as a function of depth, derived from an age vs. depth comparison interpolated from the Vostok ice core data. The different layers were further confirmed by a dust logging device that was used during the deployment of the IceCube strings [34].

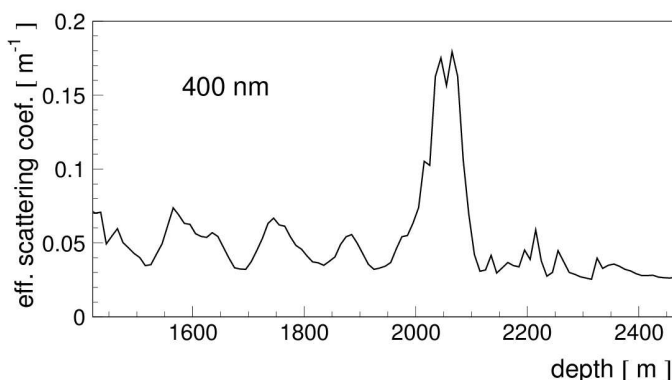


Figure 6.2: *The effective scattering coefficient distribution varying with detector depths shown for 400 nm [34].*

The Photonics package is used to produce tables of light fluxes for a range of some depth and initial particle direction. Photons emitted along the tracks of ultra relativistic muons are generated by integrating over a large number of point emitters.

The implementation of the heterogeneous ice properties into the simulation chain is achieved through accessing these Photonics³ tables [44, 45].

Detector Response

The simulation of the detector response calculates the number of expected photo electrons in the PMTs from the number of arriving Čerenkov photons. The number of photo electrons depends on the DOM sensitivity and the effective DOM Area (track angle). Additional noise hits are added as a baseline to the signal. In a final step, the triggers are simulated and the simulated, triggered physics events are combined into one frame by a global trigger simulation.

6.1.1 LKP Signal

The LKP signal is generated with the software package WimpSim. WimpSim simulates the LKP annihilations in the center of the sun and propagates the produced signal neutrinos to the detector, where they are forced to interact with nuclei in the ice [46]. The IceTray based module, WimpSim Reader [47], translates the generated WimpSim events into the IceTray format and distributes them in a custom chosen generation volume⁴. The centre of the selected volume overlaps with the origin of the combined detector coordinate system (2007 configuration). WimpSim consists of two parts, WimpAnn and WimpEvent⁵. WimpAnn generates neutrinos from a selected number of annihilations, N_{ann} , in the Sun in a certain annihilation channel, and propagates them out of the sun, through space to a distance of 1 AU . For the neutrino simulations the programs DarkSUSY [48] and PYTHIA [49] are used by WimpAnn, whereas the neutrino-hadron interactions on the way out of the Sun are simulated with nusigma⁶ [50]. WimpEvent also uses nusigma to simulate the neutrino-hadron interactions in the ice on their path to the detector location on Earth. Despite the fact that ultimately only muon neutrinos are considered in this analysis, WimpSim propagates all three flavours of neutrinos created in the annihilation processes and handles also full three flavour neutrino oscillations (matter and vacuum) during the propagation of the created neutrinos to the detector. nusigma uses the CTEQ6-DIS parton distributions for the CC and NC interactions for neutrinos and antineutrinos. Throughout one year, the zenith direction to the Sun at the South Pole is limited within $\pm 23^\circ$ around the horizon. In this analysis, only the time of the year when the sun is strictly below the horizon (dark year) is used, in order to increase the atmospheric muon background rejection probability. The signals used are defined by N_{ann} , the annihilation channel, ch , the LKP mass, $m_{B(\chi)}$, and the specified time interval, t . To cover the full allowed mass range for LKPs,

³For all simulations, AHA07vlice (IC22) and AHA07v1ama (TWR) Photonics tables are used.

⁴The chosen volume is defined by $[-100.0 < x < 800.0, -300.0 < y < 600.0, -600.0 < z < 600.0]$.

⁵In this analysis, versions WimpAnn-2.07 and WimpEvent-2.07 were used.

⁶Versions DarkSUSY-4.1.6-lite, PYTHIA-6.400 and nusigma-1.14-pyr were used.

derived in section 2.3.2, three sets of signals for the masses,

$$m_{B^{(1)}} = 500, 750, 1000 \text{ GeV}/c^2 ,$$

are simulated. As explained in chapter 2.3.2, the strength with which LKPs couple with ordinary matter, is only proportional to the SM particles' hypercharge, which is well known. Consequently, the branching ratio of each annihilation channel can be well approximated (see table 3.1). Several channels result in a significant number of generated neutrinos. Some channels with high branching ratios, like the $u\bar{u}$ channel, are not feasible because of their long lifetime (explained in detail in section 3.2). All channels and parameters chosen are listed in table 6.1. The neutrino oscillation parameters without CP violation and standard mass hierarchy are taken from [51].

Simulation Parameter	Parameter Value
$m_{B^{(1)}}$ in $[GeV/c^2]$	500, 750, 1000
channel ch	$1(c\bar{c}), 2(b\bar{b}), 3(t\bar{t}), 4(\tau^+\tau^-),$ $16(\nu_e\bar{\nu}_e), 17(\nu_\mu\bar{\nu}_\mu), 18(\nu_\tau\bar{\nu}_\tau)$
N_{ann}	$2 \cdot 10^6$
ν -mixing angle θ_{12} in $[\circ]$	33.2
ν -mixing angle θ_{13} in $[\circ]$	0.0
ν -mixing angle θ_{23} in $[\circ]$	45.0
CP-breaking phase δ for ν -oscillations	0
mass difference Δm_{21}^2 in $[eV^2]$	$8.1 \cdot 10^{-5}$
mass difference Δm_{31}^2 in $[eV^2]$	$2.2 \cdot 10^{-3}$
t time interval in fraction of one year	[0.25, 0.75]

Table 6.1: *Input parameters for the WimpSim signal simulations, with the annihilation channel, ch , the number of annihilation, N_{ann} , and the LKP mass $m_{B^{(1)}}$.*

The WimpSim output is a physical event corresponding to one annihilation process, which results in a neutrino. This event contains directional and energy information for the incoming neutrino, the created lepton and the resulting hadronic shower. The scattering angle, ψ , between incoming ν and created μ decreases with increasing ν energy. Figure 6.3 shows the zenith angle distribution for the simulated time span, t , for initial neutrinos and created muons. The angular spectrum for the created muons broadens slightly, but still contains good directional information about the initial ν .

Figure 3.2 shows the true ν_μ spectrum from all annihilation channels for $m_{B^{(1)}} = 1000 \text{ GeV}/c^2$ at the detector for the parameters specific to this analysis. One can clearly see the distinct sharp delta peak in the three direct neutrino channel spectra (16, 17, 18), as well the softer spectra of all other channels (1, 2, 3, 4). In comparison, figure 6.4 shows the same signals as figure 3.2 for the corresponding simulated muon spectra. All muon spectra are softer than their initial neutrino spectra and distinct features in the ν_μ spectra are smeared out, e.g., the dominant delta peaks. The muon

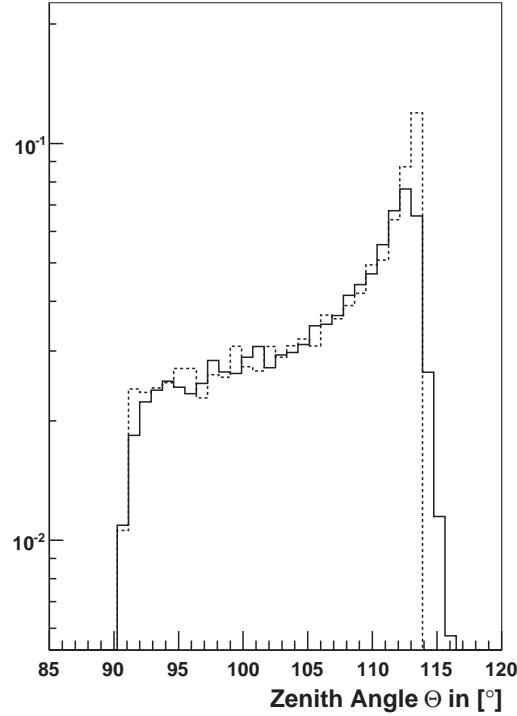


Figure 6.3: Zenith angle distribution for initial LKP ν (dashed) and created μ (solid). The displayed zenith angle range is limited to angles when the Sun is below the horizon.

spectra are rescaled to a total value of one, in order to allow better comparison of the pronounced spectral features.

Weighting of the LKP Signal

Within the simulation chain, specific multiplicative weights are calculated for each interaction that a generated neutrino undergoes. This is necessary, because interaction probabilities and oscillations depend on neutrino energy and flavour. WimpSim constructs the output weights, w_i , for the created lepton tracks as a volumetric flux, ϕ_{Vol} , per annihilation in the Sun and per unit volume. This is given by:

$$\phi_{Vol} = \frac{1}{N_{ann}} \sum_i^{N_{ann}} w_i \quad (6.1)$$

The number of corresponding physical events, N_{Phys} , from a spectra, defined by w_i , in a volume V is calculated to,

$$N_{Phys} = V \cdot \sum_i^{N_{ann}} w_i, \quad (6.2)$$

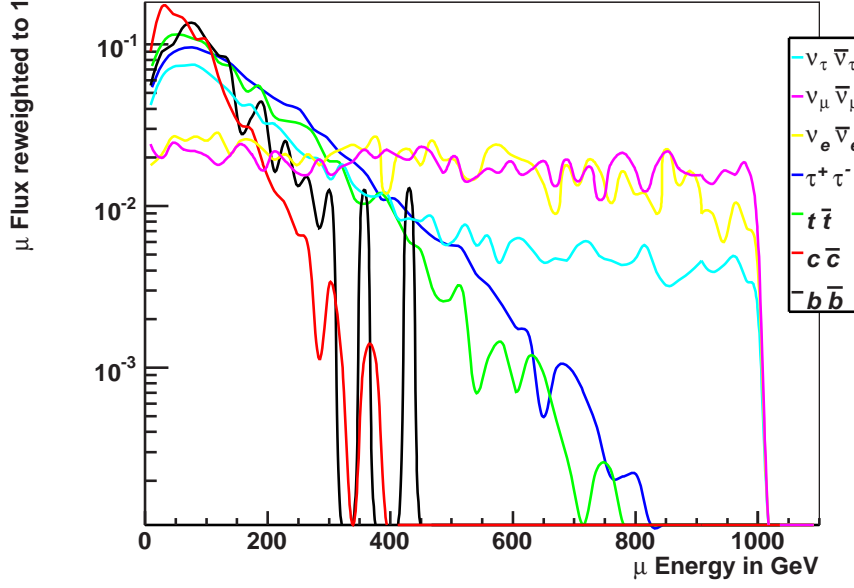


Figure 6.4: Muon energies spectra of WIMP signals for all chosen annihilation channels with a LKP mass of $1000 \text{ GeV}/c^2$. The displayed muon spectra are reweighted and normalised to 1. Therefore the displayed spectra do not reflect the true frequency of occurrence.

whereas a subset of observed physical events, N_{Obs} , e.g., events surviving certain cut criteria is given by,

$$N_{Obs} = \sum_i^{N_{ann}} w_i \delta_i V_{gen,i} , \text{ where } \delta_i = \begin{cases} 0 & \text{event not observed} \\ 1 & \text{event observed} \end{cases} \quad (6.3)$$

The interaction vertices of all N_{Phys} events from a specific WimpSim spectrum are randomly placed by the WimpSim Reader inside a generated volume, V_{gen} , around the sensitive detection volume of the detector⁷. The size of the generated volume for each muon is energy dependent. Higher energetic muons can travel longer distances and therefore have a higher observation probability by the detector. In order to make qualitative assumptions about detection efficiencies of the combined detector, the principle of an effective volume, V_{eff} , of the detector is introduced. An ideal detector setup is able to detect, reconstruct and select in the final filter stage (see chapter 7) every muon that was initially placed in a fixed volume around the detector. Due to the many imperfections in detector components (trigger, reconstruction and cut selection), the detector sensitivity to the LKP induced neutrino flux is degraded. The effective volume for the real situation, where only a fraction, N_{obs} , of the initial neutrinos, N_{gen} , is observed, is given in equation 6.4 for a constant

⁷This volume is defined by the cylinder containing the combined detector

generation volume, V_{gen} .

$$V_{eff} = \frac{N_{obs}}{N_{gen}} V_{gen} \quad (6.4)$$

As described above, the generated volume is energy and event dependent and hence different for each N_{gen} . In this case, V_{eff} is calculated as

$$V_{eff} = \frac{\sum_i^{N_{gen}} w_i \delta_i V_{gen,i}}{\sum_i^{N_{gen}} w_i} . \quad (6.5)$$

6.1.2 Muon Background

The atmospheric muon background is generated with dCORSIKA, which is a specialised version of the air shower generation code CORSIKA [52]. The main adaptation for neutrino telescopes is a three dimensional detector instead of a surface detector. The initial isotropic cosmic ray spectrum is injected into the atmosphere with an energy spectrum proportional to $E^{-2.7}$ in a zenith angle range from 0° to 90° . dCORSIKA simulates hadronic interactions in the Earth's atmosphere, decays of unstable particles and secondary processes, like ionisation and scattering losses. Of all simulated muons, only muons that enter the sensitive cylindrical volume of the combined detector are selected. The zenith angle distribution of a triggered μ_{atm} subsample, corresponding to 131 seconds of detector live time, is shown in figure 6.5.

Weighting of Muon Background

Atmospheric muon events do not require reweighting, because they are generated as a true spectrum in units of $N_{\mu_{atm}}/s$ per unit volume.

6.1.3 Neutrino Background

The atmospheric neutrino background that is produced in cosmic air shower reactions in the atmosphere, is generated with the IceTray implemented Neutrino-Generator, based on the program ANIS [53]. Neutrino-Generator simulates all neutrino flavours with a selected energy spectrum proportional to $E^{-\alpha}$ and propagates them through Earth to the detector location. The spectral index α can be chosen in order to favour the simulation of high energy events that are strongly suppressed within the true atmospheric spectrum ($E_\nu^{-3.7}$). This ensures higher statistics at all energy levels. The simulated neutrinos are forced into hadronic interactions within a defined cylindrical generation volume, where the z -axis is set to be collinear with the incoming ν track.

Weighting of Neutrino Background

ν_{atm} events have to be reweighted to the correct spectrum and expected number of events per time. Neutrino-Generator places a weight into the frame, combining

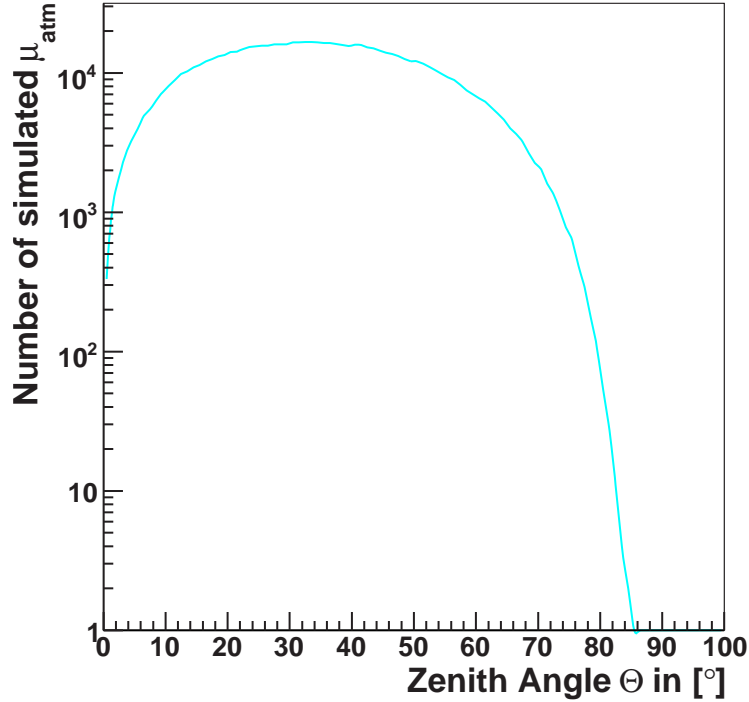


Figure 6.5: Simulated μ_{atm} zenith distribution, triggering the combined detector 2007. The displayed data sample corresponds to a detector livetime, t_{live} , of 131 seconds.

effects like spectral indices, generation volume and interaction probabilities. The so called *OneWeight* is further reweighted in the reconstruction process to match an atmospheric spectrum in the Bartol model with $E_\nu^{-3.7}$ [54]. The number of simulated ν_{atm} events in the time interval, t , is then derived by a simple multiplication with t in the order of seconds. Figure 6.6 is the triggered simulated ν_{atm} flux of the ν_{atm} dataset (see section 6.3). It reflects the theoretically expected ν_{atm} flux and is used to check the validity of the reweighting process.

6.2 Reconstruction Methods

Every detector experiment ultimately hunts for fully contained events, which are events of the highest quality, regarding the predictability of the underlying physics. Contained events deposit all their energy within the detector. Ultra high energy (UHE) muons travel large distances in ice, which makes it very difficult, or even impossible, to detect fully contained muon events in neutrino telescopes. Hence, event information in the combined detector is obtained from accurate track reconstructions that contain detailed directional information about the initial neutrino, as energy reconstructions are very difficult. The triggered signal is dominated by downgoing atmospheric muon background events. A fast first guess algorithm reconstructs a probable muon track candidate to distinguish between up and down going

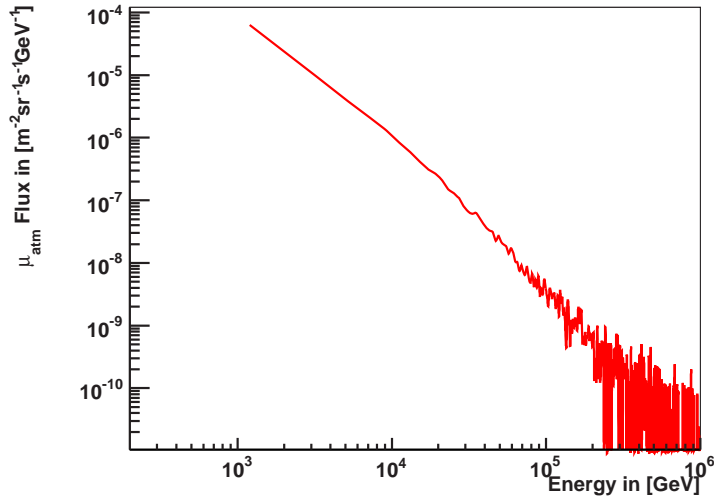


Figure 6.6: Simulated ν_{atm} spectrum (ν_{atm} dataset) triggering the detector, used as a sanity check for a correct reweighting procedure.

muon tracks, in order to minimise the data volume for the interminable likelihood reconstruction algorithms. First guess tracks also conduce to the likelihood reconstruction algorithms as an initial track hypothesis. For the following derivations, the definitions of track variables are given in the left diagram of figure 6.7.

6.2.1 First Guess

In this thesis two first guess methods are used within the first reconstruction⁸ step. The IceJAMS method [55] is a more sophisticated first guess algorithm than line-fit, but was found to be less accurate overall for the combined detector reconstruction. Nevertheless, it was used as a decision in the level 1, $L1$, filtering (explained in detail in section 7.2.1), in order to not fully rely on one single algorithm in the first filter level. IceJAMS collects the hit information of each event (t_i, r_i) and divides the unit sphere uniformly into N possible initial track directions. The basic idea of IceJAMS is that along a possible track r , all hits cluster in a Gaussian distribution in a plane perpendicular to r . For unlikely directions, the Gaussian distribution is shifted off the center. Further, IceJAMS searches for the best fit of all possible tracks N , by training and testing an artificial Neuronal Network (NN). The final output of IceJAMS is one track, corresponding to the best fit of the NN.

The line-fit [56] first guess method is used as a directional decision in $L1$ filtering. In addition, it is used as a seed for the likelihood based reconstruction methods. line-fit estimates an initial track on the basis of hit times, t_i . It ignores specific optical properties of the medium, as well as the geometry of the Čerenkov cone, and assumes light traveling along a 1-dimensional track path with constant speed v [57]. A χ^2

⁸IceRecV01-06-02 was used for all reconstructions.

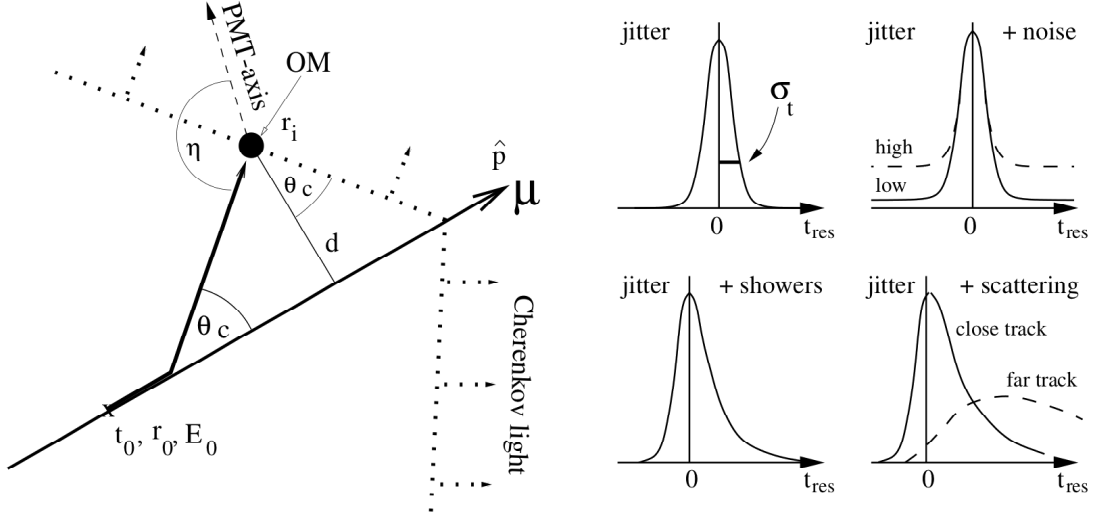


Figure 6.7: The left diagram defines all relevant track variables and coordinates for the reconstruction process ($r_0, r_i, t_0, E_0, \hat{p}, d$). The four diagrams on the right side, demonstrate the impact of different effects, like noise (top-right), hadronic showers (bottom-left) and scattering (bottom-right), and the PMT jitter distribution, defined as a Gaussian with the jitter time σ_t (top-left) on the residual time t_{res} distribution of a hit. [57]

variable can be defined by summing over all observed hits, N_{hit} ,

$$\chi^2 = \sum_{i=1}^{N_{hit}} (r_i - r - v \cdot t_i)^2 . \quad (6.6)$$

By minimising χ^2 the fit parameters v and r are obtained.

6.2.2 Likelihood Reconstruction

Likelihood reconstruction algorithms determine a set of unknown track parameters, \mathbf{a} , from a set of observed experimental values, \mathbf{x} , by minimising the negative log-likelihood, $-\log(\mathcal{L}(\mathbf{x}|\mathbf{a}))$, where

$$\mathcal{L}(\mathbf{x}|\mathbf{a}) = \prod_i p(x_i|\mathbf{a}) , \quad (6.7)$$

is the probability density function (p.d.f.) of the independently measured components, x_i , and is defined by $p(x_i|\mathbf{a})$ [57]. The track parameters \mathbf{a} are described by

$$\mathbf{a} = (r_0, t_0, E_0, \hat{p}) \text{ with } r_0 = (x_0, y_0, z_0, \theta, \vartheta). \quad (6.8)$$

For this analysis the patched Pandel p.d.f. is used, which gives the probability of observing an event within a residual time, $t_{res} = t_{hit} - t_{geo}$, at a closest distance, d_i , between track and hit OM. t_{geo} is the expected arrival time of a photon, calculated

along the geometrical path without scattering. The patched Pandel is based on the Pandel p.d.f. that takes into account scattering and absorption of photons in ice, and is parametrised as

$$p(t_{res,i}|d_i) = \frac{\tau^{-d_i/\lambda_s} \cdot t_{res,i}^{d_i/\lambda_s-1}}{\Gamma(d_i/\lambda_s)} \cdot e^{-(t_{res,i}/\tau + ct_{res,i}/n\lambda_a + d_i/\lambda_a)}, \quad (6.9)$$

with the scattering time, $\tau = 557$ ns, the absorption length, $\lambda_a = 98$ m, and the scattering length, $\lambda_s = 33.3$ m [58]. In order to get the patched Pandel p.d.f. relevant for this analysis, $p(t_{res,i}|d_i)$ is convoluted with a Gaussian function at time t_0 , where the width of the Gaussian is set to match the jitter time, σ_t , of the PMTs. The influence of the PMT jitter for different observed photon arrival times is illustrated in the four diagrams on the right in figure 6.7. PMT noise is added as a constant to the patched Pandel function. To further improve the accuracy of the reconstructed track, the iterative fit reconstruction is used. The iterative fit performs the described minimisation for N first guess tracks, distributed in a cone around the initial line-fit track. Furthermore, the smallest value for $-\log(\mathcal{L}(\mathbf{x}|\mathbf{a}))$ is determined, which corresponds to the best likelihood fit.

The paraboloid reconstruction method [59] is additionally performed, to estimate the angular uncertainty of each event. paraboloid evaluates the likelihood function in the neighbourhood of the best fit with Gaussian functions. Consequently the angular uncertainty is determined by the quality of the agreement between real likelihood function and Gaussian function. The angular agreement value, σ_{para} , is used as an important cut value in the filtering process, see section 7.2.2.

6.3 Data Sets

For a point source analysis with a strongly hidden signal, like the LKP signal from the Sun, a key issue is to understand the detector response and the background in detail. The simulated background in this analysis consists of atmospheric muons and atmospheric neutrinos. The datasets, generated by the IceCube simulation production (simprod), are listed in table 6.2, including all detailed settings. Simulated background datasets, together with the simulated signals, are used to design cuts because their different dependencies on certain observables or parameters can be clearly identified. Additionally, they are used to explain expected remaining background events before the final cut level. The simulated background has to match the actual experiment as exactly as possible at all levels of filtering. This comparison is shown in detail in section 7.1. In the 2007 combined detector, a second source of atmospheric muon background has to be considered. The instrumented detector volume is so large that two muon tracks can pass the detector coincidentally at two different positions. These so called coincident muon events can be misreconstructed as an upgoing neutrino event. Therefore, an additional dataset containing simulated coincident muon events is considered in order to match the experiment. At

the time of the design of the cuts for this analysis, no combined detector coincident muon sample was available. Consequently, this source of background is not perfectly reflected by the simulated coincident dataset, which is only triggering IceCube. Nevertheless, the MC background comparison with the experiment (see 7.1) is very accurate. This can be explained by the fact that coincident muon events are triggering the detector as very high energetic (bright) events, with many hit DOMs. Additionally, such events are spread out over a large fraction of the detector instrumented volume. Consequently, the probability to hit an IceCube DOM is much higher than for an AMANDA OM. Hence, coincident muons predominantly trigger IceCube.

Simprod dataset	Generator	Parameters $E_{CR,\nu}$ in GeV	N_{files}	$\langle N_{gen} \rangle$ per file	$\langle N_{trig} \rangle$ per file	t_{live} in days
963 IC22+TWR	corsika	μ with $E^{-2.7}$ $600 < E_{CR} < 10^{11}$ $0^\circ < \theta < 90^\circ$	9996	$85.37 \cdot 10^3$	$1.506 \cdot 10^3$	0.303
964 IC22+TWR	corsika	μ with $E^{-2.7}$ $600 < E_{CR} < 10^{11}$ $0^\circ < \theta < 90^\circ$	10000	$85.37 \cdot 10^3$	$1.506 \cdot 10^3$	0.303
965 IC22+TWR	corsika	μ with $E^{-2.7}$ $600 < E_{CR} < 10^{11}$ $0^\circ < \theta < 90^\circ$	9973	$85.37 \cdot 10^3$	$1.507 \cdot 10^3$	0.3025
966 IC22+TWR	corsika	μ with $E^{-2.7}$ $600 < E_{CR} < 10^{11}$ $0^\circ < \theta < 90^\circ$	9999	$85.37 \cdot 10^3$	$1.507 \cdot 10^3$	0.303
861 IC22	corsika (coincident)	μ with $E^{-2.7}$ $600 < E_{CR} < 10^{11}$ $0^\circ < \theta < 90^\circ$	10000	$85.36 \cdot 10^3$	$1.336 \cdot 10^3$	7.083
909 IC22+TWR	ν -generator	ν_μ with E^{-2} $10 < E_\nu < 10^9$ $70^\circ < \theta < 180^\circ$	1000	$5.0 \cdot 10^5$	$1.398 \cdot 10^3$	3564.5

Table 6.2: *Simulated background datasets, divided into simulation production (simprod) datasets and event generators. IC22+TWR represents the combined 2007 detector, whereas IC22 stands for IceCube only. The corresponding detector live-time of a dataset is given by t_{live} . The number of generated, N_{gen} , and triggered, N_{trig} , events per dataset are averaged over all simulated files.*

All simulated signals are listed in detail in table 6.3, along with their effective volume (V_{eff}) at trigger level (see section 6.1.1), which is a quantity directly proportional to the sensitivity at trigger level. A larger V_{eff} for a particular annihilation channel indicates a higher sensitivity of the detector to this LKP signal. Additionally, the number of triggered signal events per annihilation channel per investigated

LKP mass is shown in figure 6.8. The number of triggered events, N_{trig} , for the direct neutrino annihilation channels is decreasing with rising mass. This effect is caused by the increasing opacity of the Sun for neutrinos with higher energies. On the other hand the detection probability for created muons in the combined detector increases with higher energies. Therefore, the softer channels (1, 2, 3, 4) experience a gain in N_{trig} .

$m_{B^{(1)}}$ in GeV/c^2	Annihilation Channel	N_{ann} in Sun	N_{trig}	$V_{eff,trig}$ in km^3
500	1	$2 \cdot 10^6$	173	$1.4 \cdot 10^{-2}$
	2	$2 \cdot 10^6$	470	$1.4 \cdot 10^{-2}$
	3	$2 \cdot 10^6$	$3.46 \cdot 10^3$	$6.7 \cdot 10^{-2}$
	4	$2 \cdot 10^6$	$12.50 \cdot 10^3$	$1.0 \cdot 10^{-1}$
	16	$2 \cdot 10^6$	$5.80 \cdot 10^3$	$3.3 \cdot 10^{-1}$
	17	$2 \cdot 10^6$	$9.37 \cdot 10^3$	$3.1 \cdot 10^{-1}$
	18	$2 \cdot 10^6$	$12.96 \cdot 10^3$	$2.2 \cdot 10^{-1}$
750	1	$2 \cdot 10^6$	265	$2.1 \cdot 10^{-2}$
	2	$2 \cdot 10^6$	760	$2.5 \cdot 10^{-2}$
	3	$2 \cdot 10^6$	$3.99 \cdot 10^3$	$8.6 \cdot 10^{-2}$
	4	$2 \cdot 10^6$	$14.03 \cdot 10^3$	$1.4 \cdot 10^{-1}$
	16	$2 \cdot 10^6$	$3.35 \cdot 10^3$	$4.9 \cdot 10^{-1}$
	17	$2 \cdot 10^6$	$3.74 \cdot 10^3$	$4.2 \cdot 10^{-1}$
	18	$2 \cdot 10^6$	$8.76 \cdot 10^3$	$2.2 \cdot 10^{-1}$
1000	1	$2 \cdot 10^6$	333	$2.7 \cdot 10^{-2}$
	2	$2 \cdot 10^6$	883	$3.0 \cdot 10^{-2}$
	3	$2 \cdot 10^6$	$4.21 \cdot 10^3$	$1.0 \cdot 10^{-1}$
	4	$2 \cdot 10^6$	$14.09 \cdot 10^3$	$1.6 \cdot 10^{-1}$
	16	$2 \cdot 10^6$	669	$4.9 \cdot 10^{-1}$
	17	$2 \cdot 10^6$	$2.11 \cdot 10^3$	$5.4 \cdot 10^{-1}$
	18	$2 \cdot 10^6$	$7.17 \cdot 10^3$	$2.2 \cdot 10^{-1}$

Table 6.3: Number of triggered events, N_{trig} , effective volume at trigger level, $V_{eff,trig}$ and number of simulated annihilations, N_{ann} , given for each simulated LKP mass $m_{B^{(1)}}$ and annihilation channel.

2007 was the first year in which the AMANDA array was integrated into the DAQ-system of IceCube. For the first time a combined detector analysis is possible. As a consequence of unexpected difficulties in the integration process throughout the year, the overall consensus in the collaboration was that very limited combined detector data is available. This consensus led to the decision that only IceCube 22 string (IC22) data was reprocessed in the time consuming reconstruction process, done within the collaboration.

Nevertheless, the author of this thesis discovered that more than 60 days of combined data is available for the analysis. Within the limited time frame of this thesis

it is not possible to reconstruct and process all ‘good’ runs by the author personally. A feasible option, which is considered and suggested by the author, including optimised pre-cuts and the need of a super computer, will be utilised to process all experimental data for a future unblinding proposal. The complete list of ‘good’ runs for the combined detector 2007 is shown in table B.1 in appendix B. In preparation, several experimental datasets that are divided into individual reconstructed runs and are listed in table 6.4, have been reconstructed to design an analysis, which can be performed as soon as all data is available. The chosen experimental datasets consist of experimental background data and experimental data. Experimental data is data taken before the 23rd September 2007, the day of the sunrise at the South Pole, including the (possible) LKP signal. Experimental background consists of runs where the Sun was above the horizon (zenith angles of less than 90° are excluded in the analysis) and is used as a real background sample to define the actual cut values. This is the best possible method of defining the final values of the cuts, which have been selected and designed with the simulated datasets, because this data sample consists of solely real background and is not sensitive to possibly wrongly simulated datasets. Additionally, the experimental background is independent of detector problems, which have not been identified, and are therefore reflected incorrectly in the simulation. The two major advantages compared to the simulated datasets are the independence from simulated ice properties and the missing coincident muon dataset, which are expected to be the dominant sources of errors within the simulated datasets of this analysis.

Experimental data	Run	Date	N_{trig}	t_{live} in days
Containing Signal	108727	16/06/2007	14969748	0.3336
	108729	16/06/2007	15034905	0.3335
	108732	16/06/2007	10182987	0.2265
	108734	17/06/2007	4166978	0.0925
	108736	17/06/2007	15010714	0.3335
	108738	17/06/2007	15027224	0.3343
	108740	17/06/2007	12037232	0.2676
	108743	18/06/2007	15102638	0.3335
	108745	18/06/2007	11796599	0.2611
	108747	18/06/2007	12999704	0.2871
	108749	19/06/2007	15033856	0.3347
	108751	19/06/2007	15033856	0.3335
	108753	19/06/2007	15050334	0.3335
	108755	20/06/2007	15048734	0.3335
	108759	20/06/2007	12998000	0.2800
	109352	20/09/2007	15941555	0.3346
	109353	21/09/2007	11503284	0.2265
	109354	21/09/2007	15815849	0.3124
109356	21/09/2007	15826981	0.3118	
Background	109364	24/09/2007	15658868	0.3120
	109365	24/09/2007	15700296	0.3336
	109366	24/09/2007	15666473	0.3120
	109375	25/09/2007	14368682	0.2860
	109376	25/09/2007	14654427	0.2909

Table 6.4: List of experimental datasets used to design cuts (Background) and to estimate the final sample (Containing Signal). The individual runs are listed by date, livetime, t_{live} , and number of triggered events, N_{trig} .

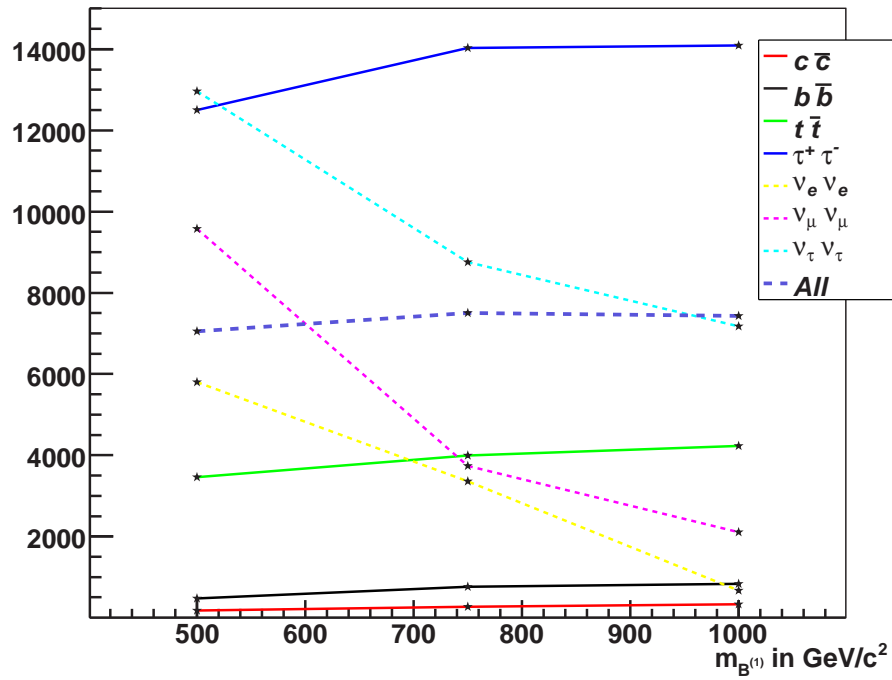


Figure 6.8: Number of triggered signal events in the combined IC22+TWR detector per annihilation channel, ch , and per LKP mass, $m_{B^{(1)}}$. All signals are simulated with $N_{ann} = 2 \cdot 10^6$. The dark-blue dotted line, corresponding to the channel All, represents the true expected LKP spectrum at trigger level, which is obtained by a weighted addition of the individual channels according to their expected branching ratios rescaled to a total branching ratio of 1.

Chapter 7

Analysis

This chapter summarises all methods of background rejection used in order to obtain the highest possible sensitivity of the combined detector (2007) for a KK-DM induced ν signal from the center of the Sun. Throughout the filtering process, the detailed directional information of each experimental event with regard to the Sun's position is unknown to avoid a bias in the applied set of selection criteria, called cuts, for each event. For this so called 'blind' analysis, all discussed datasets from section 6.3 are used in order to design and train the chosen cuts that are presented in the following sections. The simulated datasets fulfill two purposes. Firstly, the Monte Carlo (MC) simulations of the various background sources have to be in good agreement with the experimental values and parameters (section 7.1) to prove that a detailed understanding of the detector is achieved. Furthermore, they are used to select the different cut parameters for the cut levels $L2$, $L3$ and $L4$, because their dependencies on individual parameters can be tagged and the differences clearly identified. The actual cut value of each cut level is obtained by maximising the efficiency function, or a figure-of-merit (section 7.2.2), for the simulated LKP signals and the experimental background sample. Training cut values with experimental background datasets has the advantage of being free from possible simulation flaws and imperfectly matched coincident muon samples.

Bearing in mind that the LKP signals are point sources with very distinct directional limitations ($\Theta_{zen} = 90^\circ \pm 23^\circ$), the general strategy of the filtering is to apply strict directional cuts in early filter levels. Additionally, $L3$ picks reconstructed tracks, fulfilling criteria of horizontal tracks passing the detector, to further minimise vertical tracks associated with background events, before a neuronal-network and a support-vector-machine in the TMVA¹ based multivariant cut level $L4$ is trained [60, 61]. In $L5$, the search in solar direction, different statistical methods are utilised to derive the maximal sensitivity for LKP signals. One must note that the actual LKP spectrum is reflected by a composition of all simulated channels weighted respectively to their branching ratios. Therefore, the actual applied cut values at each filter level can differ from the optimised cut values of isolated anni-

¹(TMVA-v3.9.4) Toolkit for Multivariate Data Analysis together with ROOT-v5.18.00 was used in this thesis.

hilation channels. Nevertheless, all channels are processed individually throughout the various cut levels, which are determined by the composed LKP signal, in order to be able to perform the conversions from the final effective volumes V_{eff} correctly (section 7.3). All parameters, used in this analysis, are listed and defined in table 7.1.

7.1 Comparison with Experiment (MC vs Exp)

Understanding the detector characteristics is fundamental for a successful data analysis. Consequently, the simulated datasets have to agree very accurately with the experiment at an early stage of data processing. All parameters shown in figures 7.1, 7.2 and 7.3 are plotted after $L0$ and $L1$ filtering (see section 7.2.1 for detailed description of settings) and show several parameters, defining multiplicity, geometry and reconstruction of an event. At this filtering stage, all parameters, further used in the analysis are required to be in good agreement with the experimental datasets. The current simulation, using the AHA07v1 ice-model, oversimulates the number of triggered events. In addition, the simulated muon background flux is an annual averaged flux, and therefore doesn't account for seasonal variations. As a consequence, the simulated datasets are rescaled by a constant factor of 0.85 in the filtering process, to match the trigger rates of simulation and experiments. Since the experimental datasets are expected to be highly dominated by μ_{atm} , single muon and coincident muon datasets are combined to a total μ_{atm} background, which is required to resemble the experiment very precisely.

7.2 Cut Selections

7.2.1 $L0 + L1$: First Selection

$L0$ and $L1$ filtering occurs within the reconstruction process, thereby minimising the data volume for the interminable likelihood reconstruction. The $L0$ filter is a prefilter level to eliminate noise and 'bad' hits. In the first step, hits detected by broken or 'bad' DOMs are rejected, cross talk cleaning for AMANDA hits is performed, and all hits are feature extracted to identify individual pulses and peaks in the events. Then, the extracted pulse series of both detectors are combined, and hit cleaning is performed. Events are subjected to the local coincidence condition, the time window (TW) constraint, and isolated hit cleaning, which are listed in detail in table 7.2.

The $L1$ filter level in this analysis consists of three JEB-filters, which are used in the 'or' condition, allowing an event to pass the $L1$ filter when the event fulfills only one of the three filter conditions (see table 7.2 for detailed settings). The IceCube-Muon filter and the JAMS-Muon filter are upgoing muon filters, based on the two different first guess algorithms (see section 6.2.1). Both filters are designed to select upgoing, low energy muon tracks ($\Theta_{zen} > 80^\circ$), as the LKP signal ν is of

Parameter	Definition
n_{chan}	Number of hit DOMs
$n_{chan, fid}$	Number of hit DOMs in fiducial region
$n_{chan, twr}$	Number of hit AMANDA OMs
$n_{chan, veto}$	Number of hit DOMs in veto region
n_{str}	Number of hit strings
n_{hits}	Number of hits (DOM can have more than 1 hit)
z_{ext}	Extension of μ track in z direction in $[m]$ ($z_{ext} = z_{max} - z_{min}$)
accu time	Time till 75% of the total charge are accumulated in $[ns]$
separation	Distance between the calculated $cog(x, y, z, t_{1^{st}qu})$ and $cog(x, y, z, t_{4^{th}qu})$
cog x,y,z	Calculated center of gravity of an event in x,y,z direction in $[m]$
cog z sigm	Calculated uncertainty of the center of gravity in z direction
z_{trav}	Average drift of hits in z direction, calculated from $z_{av}(t_{1^{st}qu})$
amp per hit	charge per hit
t_{ext}	Temporal extension of time in $[ns]$ ($t_{ext} = t_{last} - t_{first}$)
tspread	combined parameter: (time ext/ n_{chan})
reco azi ϕ_{azi}	Reconstructed azimuth angle distribution in $[\circ]$
reco zen Θ_{zen}	Reconstructed zenith angle distribution in $[\circ]$
σ_{para}	Estimation of angular uncertainty of llh-reconstruction in $[\circ]$
rlh	Output value of loglikelihood fit divided by degrees of freedom
TW	Maximum time window for the event to happen in ns
$n_{dir,a}$	Number of direct hits in time interval $a = [-15ns, 25ns]$
$n_{dir,b}$	Number of direct hits in time interval $b = [-15ns, 75ns]$
$n_{dir,c}$	Number of direct hits in time interval $c = [75ns, 150ns]$
$n_{dir,d}$	Number of direct hits in time interval $d = [> 150ns]$
$n_{dir,e}$	Number of direct hits in time interval $e = [< -15ns]$
$n_{dir,all}$	$(n_{dir,a} + n_{dir,b} + n_{dir,c} + n_{dir,d} + n_{dir,e})$
$l_{dir,a}$	Largest distance of perpendicular projection onto recontrack of $n_{dir,a}$
$l_{dir,b}$	Largest distance of perpendicular projection onto recontrack of $n_{dir,b}$
$l_{dir,c}$	Largest distance of perpendicular projection onto recontrack of $n_{dir,c}$
$l_{dir,d}$	Largest distance of perpendicular projection onto recontrack of $n_{dir,d}$
$l_{dir,all}$	$(l_{dir,a} + l_{dir,b} + l_{dir,c} + l_{dir,d} + l_{dir,e})$
t_{res}	residual time of $t_{res} = t_{hit} - t_c$ in $[ns]$; $t_c = \text{distance}(\text{vertex-OM})/c_M$
$n_{dir,a}^{str}$	Number of hit strings with $n_{dir,a}$
$n_{dir,b}^{str}$	Number of hit strings with $n_{dir,b}$
$n_{dir,c}^{str}$	Number of hit strings with $n_{dir,c}$
$n_{dir,d}^{str}$	Number of hit strings with $n_{dir,d}$
$n_{dir,a+b}^{str}$	$(n_{dir,a}^{str} + n_{dir,b}^{str})$
hit oms	Distribution of hit OMs in the Ice; DOM[0] is the uppermost
ρ_{av}	$\sum_{i=1}^{allstrings} \sum$ of shortest distance from track to string per n_{chan} ; in $[m]$

Table 7.1: Parameters available and used in analysis for filtering and to design cuts. $t_{1^{st}qu}$ and $t_{4^{th}qu}$ correspond to the first and respectively fourth quartile of hits, ordered in time for an event. c_M is the speed of light in medium.

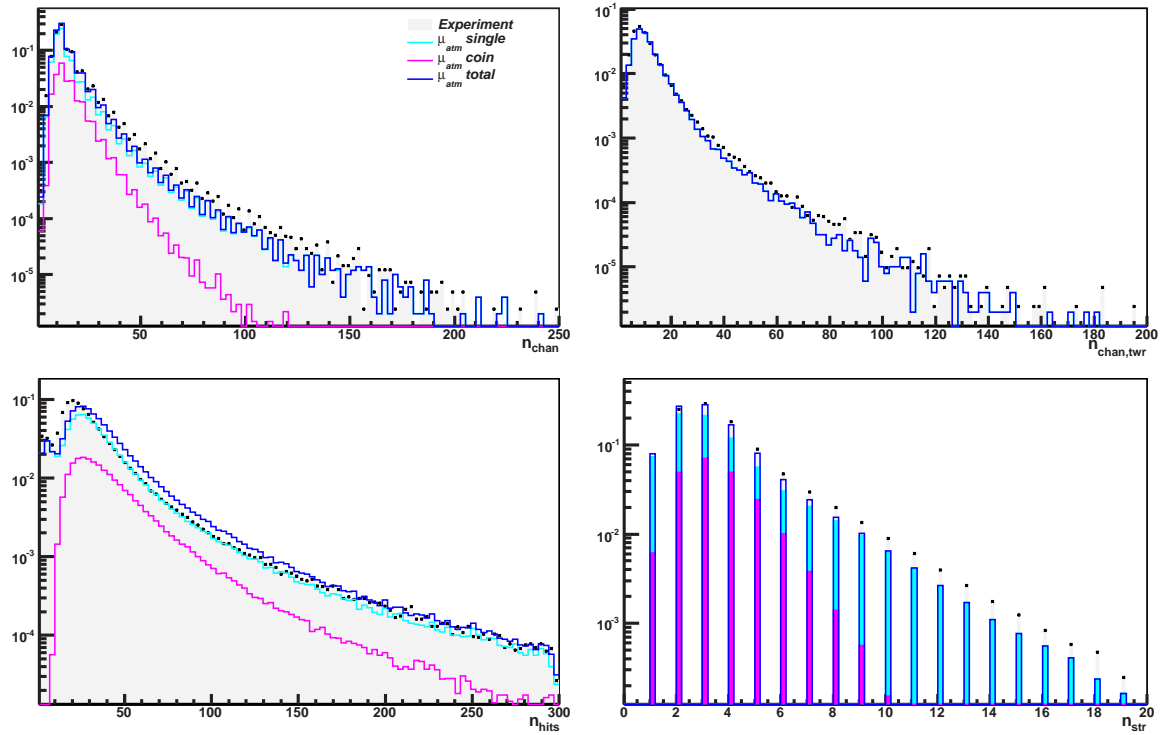


Figure 7.1: Multiplicities MC vs. background. Single μ_{atm} (light blue) and coincident μ_{atm} (purple) are combined in a total μ_{atm} (dark blue) and compared to the experimental data, indicated by black squares (area shaded in grey). Experiment and combined μ_{atm} are rescaled to 1 for accurate comparison. Top left is the number of hit channels, top right the number of TWR channels, bottom left is the number of extracted hits, and bottom right is the number of hit strings (see table 7.1 for details about parameters).

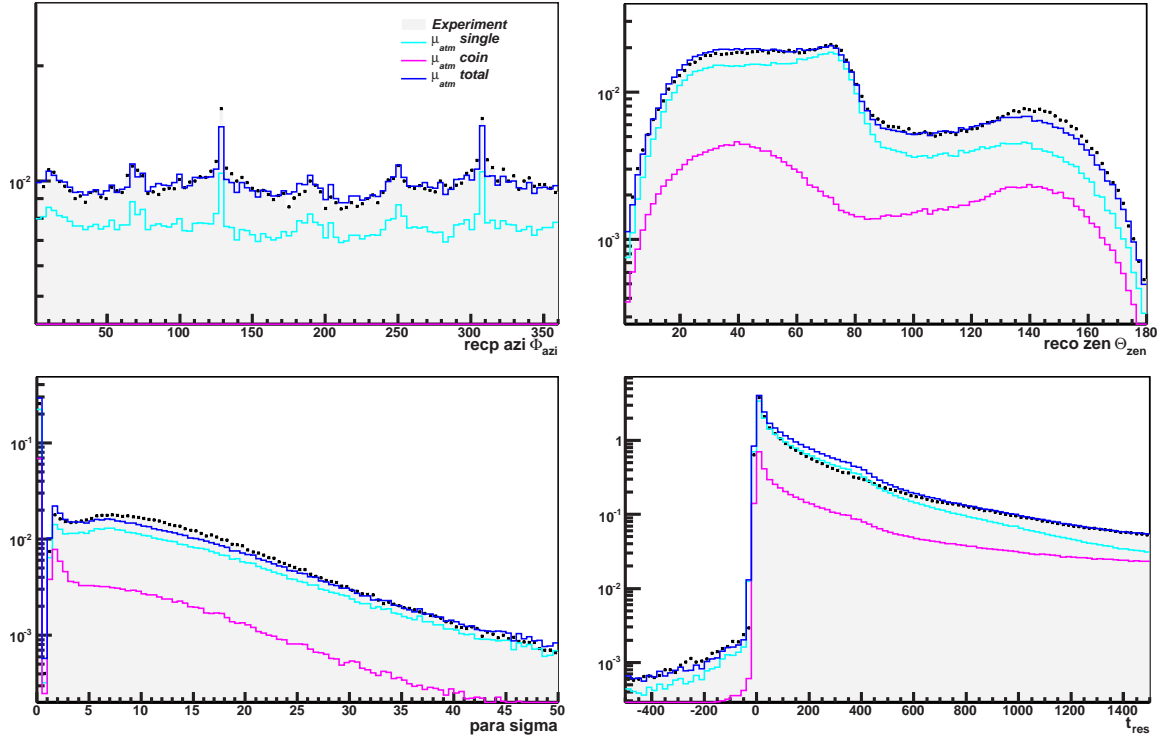


Figure 7.2: Reconstruction parameters MC vs. background. Single μ_{atm} (light blue) and coincident μ_{atm} (purple) are combined in a total μ_{atm} (dark blue) and compared to the experimental data, indicated by black squares (area shaded in grey). Experiment and combined μ_{atm} are rescaled to 1 for accurate comparison. Top left is the distribution of reconstructed azimuth angles, top right the distribution of reconstructed zenith angles, bottom left is the paraboloid sigma distribution, and bottom right the time residuals (see table 7.1 for details about parameters).

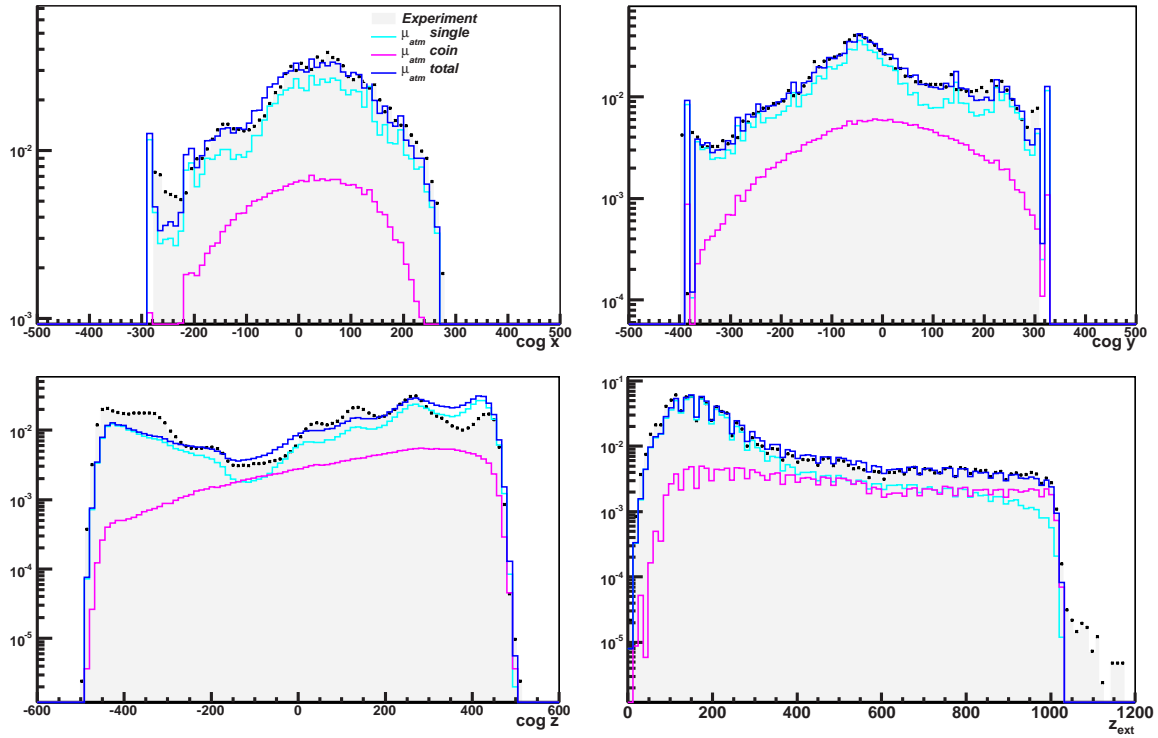


Figure 7.3: Geometry parameters MC vs. background. Single μ_{atm} (light blue) and coincident μ_{atm} (purple) are combined in a total μ_{atm} (dark blue) and compared to the experimental data, indicated by black squares (area shaded in grey). Experiment and combined μ_{atm} are rescaled to 1 for accurate comparison. In the order of top left, top right and bottom left the center of gravity for x , y , and z direction is shown. The bottom right diagram shows the z extension distribution (see table 7.1 for details about parameters).

very low energy, with an overall expected maximum of 1000 GeV. Additionally, they require a certain minimum number of hit DOMs, in order to ensure an accurate track reconstruction. Nevertheless, both upgoing filters do not demand a neutrino interaction vertex inside the detector volume and therefore also detect muons created in CC interactions outside the detector, as well as atmospheric muons. The third $L1$ filter, the contained event filter, selects events with an interaction vertex inside the fiducial volume of the detector.

$L0$	$L1$ IceCubeMuon	$L1$ JAMSMuon	$L1$ Contained
LC2	min 10 $n_{hits,IC}$	min 13 $n_{hits,twr}$	min 4 $n_{hits,fid}$ no $n_{hits,veto}$
TW < 6000 ns	linefit $\Theta_{zen} > 80^\circ$	max 20 $n_{hits,IC}$	1 st $n_{hits,veto}$ later 4 th $n_{hits,fid}$
$n_{hits,iso}$:		JAMS $\Theta_{zen} > 80^\circ$	$z_{trav} > -40$ m
$R < 300$ m			
$t_{hit} < 2000$ ns			

Table 7.2: Filter settings at $L0 + L1$ level. $L0$ is the prefilter level, cleaning events of noise (LC2) and isolated hits ($n_{hits,iso}$), as well as setting a maximum time window (TW) for the event of 6000 ns. At $L1$, all three JEB filters (IceCubeMuon, JAMSMuon and Contained) are listed with the individual settings, used in this analysis. For an explanation of the individual parameters, see table 7.1.

Contained Event Filter

The contained event filter divides the combined detector into veto and fiducial regions (shown in figure 7.4) to distinguish between charged particles created inside or outside the fiducial volume. μ_{atm} and particles created outside the detector emit light prior to entering the detector volume. As a consequence, the first hits are detected at the outermost DOMs (veto region) and the events can be rejected. The contained event filter has three conditions. The first is set to detect no hits in the veto region, but a minimum of 4 hits in the fiducial region. The second condition requires that the first veto hit must be later than the 4th fiducial hit. This allows to trigger events, which are generated inside the fiducial volume, but leave the detector on a track passing through the veto region. The third requirement, to be fulfilled by an event, either passing condition one or two, is $z_{trav} > -40$ m. z_{trav} defines the average drift of an event in z direction. It compares the average z -position of the first quartile of hits, to the z -position of all later hits, which can be written as,

$$z_{trav} = \sum_{i=p}^{n_{hits}} (z_i - \langle z \rangle_{1st_{qu}}) / (n_{hits} - p) \quad \text{with} \quad \langle z \rangle_{1st_{qu}} = \sum_{i=0}^p z_i / p. \quad (7.1)$$

The vertex positions of events passing the different $L1$ filters, after $L0 + L1$ filtering is shown in figure 7.5. Resulting trigger rates for the datasets at level $L0 + L1$ are summarised in table 7.3. The cut efficiency is listed in table 7.4.

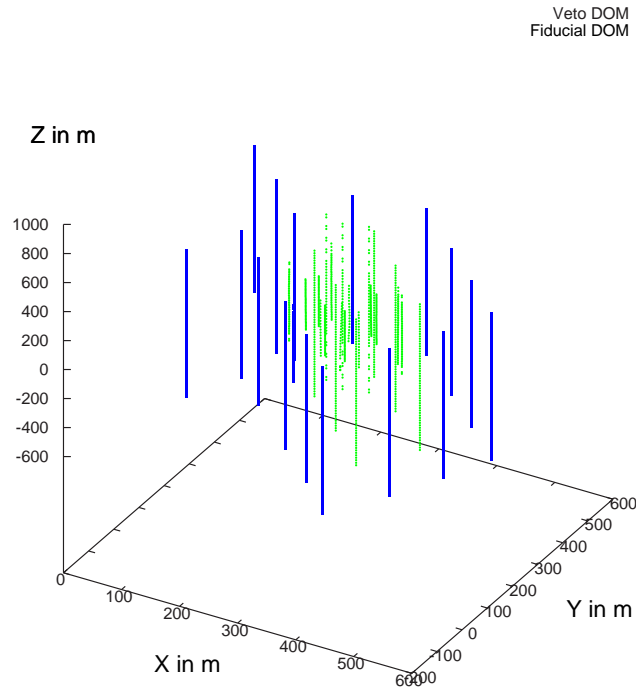


Figure 7.4: This figure illustrates the distinction between veto strings (blue) and fiducial strings (green) in the combined 2007 detector. The zero point marks the origin in the detector coordinate system at an absolute depth of 1730 m from the surface.

Level	Experiment	Total μ_{atm}	Single μ_{atm}	Coincident μ_{atm} (IC22 only)	ν_{atm}
Trigger level	603 Hz	597 Hz	575 Hz	21.8 Hz	4.55 mHz
L0 + L1	17 Hz	20.4 Hz	16.2 Hz	4.2 Hz	3.06 mHz
L2	0.33 Hz	0.41 Hz	0.24 Hz	0.17 Hz	0.69 mHz
L3	0.16 Hz	0.16 Hz	0.12 Hz	0.04 Hz	0.67 mHz
L4	0.47 mHz	0.11 mHz	0.07 mHz	0.04 mHz	0.34 mHz
L5	7.0 μ Hz	2.1 μ Hz	1.1 μ Hz	1.0 μ Hz	5.0 μ Hz

Table 7.3: Trigger rates at different filter levels for the different datasets. The event rate for the total μ_{atm} background is obtained by adding the individual rates of single μ_{atm} and coincident μ_{atm} background. All simulated datasets are compared to the real experimental rate.

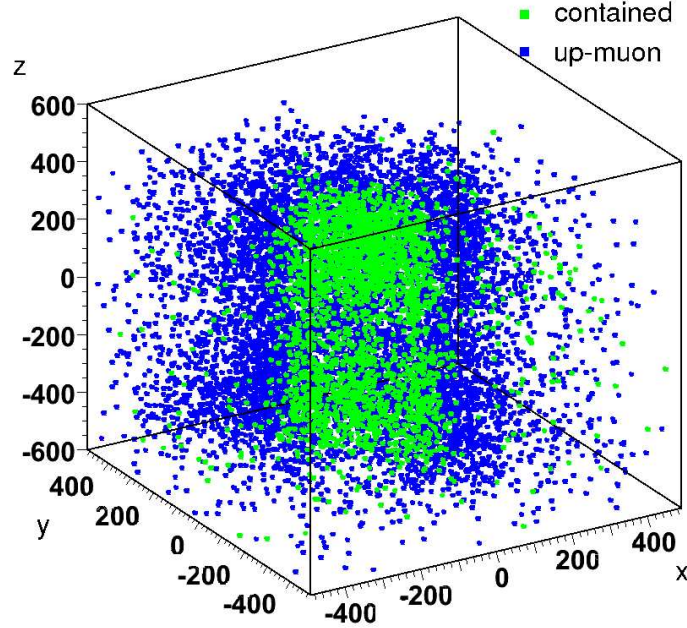


Figure 7.5: Vertex positions of events passing the different $L1$ filters. Events passing the Contained event filter are marked in green, whereas events passing either the IceCubeMuon or the JAMSMuon filter are marked in blue. The vertices shown here are for one LKP signal ($m_{B^{(1)}} = 500 \text{ GeV}/c^2$, $ch = 18(\nu_\tau \bar{\nu}_\tau)$). It can be clearly seen that events passing the Contained event filter are well confined within the instrumented detector volume.

7.2.2 L2: Cut in Solar Region

All events passing the $L0+L1$ filter are likelihood reconstructed (see section 6.2.2 for details). The level 2 filter is a two dimensional cut on the reconstructed iterative-fit zenith angle ($\Theta_{zen,llh}$) and the angular uncertainty of the reconstructed track, given by the paraboloid sigma value (σ_{para}). Figure 7.6 shows the individual parameters, as well as the 2-dim scatter profile for the LKP signal compared to experiment and simulated backgrounds. Naively, one would set the cut for $\Theta_{zen,llh}$ within the solar zenith region of $[90^\circ, 113^\circ]$. In the following section different calculation methods for cut efficiencies, that were used for finding the best set of cut parameters in the early filter levels, are presented and compared. Utilising these methods, the following $L2$ cut values are found:

$$\begin{aligned}
 90^\circ &\leq \Theta_{zen,llh} \leq 116^\circ \\
 \sigma_{para} &< 10^\circ \\
 \sigma_{para} &> 0 \\
 n_{str} &> 1
 \end{aligned}
 \tag{7.2}$$

In some cases, the llh reconstruction algorithm fails finding a best fit. Therefore, the existence of σ_{para} is an additionally requirement for the upper cut on the angular

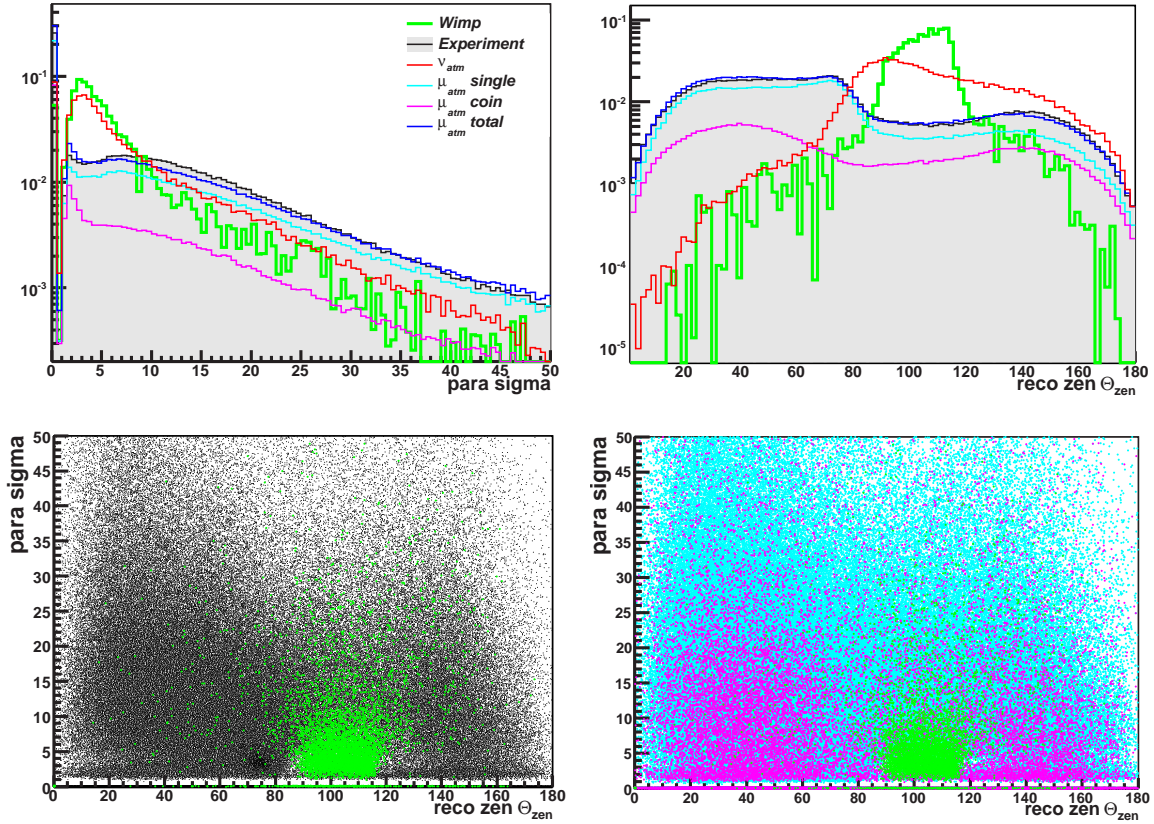


Figure 7.6: $L2$ filter parameters. Different datasets are indicated by colours. Single μ_{atm} (light blue) and coincident μ_{atm} (purple) are combined in a total μ_{atm} (dark blue) and experimental data is indicated by black squares (area shaded in grey). LKP signal (green) and ν_{atm} background (red) are rescaled to 1, as well as experiment and combined μ_{atm} for accurate comparison. The top left figure shows the angular error σ_{para} and the top right the reconstructed zenith angle distribution Θ_{zen} . The bottom two 2-dimensional scatter profiles illustrate the σ_{para} - Θ_{zen} dependency for signal & experiment (bottom left), and signal & simulated μ_{atm} (bottom-right).

uncertainty. $L2$ also excludes single string events, because they imply almost vertical muon tracks, which are not valid track solutions for $\nu_{B(1)}$ from the centre of the Sun. This filter degrades initially triggered $\mu_{atm,total}$ by more than 99.9%. Cut efficiencies and trigger rates for $L2$ are listed in tables 7.3 and 7.4.

Cut Value Calculations

There are various ways to determine the most efficient cut values for different parameter distributions of background and signal. In general, the methods discussed here are only found to be suitable for parameter distributions that differ significantly for background and signal. For distributions with only marginal differences, multi-variant approaches, as discussed in section 7.2.4, are a far more successful solution.

The simplest figure-of-merit to define a cut value is given by

$$x = \frac{N_{sig}}{\sqrt{N_{bg}}} . \quad (7.3)$$

This figure can be evaluated at each bin, in order to find the maximum value, defining the cut value. This method is found to be too inaccurate and is not used in the analysis. Better results are obtained by maximising

$$\epsilon_{cut1} = eff_{sig}(1 - eff_{Bg}) , \text{ or} \quad (7.4)$$

$$\epsilon_{cut2} = \frac{eff_{sig}}{\sqrt{eff_{Bg}}} , \quad (7.5)$$

which depend on the signal and background efficiency per bin, given by $eff_{sig} = N_{sig,cut}/N_{sig,total}$ and $eff_{Bg} = N_{Bg,cut}/N_{Bg,total}$. The cut values that are determined by both methods are very similar. A cut limiting the left side of a given distribution is obtained by integration from the right-upper end of the parameter distribution, whereas cuts on the right part of the distribution are consequently derived by an integration from the left-lower end of the spectrum. The values from method ϵ_{cut2} represent, in the case of the $L2$ distributions, a slightly softer cut space. Consequently, the final $L2$ cut values for the 2 dimensional cut are defined by the maximum of ϵ_{cut1} , which is illustrated for the $\Theta_{zen,llh}$ distribution in figure 7.7.

7.2.3 L3: Horizontal Selection

This cut level is devoted to further selecting events with horizontal and contained tracks. The concept of the $L3$ cut concerning the multivariant $L4$ cut, is to select dataset samples of very similar tracks, with respect to direction and brightness. The more similar the reconstructed background tracks match the signal tracks in these parameters, the more distinct and effective other parameter differences become in the $L4$ cut, and background reduction can be optimised. The actual cut values of the parameters, presented in equation 7.6, are obtained without maximising a figure-of-merit or other optimisations. The values are simply set to remove the tails in the distributions of the parameters (illustrated in figure 7.8).

$$\begin{aligned} -25 \text{ m} &< z_{trav} < 125 \text{ m} \\ \rho_{av} &< 80 \text{ m} \\ z_{ext} &< 350 \text{ m} \end{aligned} \quad (7.6)$$

The z_{trav} interval limits too steeply downgoing, as well as upgoing events, whereas the z_{ext} cut puts an upper boundary on the event extension in z -direction within the detector. This cut additionally improves the ratio of horizontal to vertical events, as horizontal events are generally more limited in z_{ext} . ρ_{av} is a quantity, defining the average shortest distance from a string with a hit DOM, to the reconstructed track.

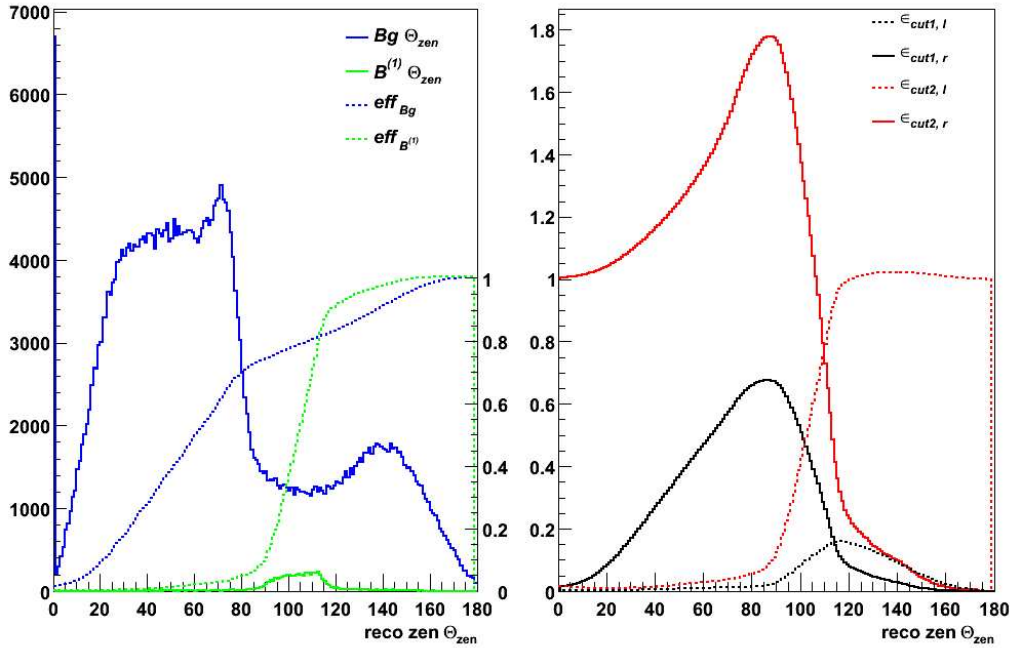


Figure 7.7: The left diagram shows the unscaled $\Theta_{zen,llh}$ distribution before the $L2$ cut for the $B^{(1)}$ signal in green and the total $\mu_{atm,total}$ background in blue, as well as their efficiencies (also called purity), indicated by the green (signal) and blue (background) dotted lines. The right diagram presents the distribution of the two chosen optimisations, ϵ_{cut1} in black and ϵ_{cut2} in red. The indices r (solid lines) and l (dotted lines) stand for integration from the right or left end of the distribution, in order to obtain the left and right cut values, indicated by the maxima.

Smaller average distances indicate more horizontal and contained events. Overall, the coincident μ_{atm} background rate is abated effectively by this cut. The individual parameters are shown in figure 7.8 and cut results for the respective datasets are summarised in tables 7.3 and 7.4.

7.2.4 L4: Multivariant Background Rejection

The multivariant filter level, $L4$, consists of a combination of two different TMVA routines to determine accurately between signal and background. The two parameter sets for the routines are obtained by choosing parameters with low correlation, but high discrimination power between background and signal. Furthermore, the background rejection efficiencies of all available TMVA routines are determined in test-trials. As a result, a support vector machine (SVM) together with a Gaussian fit-function and a neural network (NN) are found to be most suitable for the $L4$ cut. The NN, depending on six input parameters (σ_{para} , z_{trav} , r_{llh} , $accu\ time$, $l_{dir,all}$, $n_{dir,b}^{str}$) with two hidden layers ($N+1$, N), is trained and tested on a specifically chosen signal and background sample. The additional simulated signal, produced specifically for

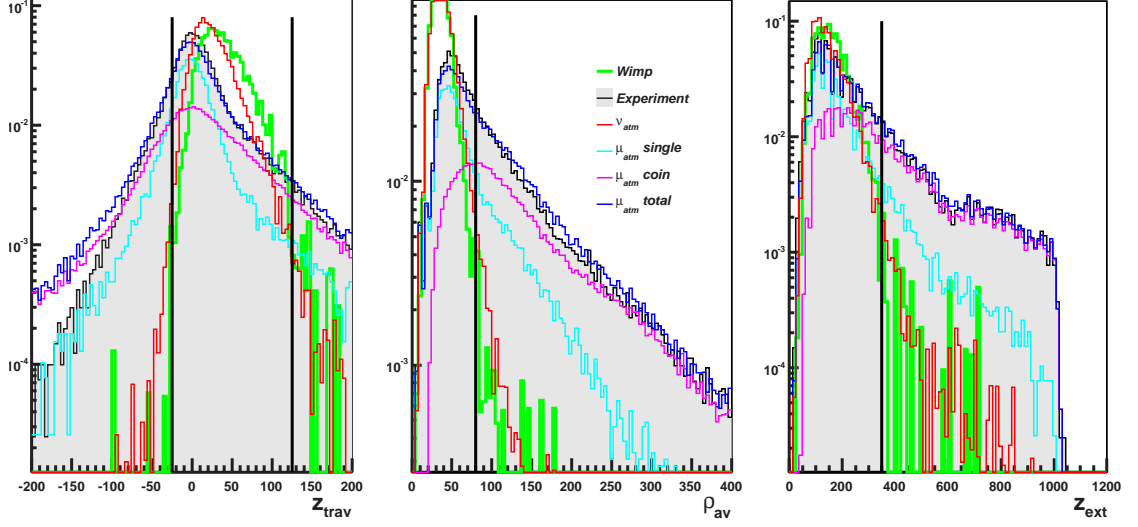


Figure 7.8: *L3 filter parameters. Datasets are indicated by their colours. Single μ_{atm} (light blue) and coincident μ_{atm} (purple) are combined in a total μ_{atm} (dark blue), and experimental data is indicated by black squares (area shaded in grey). LKP signal (green) and ν_{atm} background (red) are rescaled to 1, as well as experiment and combined μ_{atm} for accurate comparison. The left diagram shows the z_{trav} parameter. The diagram in the middle the ρ_{av} and the right diagram the z_{ext} distribution. The actual cut values are indicated by the vertical solid black lines for each parameter.*

this cut, is exactly split in half for testing and training ($m_{B^{(1)}} = 750 \text{ GeV}/c^2$, $ch = 18(\nu_\tau\bar{\nu}_\tau)$, $N_{ann} = 2 \cdot 10^6$) as is the experimental background sample. Both datasets are discarded after training and testing, in order to be unbiased in the final steps of the analysis. The second routine, the SVM, is trained and tested on the same subsamples of data for seven different input parameters ($cog z$, $n_{dir,a}$, $l_{dir,b}$, $n_{dir,a+b+c}^{str}$, ρ_{av} , separation, $(\Theta_{zen,llh} - \Theta_{zen,linefit})$). The output parameters of both routines classify events as background-like (NN(-1), SVM(0)) and signal-like (NN(1), SVM(1)) by assigning each tested event the parameters Q_1 (SVM) and Q_2 (NN) ranging within the routines Q -values. The individual output parameters are combined in one multivariate cut parameter $Q_1 \cdot Q_2$ to further optimise the discrimination power of the individual routines. The resulting Q_1 , Q_2 and $Q_1 \cdot Q_2$ distributions are shown in figure 7.9, as well as a 2-dimensional scatter profile of Q_1 and Q_2 to further illustrate their dependency. The *L4* cut values are set to:

$$\begin{aligned}
 Q_1 &> 0.45 \\
 Q_2 &> 0.45 \\
 Q_1 \cdot Q_2 &> 0.2025 \\
 n_{str} &> 2 \\
 n_{dir,a+b+c}^{str} &> 4
 \end{aligned} \tag{7.7}$$

To further diminish the atmospheric background, additional cuts on the number of hit strings n_{str} , and the number of hit strings with direct hits in a combined time

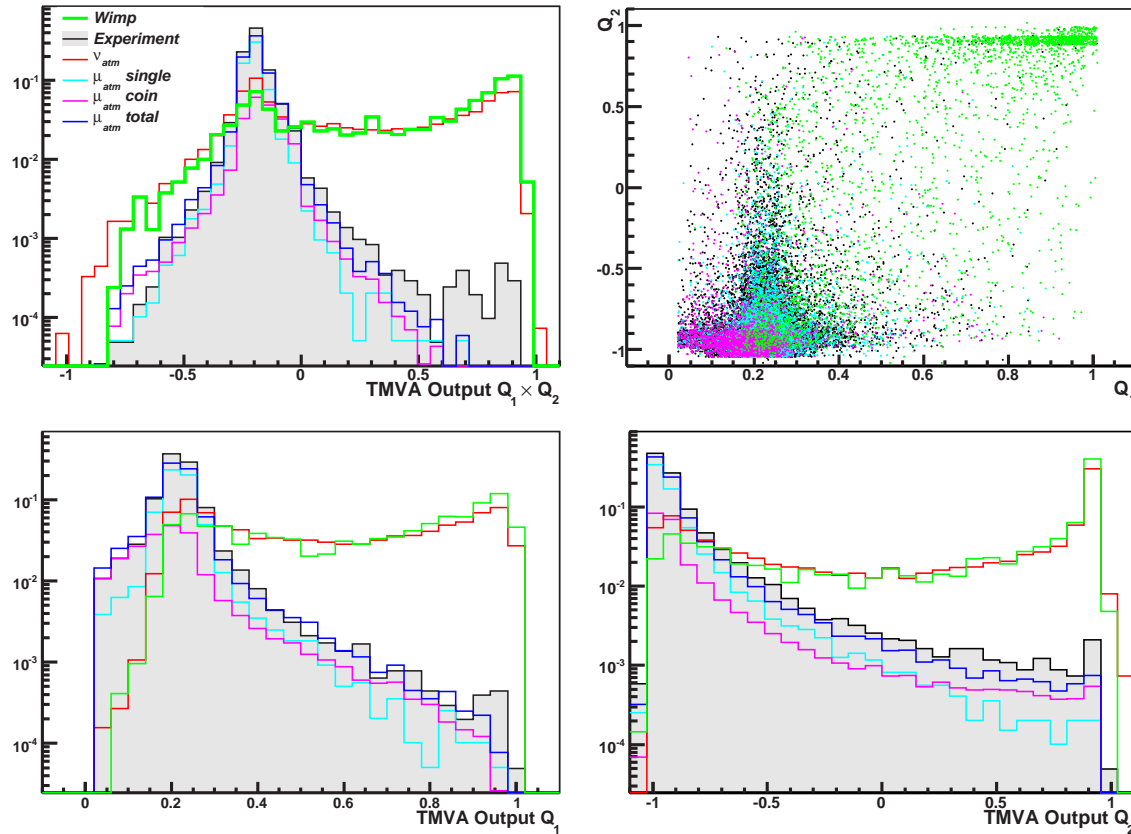


Figure 7.9: *TMVA cut parameters. The two bottom diagrams show the multivariate output parameter distributions Q_1 (SVM) and Q_2 (NN) for the different datasets, the top-left diagram the distribution of the combined TMVA parameter $Q_1 \cdot Q_2$. In the 2-dimensional scatter plot at the top-right, the Q_1 dependency on Q_2 for the various datasets is illustrated.*

interval $[a + b + c]$ are applied. These two cuts further support the selection of horizontal tracks and are applied after the multivariate cut is performed. Resulting efficiencies at level 4 are summarized in tables 7.3 and 7.4.

7.2.5 L5: Solar Search Cone

After the $L4$ cut, the μ_{atm} background reduction is $< 1.16 \cdot 10^{-7}$, which implies that the final surviving events in the final sample are dominated by ν_{atm} background. The solar search is looking for an excess in neutrino events over the expected background in a specifically determined search cone with a half opening angle Ψ . The simplest approximation for ν_{atm} is to assume an isotropic distribution. Therefore, the number of background ν events found in the search cone can be determined by

$$n_{\Psi} = \frac{n_{sky} \cdot \Omega_{\Psi}}{\Omega_{sky}}, \quad (7.8)$$

where n_{sky} is the number of remaining ν_{atm} after $L4$ cut within the detector livetime T_{live} . Ω_{Ψ} is the solid angle of the chosen search cone, and Ω_{sky} the solid angle of the remaining LKP search region, given by $90^\circ < \Theta < 116^\circ$, $0^\circ < \phi < 180^\circ$. However, the ν_{atm} distribution at $L5$ depends on the angular reconstruction efficiency of the llh algorithm for different zenith angles and is therefore specified by the ν_{atm} $\Theta_{zen,llh}$ distribution. Consequently, the real background distribution is given by a probability density function $f_{Bg}(x|\Psi)$ of finding an event x given a certain search cone angle Ψ . The p.d.f. f_{Bg} is determined by performing a sufficiently large number of test experiments, where the opening angle between the ν_{atm} event and the sun direction is given by,

$$2\Psi = \arccos(\vec{r}_{sun} \cdot \vec{r}_{test}) \quad \text{with} \quad |\vec{r}_{sun}| = |\vec{r}_{test}| = 1, \quad (7.9)$$

where f_{Bg} is rescaled to a total probability of one. The real expected background p.d.f. is obtained by multiplying f_{Bg} with the total number of background events expected within T_{live} ($\nu_{atm} + \mu_{atm,single} + \mu_{atm,double}$). $f_S(x|\Psi)$, the p.d.f. for finding a signal event x within Ψ , is given by the total angular difference between the initial MC track and the final reconstructed track. Such a signal p.d.f. can be calculated for each individual channel. As the LKP signal is determined by a composition of all simulated annihilation channels, the search cone optimisation is performed on a combined $f_S^{all}(x|\Psi)$ given by all seven channels, added together according to the expected branching ratios listed in table 3.1. $f_S^{all}(x|\Psi)$ is rescaled to unit area before it is multiplied by the weighted sum of all remaining events of the seven different annihilation channels. Figure 7.10 shows the combined signal p.d.f. $f_S^{all}(x|\Psi)$ and the expected background p.d.f. $f_{Bg}(x|\Psi)$. It is clear that in the left diagram the combined signal p.d.f. is broadened with respect to $f_S^{ch17}(x|\Psi)$. This behaviour is expected as $ch17$ is a very hard channel with more accurately reconstructed muon tracks.

In the process of finding the optimum half opening angle Ψ of the solar search cone, which results in the highest possible sensitivity for the combined detector 2007 with a total livetime $T_{live} = 60$ d, three different optimisations were investigated:

$$\begin{aligned} \epsilon_1(\Psi) &= \frac{\sqrt{n_{Bg}}}{n_s} \\ \epsilon_2(\Psi) &= \frac{\sqrt{eff_{Bg}}}{eff_s} \\ MRF &= \frac{\bar{\mu}_s^{90\%}}{n_s} \end{aligned} \quad (7.10)$$

n_s and n_{Bg} are the number of signal, respectively background events in the cone, whereas eff_s and eff_{Bg} define the signal and background efficiency of the chosen search cone (see section 7.2.2). $\bar{\mu}_s^{90\%}$ is the average Feldman-Cousins 90% confidence upper limit on the expected signal $\mu_s^{90\%}$ [62]. $\bar{\mu}_s^{90\%}$ is used to estimate an upper limit for the sensitivity of an experiment, without looking at the actual data. The so called Feldman-Cousin sensitivity is determined for experiments under the assumption of m hypothetical repetitions of the same experiment with an expected background n_{Bg} and no true observed signal ($n_s = 0$) [63]. The average upper limit is given

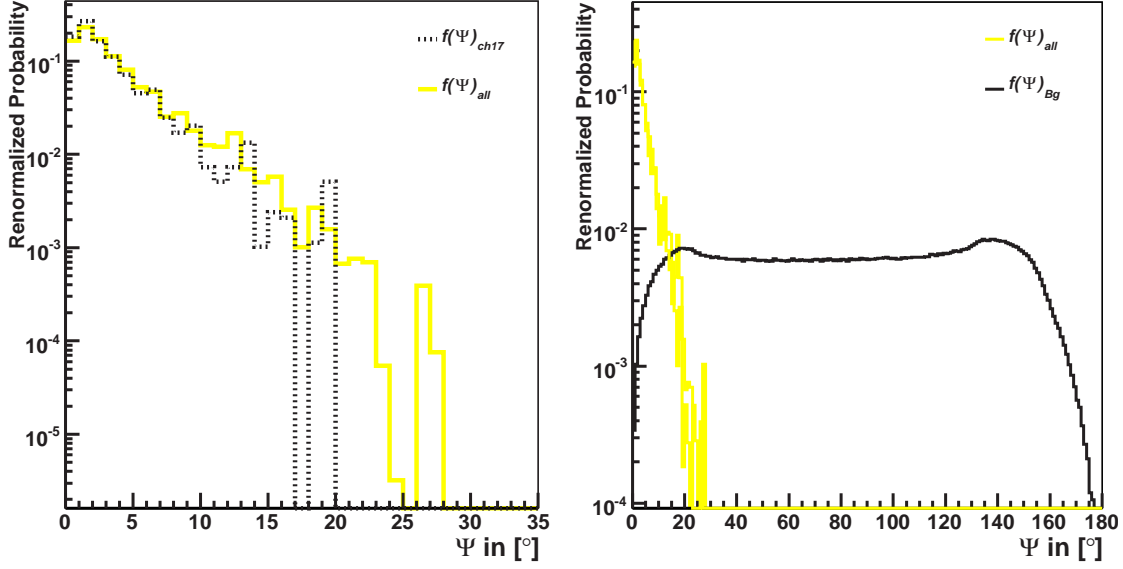


Figure 7.10: Signal and Background p.d.f. at level L5. The left diagram shows a close up of $f_S^{all}(x|\Psi)$ compared to $f_S^{ch17}(x|\Psi)$ in the relevant Ψ -range, whereas the right diagram illustrates the Ψ distribution of $f_{Bg}(x|\Psi)$ compared to $f_S^{all}(x|\Psi)$.

by the sum over all hypothetically observed events n_{obs} in the pseudo experiments weighted by their Poisson probability of occurrence,

$$\bar{\mu}_s^{90\%}(n_{Bg}) = \sum_{n_{obs}=0}^{\infty} \mu_s^{90\%}(n_{obs}, n_{Bg}) \frac{(n_{Bg})^{n_{obs}}}{(n_{obs})!} e^{-n_{Bg}} . \quad (7.11)$$

The model rejection factor (MRF) is used to determine the optimised search cone angle Ψ , because the conversion rate for neutrinos-to-muons $\bar{\Gamma}_{\nu \rightarrow \mu}^{90\%}$ is directly proportional to the MRF² (see equation 7.12 and section 7.3 for details). All investigated optimisation methods are plotted for the $m_{B(1)} = 500 \text{ GeV}/c^2$ case in figure 7.11 and the obtained values for Ψ are listed in table 7.5.

²this assumption is valid, because the effective Volume V_{eff} is directly proportional to n_s .

Dataset	ch	$L0 + L1$	$L2$	$L3$	$L4$	$L5$
500 GeV/c^2	1	0.70	0.29	0.29	0.07	0.05
	2	0.62	0.28	0.28	0.06	0.03
	3	0.66	0.36	0.35	0.13	0.08
	4	0.65	0.38	0.37	0.15	0.09
	16	0.71	0.46	0.45	0.24	0.16
	17	0.71	0.46	0.44	0.23	0.15
	18	0.67	0.42	0.40	0.19	0.12
750 GeV/c^2	1	0.68	0.33	0.33	0.06	0.03
	2	0.66	0.30	0.30	0.08	0.04
	3	0.66	0.38	0.37	0.14	0.07
	4	0.66	0.40	0.38	0.17	0.07
	16	0.73	0.50	0.49	0.25	0.14
	17	0.72	0.49	0.48	0.25	0.14
	18	0.68	0.41	0.40	0.18	0.10
1000 GeV/c^2	1	0.67	0.28	0.28	0.07	0.03
	2	0.67	0.30	0.30	0.10	0.05
	3	0.66	0.37	0.37	0.15	0.07
	4	0.68	0.41	0.40	0.17	0.08
	16	0.73	0.50	0.49	0.28	0.16
	17	0.74	0.50	0.49	0.27	0.14
	18	0.68	0.41	0.41	0.18	0.08
$\mu_{atm,single}$	–	$2.8 \cdot 10^{-2}$	$4.14 \cdot 10^{-4}$	$2.10 \cdot 10^{-4}$	$1.16 \cdot 10^{-7}$	$3.3 \cdot 10^{-9}$
$\mu_{atm,double}$	–	0.21	$7.98 \cdot 10^{-3}$	$1.85 \cdot 10^{-3}$	$1.87 \cdot 10^{-6}$	$4.5 \cdot 10^{-8}$
ν_{atm}	–	0.71	0.153	0.147	0.06	$9.5 \cdot 10^{-4}$
Experiment Bg	–	$2.8 \cdot 10^{-2}$	$5.41 \cdot 10^{-4}$	$2.69 \cdot 10^{-4}$	$6.97 \cdot 10^{-7}$	$8.9 \cdot 10^{-9}$
Experiment	–	$2.8 \cdot 10^{-2}$	$5.37 \cdot 10^{-4}$	$2.67 \cdot 10^{-4}$	$7.4 \cdot 10^{-7}$	$9.0 \cdot 10^{-9}$

Table 7.4: *Cut efficiencies. For all datasets used in this analysis, the individual cut efficiencies of each cut level are summarised and normalised to 1 at trigger level. The Experiment Bg dataset (taken when the Sun is above the horizon) is used for finding actual cut values.*

$m_{B(1)}$ in GeV/c^2	MRF(Ψ) in $[\circ]$	$\epsilon_1(\Psi)$ in $[\circ]$	$\epsilon_2(\Psi)$ in $[\circ]$	$n_{Bg}(\Psi)$ in 60 days
500	3.5	3.5	3.5	58
750	2.75	2.5	2.5	41
1000	2.5	2.0	2.0	35

Table 7.5: *Best fit values for solar search cone Ψ listed for the investigated methods MRF, $\epsilon_1(\Psi)$, and $\epsilon_2(\Psi)$. $n_{Bg}(\Psi)$ is the number of background events found in the search cone with $T_{live} = 60$ d for the best fit value of the chosen fit method, the MRF optimisation.*

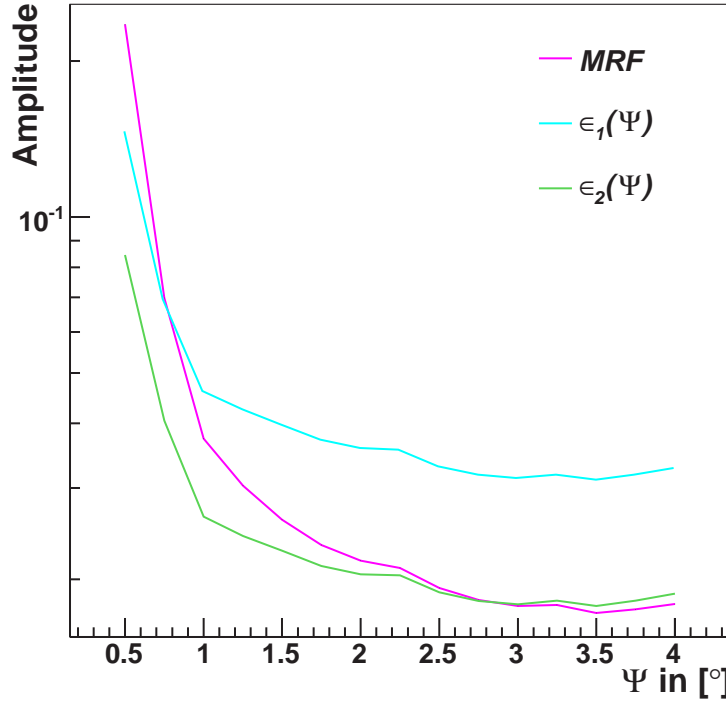


Figure 7.11: Optimisation of half opening angle of the solar search cone Ψ , plotted for the $m_{B(1)} = 500 \text{ GeV}/c^2$ combined $f_S^{all}(x|\Psi)$. The minimum determines the best value for Ψ .

7.3 Sensitivity

As the processing of the complete experimental data (60 days) would exceed the available time frame of this thesis, a real limit on the Kaluza Klein induced muon flux from the core of the Sun cannot be set. However, under the assumption of no signal detection, it is possible to derive the above discussed Feldman-Cousin sensitivity for the combined detector with a total livetime of $T_{live} = 60 \text{ d}$. The expected experimental events after cut level $L4$ are estimated from the processed experimental subset, which has a corresponding detector livetime of 5.61 d. The results are then extrapolated to the total livetime T_{live} . Therefore, a final sample of 2380 experimental events is expected for the ‘unblinding’ stage of this analysis. This quantity is precisely predicted by the simulated MC background samples, surviving the $L4$ filter extrapolated to T_{live} ($211(\mu_{atm,coin}) + 346(\mu_{atm,single}) + 1780(\nu_{atm}) = 2337(n_{Bg,MC})$).

The physical quantity that neutrino telescopes measure directly or set limits on, is the neutrino-to-muon conversion rate $\bar{\Gamma}_{\nu \rightarrow \mu}^{90\%}$, given by

$$\bar{\Gamma}_{\nu \rightarrow \mu}^{90\%} = \frac{\bar{\mu}_s^{90\%}}{V_{eff} \cdot T_{live}}, \quad (7.12)$$

where the effective volume V_{eff} is given by equation 6.5. For each annihilation chan-

nel, one can separately calculate the V_{eff} within the solar search cone, determined by the combined signal p.d.f., $f_S^{all}(x|\Psi)$, and thereby determine a $\bar{\Gamma}_{\nu \rightarrow \mu}^{90\%}$ for each channel. Additionally, the combined effective volume, $V_{eff,LKP}$, for the real KK-neutrino spectrum is given by the sum of the individual V_{eff} per channel, weighted with the respective branching ratio of each channel. For the neutrino-to-muon conversion rate per single channel, the annihilation rate in the core of the sun per second is given by,

$$\bar{\Gamma}_A^{90\%} = (c_1(ch, m_{B(1)}))^{-1} \cdot \bar{\Gamma}_{\nu \rightarrow \mu}^{90\%}, \quad (7.13)$$

where $c_1(ch, m_{B(1)})$ is a LKP annihilation channel and energy dependent constant. The minimum sensitive muon flux at a plane at the combined detector is derived with,

$$\Phi_\mu^{90\%}(E_\mu > E_{thr}) = \frac{\bar{\Gamma}_A^{90\%}}{4\pi r_\odot^2} \cdot \int_{E_{thr}}^{\infty} dE_\mu \frac{dN}{dE_\mu} = \bar{\Gamma}_A^{90\%} \cdot c_2(ch, m_{B(1)}), \quad (7.14)$$

where r_\odot is the distance Earth-Sun, which is 1AU, and the energy threshold for muon detection for neutrino telescopes is set to 1 GeV. $\frac{dN}{dE_\mu}$ is the differential number of muons produced at the detector location at a given energy from LKP annihilations in the Sun and $c_2(ch, m_{B(1)})$ is another LKP annihilation channel and energy dependent constant. The calculation chain $\bar{\Gamma}_{\nu \rightarrow \mu}^{90\%} \rightarrow \bar{\Gamma}_A^{90\%} \rightarrow \Phi_\mu^{90\%}$ is performed using the code described in [64, 65, 66], and has to be done individually for each annihilation channel and LKP mass.

Given the LKP branching ratios a true combined sensitivity of the combined detector (2007) on $\Phi_\mu^{90\%}$ can be set. The annihilation rate in the Sun, $\bar{\Gamma}_A^{90\%}$, is the starting point of the combined sensitivity calculation, from which one determines the conversion factors ($c_1(ch, m_{B(1)}), c_2(ch, m_{B(1)})$) from the annihilation rate to the different fluxes ($\bar{\Gamma}_{\nu \rightarrow \mu}^{90\%}, \Phi_\mu^{90\%}$) for all the individual KK channels. Then, the individual conversion factors are summed up into one single KK-conversion factor, weighting them by their respective branching fractions. Hence, the LKP induced muon flux sensitivity from the Sun at the detector is derived by,

$$\Phi_{\mu,LKP}^{90\%} = \frac{1}{\sum_{ch} c_1(ch, m_{B(1)})} \cdot \sum_{ch} c_2(ch, m_{B(1)}) \cdot \bar{\Gamma}_{\nu \rightarrow \mu,LKP}^{90\%}, \quad (7.15)$$

and the sensitivity on the annihilation rate in the Sun is given by,

$$\bar{\Gamma}_{A,LKP}^{90\%} = \frac{1}{\sum_{ch} c_1(ch, m_{B(1)})} \cdot \bar{\Gamma}_{\nu \rightarrow \mu,LKP}^{90\%}. \quad (7.16)$$

The results of the calculations for the different V_{eff} and sensitivities are summarised in table 7.6 and graphically illustrated for three extreme cases of V_{eff} and the muon flux $\Phi_\mu^{90\%}$ in figures 7.12 and 7.13. Assuming a total branching ratio of one, the three displayed cases correspond to the scenarios, where all neutrinos either go into the ‘best-detectable’ channel ($\nu_e, \bar{\nu}_e$), the soft (b, \bar{b}) channel or into the combined true LKP signal.

$m_{B(1)}$ in GeV/c^2	Annihil. Channel	Ψ in $[\circ]$	$\bar{\mu}_s^{90\%}$	V_{eff} in km^3	$\bar{\Gamma}_{\nu \rightarrow \mu}^{90\%}$ in $km^{-3}a^{-1}$	$\bar{\Gamma}_A^{90\%}$ in s^{-1}	$\bar{\Phi}_\mu^{90\%}$ in $km^{-2}a^{-1}$
500	1	3.5	11.09	$1.1 \cdot 10^{-3}$	$6.3 \cdot 10^4$	$8.2 \cdot 10^{23}$	$7.5 \cdot 10^3$
	2			$0.8 \cdot 10^{-3}$	$8.7 \cdot 10^4$	$4.3 \cdot 10^{23}$	$1.1 \cdot 10^4$
	3			$7.3 \cdot 10^{-3}$	$9.2 \cdot 10^3$	$1.4 \cdot 10^{22}$	$2.5 \cdot 10^3$
	4			$1.1 \cdot 10^{-2}$	$5.8 \cdot 10^3$	$3.0 \cdot 10^{21}$	$2.2 \cdot 10^3$
	16			$5.7 \cdot 10^{-2}$	$1.2 \cdot 10^3$	$1.7 \cdot 10^{21}$	$1.1 \cdot 10^3$
	17			$5.5 \cdot 10^{-2}$	$1.2 \cdot 10^3$	$1.0 \cdot 10^{21}$	$1.0 \cdot 10^3$
	18			$3.6 \cdot 10^{-2}$	$1.8 \cdot 10^3$	$9.8 \cdot 10^{20}$	$1.3 \cdot 10^3$
	LKP			$1.1 \cdot 10^{-2}$	$6.2 \cdot 10^3$	$5.6 \cdot 10^{21}$	$2.4 \cdot 10^3$
750	1	2.75	8.86	$0.9 \cdot 10^{-3}$	$5.9 \cdot 10^4$	$6.5 \cdot 10^{23}$	$8.5 \cdot 10^3$
	2			$1.8 \cdot 10^{-3}$	$3.0 \cdot 10^4$	$1.3 \cdot 10^{23}$	$4.5 \cdot 10^3$
	3			$8.4 \cdot 10^{-3}$	$6.3 \cdot 10^3$	$8.6 \cdot 10^{21}$	$2.1 \cdot 10^3$
	4			$1.6 \cdot 10^{-2}$	$3.3 \cdot 10^3$	$1.6 \cdot 10^{21}$	$1.6 \cdot 10^3$
	16			$7.7 \cdot 10^{-2}$	$6.9 \cdot 10^2$	$1.6 \cdot 10^{21}$	$9.0 \cdot 10^2$
	17			$6.9 \cdot 10^{-2}$	$7.7 \cdot 10^2$	$1.6 \cdot 10^{21}$	$8.9 \cdot 10^2$
	18			$3.1 \cdot 10^{-2}$	$1.7 \cdot 10^3$	$1.3 \cdot 10^{21}$	$1.2 \cdot 10^3$
	LKP			$1.4 \cdot 10^{-2}$	$3.9 \cdot 10^3$	$3.4 \cdot 10^{21}$	$1.8 \cdot 10^3$
1000	1	2.5	8.12	$1.1 \cdot 10^{-3}$	$4.4 \cdot 10^4$	$4.5 \cdot 10^{23}$	$7.2 \cdot 10^3$
	2			$2.6 \cdot 10^{-3}$	$1.9 \cdot 10^4$	$7.4 \cdot 10^{22}$	$3.2 \cdot 10^3$
	3			$1.0 \cdot 10^{-2}$	$4.8 \cdot 10^3$	$6.4 \cdot 10^{21}$	$1.8 \cdot 10^3$
	4			$1.7 \cdot 10^{-2}$	$2.9 \cdot 10^3$	$1.5 \cdot 10^{21}$	$1.5 \cdot 10^3$
	16			$9.4 \cdot 10^{-2}$	$5.2 \cdot 10^2$	$5.4 \cdot 10^{21}$	$7.0 \cdot 10^2$
	17			$9.0 \cdot 10^{-2}$	$5.4 \cdot 10^2$	$1.7 \cdot 10^{21}$	$7.9 \cdot 10^2$
	18			$2.7 \cdot 10^{-2}$	$1.8 \cdot 10^3$	$1.6 \cdot 10^{21}$	$1.3 \cdot 10^3$
	LKP			$1.5 \cdot 10^{-2}$	$3.2 \cdot 10^3$	$2.8 \cdot 10^{21}$	$1.6 \cdot 10^3$

Table 7.6: Expectation values for sensitivities on the effective volume, V_{eff} , the $\nu \rightarrow \mu$ conversion rate, $\bar{\Gamma}_{\nu \rightarrow \mu}^{90\%}$, the annihilation rate in the Sun per second, $\bar{\Gamma}_A^{90\%}$, and the muon flux, $\bar{\Phi}_\mu^{90\%}$, for all individual annihilation channels and for the combined true LKP signal. All results for the individual channel are scaled to a total branching ratio of 1.

7.4 Systematics

The systematic errors in the calculation of the effective volume V_{eff} arise from various sources within the simulation chain. The dominant contributions to the total systematic uncertainty are the uncertainties in the sensitivity of the OMs and DOMs and the optical properties of the Antarctic ice, such as the different ice properties of the refrozen water around the strings, cable screening, variations in the absolute PMT efficiency and OM/DOM aging. The pointing accuracy of the reconstructed muon tracks is estimated by coincident down-going events between the SPASE air shower array and the in-ice detector array and is estimated to be

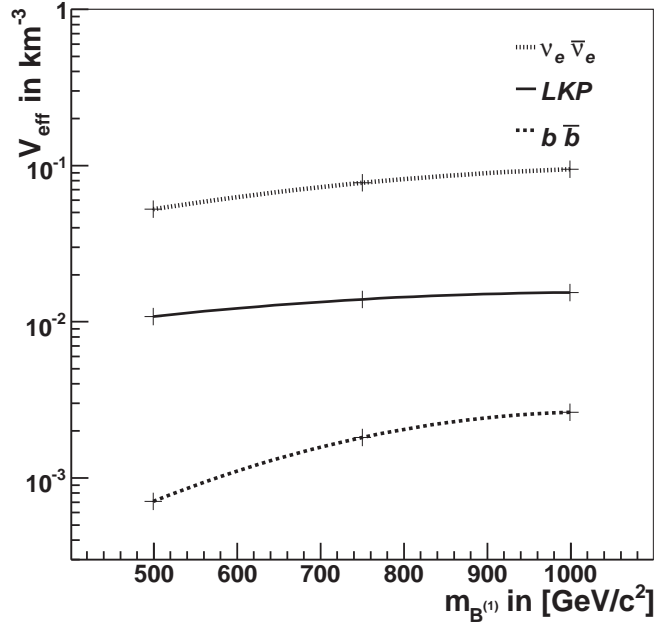


Figure 7.12: Results for the final V_{eff} . All graphs are plotted assuming a total branching ratio of 1 for the annihilation channels resulting in detectable neutrinos.

less than 1° [67]. The systematic errors in the ν -nucleon cross-section and the μ -propagation in the ice are estimated in [64, 33]. All other effects, summarised in table 7.7, are obtained by comparison with recently published and unblinded indirect dark matter searches using AMANDA and IceCube (22 string only) [68, 69, 70]. The total systematic error is given by the squared sum over all individual uncertainties. The specific systematics for this work will be estimated in intensive MC studies after all experimental data is processed and the ‘unblinding’ proposal has been approved. Since the muon flux is proportional to $1/V_{eff}$, the final results for the predicted sensitivities are scaled by a factor $1/(1.0 \pm \sum(sys))$ to obtain the correct error bars. The estimated total uncertainties of 23% on V_{eff} amount to a total systematic uncertainty on the sensitive flux of $\Phi_{-19\%}^{+30\%}$ (displayed in figure 7.13)

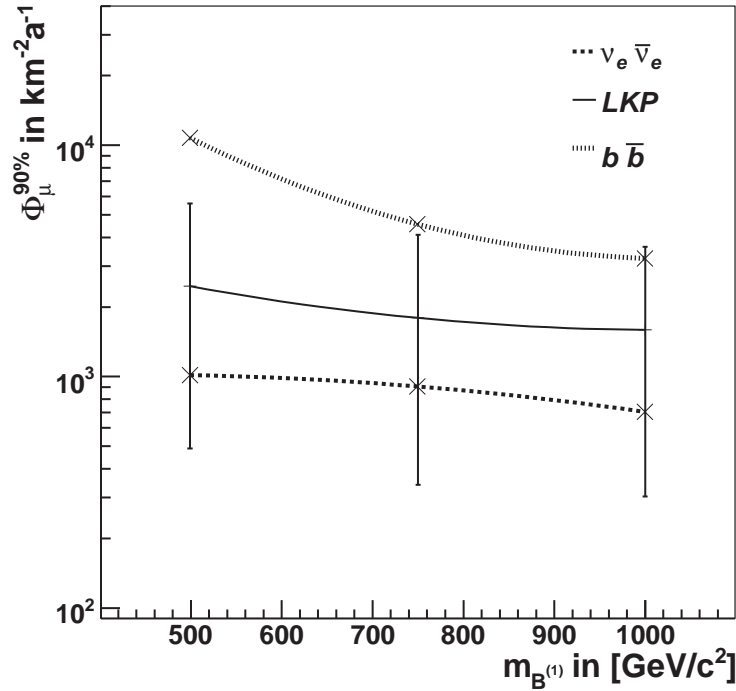


Figure 7.13: Results for the minimal sensitive muon flux $\overline{\Phi}_\mu^{90\%}$ of the combined detector together with the cuts applied in this work. All graphs are plotted assuming a total branching ratio of 1 for the annihilation channels resulting in detectable neutrinos. The solid line, reflecting the true LKP spectrum is drawn including the systematic errors (indicated by solid vertical lines), which are estimated in section 7.4.

Source	Magnitude
ν -oscillations	3%
ν -nucleon cross-section	3%
μ -propagation in ice	< 1%
Photon yield and propagation in ice	20%
OM sensitivity, PMT response	2%
Signal MC statistics	3%
Calibration (time, position, reconstruction)	10%
Total systematics $\sum(sys)$	23%

Table 7.7: Systematic uncertainties estimated from [64, 33, 68, 69, 70]

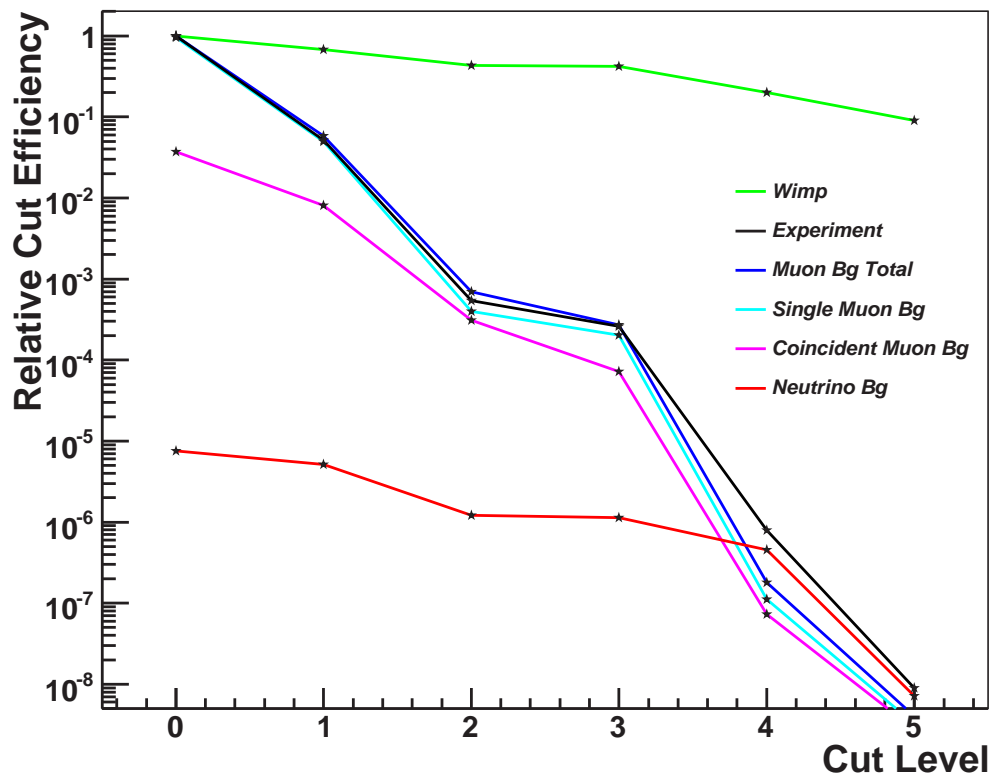


Figure 7.14: Relative cut efficiency at different filter levels. The efficiency is set to 1 at trigger level for the experimental data, the total μ_{atm} background, and the LKP signal (here channel 18 for $m_{B^{(1)}} = 1000 \text{ GeV}/c^2$ is taken as reference). The ν_{atm} , single μ_{atm} , and coincident μ_{atm} samples are rescaled to their true trigger rate relative to the total efficiency of 1.

Chapter 8

Results and Discussion

The results for the predicted sensitivity to a muon flux resulting from LKP induced annihilations in the Sun for the combined IceCube and AMANDA detector 2007 with a total livetime of 60 days are presented in figure 7.13. As shown in equation 7.16, the derived ν -to- μ conversion rate, $\bar{\Gamma}_{\nu \rightarrow \mu, LKP}^{90\%}$, reflecting the composite signal of the seven simulated channels, can be used to calculate a sensitivity for the total annihilation rate in the Sun per second, $\bar{\Gamma}_{A, LKP}^{90\%}$. The derived results for the LKP annihilation rate, listed in table 7.6, are calculated for a total branching ratio of one, corresponding to the seven simulated channels only. This result assumes all $B^{(1)}B^{(1)}$ annihilating into one of the seven channels investigated. This does not reflected reality, as the simulated channels only correspond to a total branching ratio of 0.463. Therefore, $\bar{\Gamma}_{A, LKP}^{90\%}$ is rescaled by a factor of $1/0.463$ to attain the predicted sensitivity on the actual LKP annihilation rate in the Sun.

In chapter 3 it is shown that the equilibrium condition between $\Gamma_{A, LKP}$ and the capture rate C^\odot , required in a solar search, is met by LKPs within the probed mass range. Furthermore, the capture rate of LKPs in the Sun is entirely dominated by the spin-dependent component of the $B^{(1)}$ -on-proton elastic scattering. Consequently, presuming an equilibrium of $\Gamma_{A, LKP} = C^\odot$, the sensitivity for the spin-dependent elastic scattering cross section¹ of $B^{(1)}$ can be calculated as,

$$\sigma_{H, SD} \simeq \frac{1}{3.35} \cdot 10^{-24} \left(\frac{m_{B^{(1)}}}{1000 \text{ GeV}/c^2} \right)^2 \cdot \bar{\Gamma}_{A, LKP}^{90\%} \cdot \frac{1}{0.463} \text{ pb} . \quad (8.1)$$

The estimated sensitivity for the spin-dependent cross section (region of interest is blue-shaded) and the spin-independent cross section (region of interest is yellow-shaded) for LKPs is displayed in figure 8.1, along with the most recently published limits from direct search experiments, which are discussed below. The theoretical cross section predictions (blue and yellow shaded regions) for LKPs are taken from [71] and are plotted for different predictions for the mass of the 1st KK-excitation of the quark, given by $0.01 \leq r = (m_{q^{(1)}} - m_{B^{(1)}})/m_{B^{(1)}} \leq 0.5$. Disfavoured mass

¹The local density of DM in our galaxy is taken to match the mean density $\bar{\rho}_{DM} = 0.3 \text{ GeV}/c^2 \text{ cm}^3$, and the rms velocity is set to $\bar{v} = 270 \text{ km/s}$.

regions for the LKP are indicated in grey. Figure 8.1 shows the calculated IceCube 22-string + AMANDA-II limit for a wider LKP mass spectrum, ranging from $250 \text{ GeV}/c^2 \leq m_{B(1)} \leq 3000 \text{ GeV}/c^2$. In order to present this sensitivity, two additional LKP masses are simulated, reconstructed and filtered, although the masses outside the normal signal region are strongly disfavoured (see Appendix A for details). The extended mass range is investigated in preparation for the unblinding proposal, in order to demonstrate the sensitivity of the combined detector with respect to a wider LKP mass range. The essential steps of the analysis remain the same and are specifically optimised for the most probable mass range within the two grey-shaded areas.

8.1 Comparison to Direct Search Experiments

Unlike indirect search experiments, which measure products of WIMP annihilations or WIMP reactions, direct detection experiments look for the interaction of WIMPs with ordinary matter by measuring, for example, the recoil energy of nuclei, as WIMPs scatter off them. The interaction processes with the target nuclei can be divided into elastic or inelastic scattering, and spin-dependent or spin-independent scattering processes. In order to compare the results obtained in this study with results from direct search experiments, the quantity of interest is the sensitivity of direct search experiments to the spin-dependent elastic cross section. One has to note that the direct search approach and the indirect experiment (the latter being the focus of this work) measure different quantities. The indirect method measures WIMPs accumulating in the Sun during the entire existence of the solar system, and is therefore not influenced by DM density fluctuations within our galaxy, as it is accomplished in a possibly lumpy DM density distribution scenario with the same value $\bar{\rho}_{DM}$ for the mean density. Direct search experiments measure the current local WIMP population. The cross section for spin-dependent scattering is proportional to the total angular momentum ($J(J+1)$) of the utilised target nuclei, whereas the spin-independent cross section depends quadratically on the mass of the nuclei, A . In direct search experiments, the target nuclei are generally chosen to be heavy elements, to enhance the total scattering cross section. Nevertheless, the spin-independent component dominates over the spin-dependent component of the total cross section in all current experimental setups [3].

The existing limits within the parameter space for neutralino search, χ , are all dominated by direct search experiments. However, the detection prospects for the direct experiments via the spin-independent scattering cross section of LKPs, described through the exchange of KK-quarks at quark level [17], are expected to be not particularly successful within the next few years [73]. A much more promising prognosis for probing the parameter space of the spin-dependent scattering cross section of KK-DM is given for neutrino telescopes, and is reflected by the results presented here, which are illustrated in figure 8.1. Although, the livetime of the detector was limited to 60 days in 2007, the calculated sensitivity of the combined

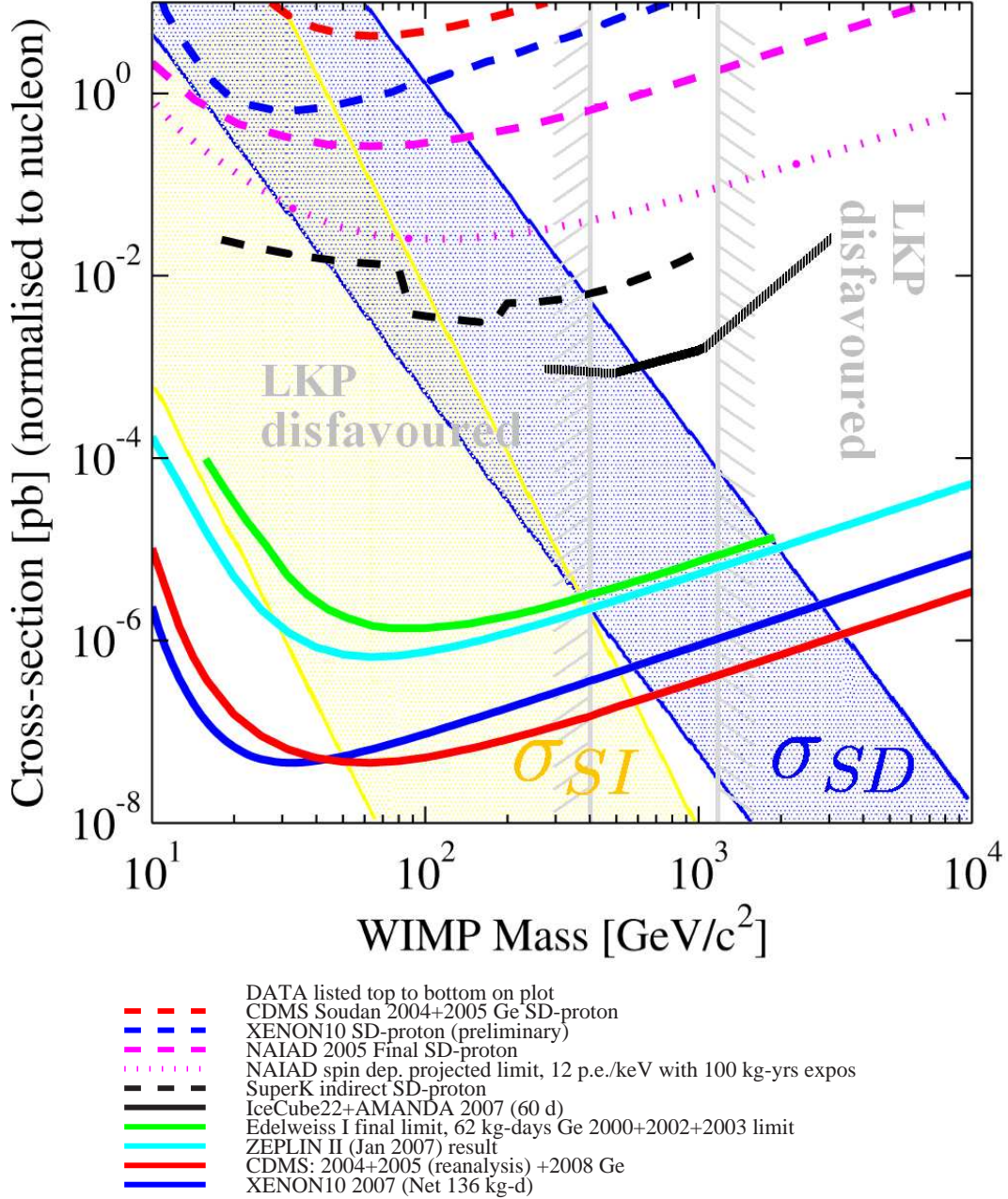


Figure 8.1: Predicted spin-dependent $B^{(1)}$ -on-proton elastic scattering cross section, indicated by the blue lines and the blue-shaded area, as well as predictions for the spin-independent component, indicated by the yellow lines and the yellow-shaded area. The indicated cross section regions mark predictions for different values of the cross section according to different predictions for the mass of the 1st KK-excitation of the quark, given by $0.01 \leq r = (m_{q^{(1)}} - m_{B^{(1)}})/m_{B^{(1)}} \leq 0.5$. The current ‘best’ limits, set by direct search experiments, on the spin-independent component (yellow-shaded only) are illustrated by the coloured solid lines. The limits on the spin-dependent component (blue-shaded only) are displayed by the dashed-coloured lines, and the sensitivity of the combined detector IC22 + TWR (calculated in this study) is shown by the black solid line, which is extended into the disfavoured regions (black fine-dashed line). The region below $m_{B^{(1)}} = 400 \text{ GeV}/c^2$ and above $1200 \text{ GeV}/c^2$ is disfavoured by CMB and SN1a observations [2, 11]. Limits are plotted with [72] and cross section predictions are taken from [71].

detector 2007, is together with the most recent CDMS results (spin-independent), the only existing experiment, actually probing the favoured parameter space above a LKP mass of $400 \text{ GeV}/c^2$. The limits set by the EDELWEISS experiment [74] and the ZEPLIN-II detector do not probe the equivalent parameter space within the spin-independent cross section region, indicated by the yellow-shaded area in figure 8.1. The steeper slope of the spin-independent cross section parameter space underlines this prognosis, because more significant experimental improvements have to be made to lower the limit an order in magnitude, than for the spin-dependent component, having a more gentle slope. Hence, neutrino telescopes are promising detectors for probing most of the favoured parameter space of KK-DM in the nearby future. Additionally, the sensitivity for the combined detector is going to improve significantly during the next years. Data samples with longer livetimes will be available and the effective detection volume will increase, as IceCube is still in the construction phase.

8.2 Comparison to Neutralino Search

A good measure of the quality of the performed analysis is a comparison to the indirect solar search limits on χ dark matter, recently published from AMANDA-II and IceCube 22 string results within the matching mass range of $500 \text{ GeV}/c^2 \leq m_\chi \leq 1000 \text{ GeV}/c^2$ [68, 70]. The comparison is possible, as the performed analysis treats all investigated annihilation channels independently throughout simulation, reconstruction and filtering. Only the actual cut values are optimised for the expected composition of the neutrino spectra, resulting from the different annihilation channels. The χ is a Majorana particle postulated by the MSSM and the most viable WIMP candidate within this framework [3]. Unlike the LKP, the exact composition of the χ is not unambiguously determined by the underlying theory and depends on many open parameters. Consequently, the branching ratios are not known and only two extreme cases, the softest and hardest resulting neutrino spectrum, are simulated in order to set a limit on the best and worst case scenario. The true limit is anticipated to be found in between these two limits. The $b\bar{b}$ channel is one of the simulated LKP channels and also the corresponding soft channel for the χ search. Therefore, the current analysis can also calculate a sensitivity for the soft χ channel. The expected sensitivity for the combined detector 2007 with $T_{live} = 60 \text{ d}$ is shown in figure 8.2.

The calculated sensitivity is of course limited to the very specific LKP mass range and additionally constrained by T_{live} , when compared to the IceCube-22 (2007) or AMANDA-II (2003) results. The statistics within the simulated signal of the $b\bar{b}$ channel of this analysis are also too low, to be able to set a valid sensitivity. Nevertheless, the here derived sensitivity is very close to the IceCube-22 sensitivity, which is obtained from a much bigger experimental dataset with a livetime of 110 days and is, in addition, specialised on this one soft channel. This LKP analysis is performed on a mixed signal, which is dominated by hard channels, like the three

$\nu_l \bar{\nu}_l$ and the $\tau^+ \tau^-$ channels. Overall, this comparison shows that the χ sensitivity derived in this study can compete with an analysis specialised in χ search, despite the cut values being optimized for the LKP channel composition and not for the neutrino spectrum from the $b\bar{b}$ annihilation channel.

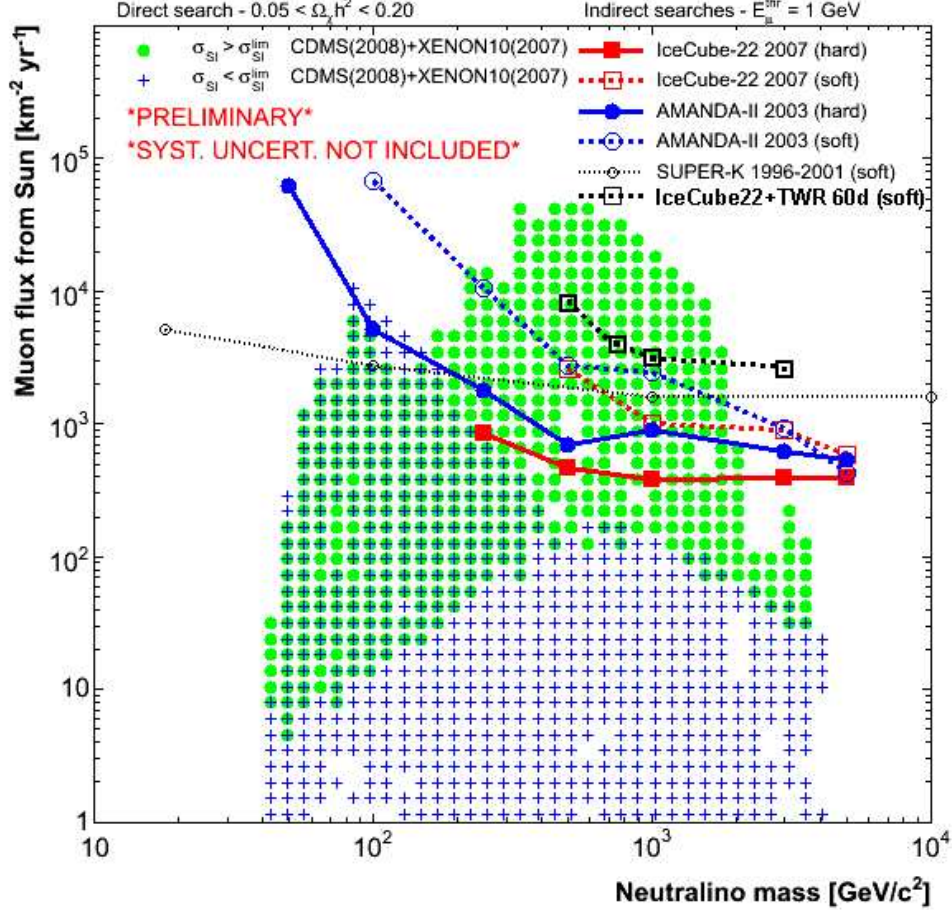


Figure 8.2: Solar χ signal muon flux 90% upper limits, presented in recent analysis [68, 70], and from Super-Kamiokande [75]. The sensitivity for the soft channel from this thesis is marked by the black-dotted line (without systematic errors). Each point in the figure represents a particular SUSY model, where the points marked in green are disfavoured by the direct search experiment Xenon-10 and CDMS [76].

8.3 Further Optimisations for KK-DM Indirect Search

The cut optimisation for the LKP analysis is more complex than it is for a single channel χ analysis. The knowledge about the composition of the LKP signal from the individual annihilation channels is an advantage, regarding the limit predictability of the results, but makes it more difficult to find the most efficient cut values,

concerning the mixture of hard and soft muon spectra. Throughout this study, a lot of effort went into finding the best cut values for the known LKP channel composition. The analysis of initially most promising channels, $\nu_l \bar{\nu}_l$ and $\tau^+ \tau^-$, with respect to detection probability in the combined detector array, is extended to three additional channels ($b\bar{b}$, $c\bar{c}$, $t\bar{t}$) to improve the results. The signal p.d.f., $f_S^{all}(x|\Psi)$, in the level 5 cut, as well as in the early filter levels, is optimised for a detection of the combined signal of all channels. The multivariant cut level is trained and tested on the hardest possible LKP annihilation channel, the $\nu_\mu \bar{\nu}_\mu$ channel with a LKP mass of $750 \text{ GeV}/c^2$. Initially, it was assumed that training and testing the TMVA cut on the hardest channel only enhances the distinctive character of the signal distribution with respect to the background. Results obtained in level 5 studies though, indicate that the optimisation of cuts on the real composition of the LKP signal is more efficient than cuts optimised on the ‘best’ signal. Therefore it is concluded that a multivariant cut on the combined signal further improves the calculated sensitivity of the combined detector. Due to the fact that all simulated signal samples, used for training and testing the TMVA cut, have to be discarded afterwards, in order to avoid a bias in the final results, the further refinement of the TMVA cut is beyond the scope of this thesis.

A signal generation over a wider LKP mass range is also another possible extension, which is accomplished for two additional LKP masses of $250 \text{ GeV}/c^2$ and $3000 \text{ GeV}/c^2$. Although the parameter space for the theoretically predicted LKP masses is more strongly bound than the χ mass range, and therefore limited to the masses probed in this thesis, nature doesn’t always behave as predicted by theorists. Therefore, results from an extended analysis, which covers a wider mass range, is more powerful in excluding parameter regions (see appendix A for details).

Deep Core

The derived sensitivity from this thesis indicates very strongly that in the following years, promising limits can be set on the spin-dependent cross section of LKPs with protons and large areas of the currently favoured parameter space for LKPs will be excluded or discoveries will be made. This will be made possible, by longer experimental datasets and the growing effective detection volume of IceCube as string deployment continues until the Austral summer 2010. Additionally, a low energy extension of IceCube, called Deep Core, has been funded and will be added to the IceCube array under construction. Deep Core will consist of six additional strings near the centre of IceCube (see figure 8.3) with a DOM spacing of only 10 metres instead of 17 metres. In these strings, the top modules will be situated 600 metres lower than the upper-most DOM on the IceCube strings, and are therefore below all identified dust layers, in the clearest ice of the instrumented detector volume. Together with the surrounding IceCube strings, the extra strings (240 additional DOMs) form a very densely spaced fiducial volume, well shielded by all outer IceCube strings and upper DOM layers. This low energy upgrade makes the total detector array more sensitive to shorter muon tracks, which emit less light

along their path. In preliminary studies [37, 77], it was shown that the triggered atmospheric μ background is not increased by Deep Core (due to its location in the deep centre of IceCube), while the effective area for low energetic point sources, like a LKP induced neutrino signal from the core of the Sun, is increased by up to two orders of magnitude for low energy neutrinos.

The importance of an detector extension like Deep Core is affirmed by the results obtained in this study. The sensitivities, presented here for the combined detector 2007 can compete with the most recent single detector results, e.g., the IceCube 22 analysis, despite a considerable shorter data set, corresponding to only 0.17 years. The main advantage over the single detector setup is the enhanced atmospheric muon background reduction, which allows to select a purer neutrino candidate sample in the final filter level and hence is reflected in a significantly improved sensitivity.

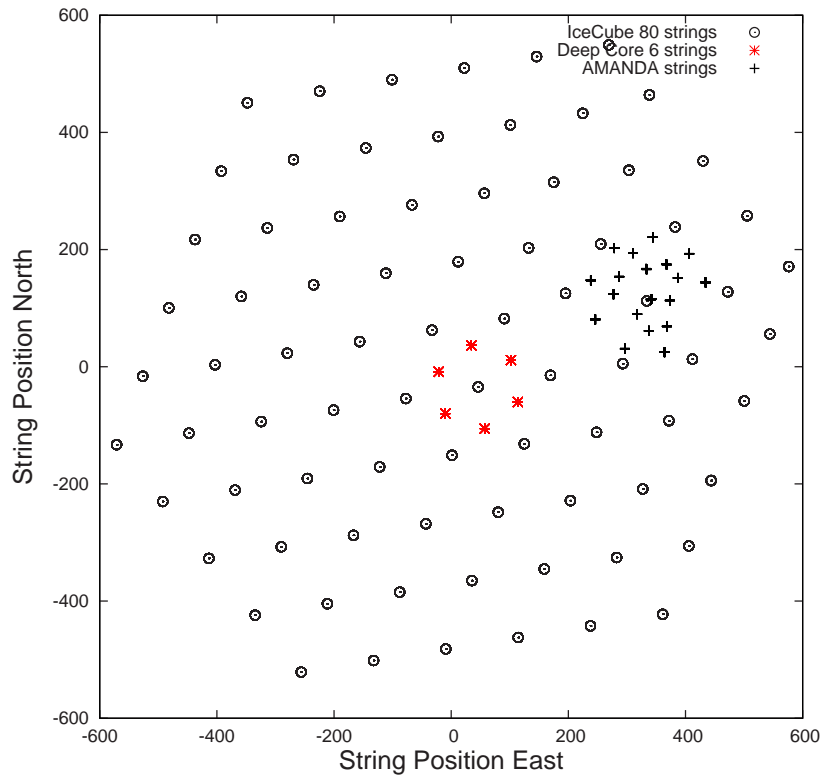


Figure 8.3: *Position of Deep Core within the IceCube array. The Deep Core strings are indicated by the red stars. Amanda strings are marked with black crosses and IceCube strings by black circles.*

Summary and Outlook

This thesis demonstrates the feasibility of detecting muons from LKP annihilations in the core of the Sun with the combined detector array 2007. These results set a benchmark for future studies in two ways. The derived sensitivity is the first complete analysis, using AMANDA-II integrated within the IceCube detector array. Moreover, this work presents the first sensitivities for the composition of all detectable LKP annihilation channels for the IceCube-AMANDA-II neutrino telescope. The processing of all available data will be done shortly and an unblinding proposal to the collaboration is in progress. The resulting events within the final sample of the available experimental dataset agree with the expected number of atmospheric neutrino events and atmospheric muon events. The sensitivity, presented here, on the LKP induced muon flux at the detector at the 90% upper confidence level is expected to be further reduced in the actual limit, which will be placed after the data unblinding.

Furthermore, a competitive limit, compared to existing direct and indirect search experiments, at the 90% upper confidence level on the spin-dependent cross section of $B^{(1)}$ on protons will be set. This limit, although placed with a 2007 data sample of 0.17 years of detector livetime, already probes inside the favoured parameter space for LKPs.

In future years, the combined detector array, including the Deep Core extension, will be a viable instrument to exclude most regions in the predicted parameter space, or even claim a possible discovery, if theories of universal extra dimensions are correct.

Acknowledgements

First of all I want to thank the University of Canterbury for offering me a place as a visiting scholar, which allowed me to carry out my research with the local IceCube group. Especially, I would like to thank Dr. Jennifer Adams for offering me the opportunity to complete my Diploma thesis in her group and for all her different arrangements throughout this year to support me in the best possible way.

My special thanks to Dr. Surjdeo Seunarine for being a constant source of help and inspiration in theoretical problems and questions as well as his support in computing.

Additionally, I want to thank the University of Stockholm and in person, Prof. Dr. Per Olof Hulth, for inviting me to Stockholm to discuss and solve ongoing analysis problems halfway through this work. There, I had the fortunate possibility to work with numerous great people, like Gustav Wikström and Thomas Burgess who helped me finishing this thesis.

I also want to thank Kahae Hahn for introducing me to this topic and the appalling beauty of a particle physics data analysis. I also very much appreciated her hospitality during my stay in Sweden.

Furthermore, I want to express my thanks to MSc Nikolai Krützmann, the coffee machine operator and most fussy and picky corrector of my thesis and his joyful participation in my trips.

Thanks also to all my office mates, in particular Sam Whitehead for reading my thesis and Joe for only deleting all my local data!

I would like to use the opportunity to thank my girlfriend Aroha for supporting and enduring me throughout the last year, especially when my work has been very difficult and progress was not in sight. I know it is not easy to be in a relationship with a physicist, who doesn't know official working hours.

Finally, I would like to thank my parents for supporting me during the last years in New Zealand in any thinkable way and all the trust and faith they have in me. This made it possible for me to continue my studies in New Zealand and to stay in the first place.

Last but not least, I want to thank my TUM supervisor Prof. Dr. Lothar Oberauer for shaping me to such a self-reliant and independent physicist and his strong advice to undertake further research and a PhD in an overseas country.

List of Figures

2.1	Rotation Curve of galaxy NGC 6503	7
2.2	Allowed Regions for Ω_m with respect to h and Ω_b	8
2.3	Loop violating Lorentz Invariance in 5-dimensions	11
2.4	Allowed regions for $m_{B^{(1)}}$ with respect to $\Omega_{B^{(1)}}h^2$	13
3.1	Feynman diagram for the $B^{(1)}B^{(1)}$ annihilation	17
3.2	$\nu_\mu\bar{\nu}_\mu$ spectra resulting from $B^{(1)}B^{(1)}$ annihilations	18
4.1	Feynman diagram for NC and CC interaction of ν with nucleon	20
4.2	Helicity suppression in the $\bar{\nu}_\mu CC$ interaction	21
4.3	Muon energy losses in ice	24
5.1	3-Dim overview of the IceCube 2010 detector	27
5.2	Top view of the combined detector	28
5.3	Depths of deployed strings	28
5.4	Illustration of LC span 2 setting	29
5.5	Signal and background muon sources in the combined detector	31
5.6	Neutrino fluxes from different sources	34
6.1	Flow chart of simulation chain	36
6.2	Scattering coefficient profile at South Pole	37
6.3	Zenith angle distribution for LKP ν and created μ	40
6.4	Muon energy spectra for all WIMP signals	41
6.5	Simulated μ_{atm} zenith distribution at South Pole	43
6.6	Simulated ν_{atm} spectrum triggering the detector	44
6.7	Reconstruction variables and PMT jitter influences	45
6.8	Number of triggered signal events per ch and per $m_{B^{(1)}}$	51
7.1	Multiplicities MC vs. background	56
7.2	Reconstruction parameters MC vs. background	57
7.3	Geometry parameters MC vs. background	58
7.4	Veto and fiducial strings	60
7.5	Vertex positions of events passing $L1$ filter	61
7.6	$L2$ filter parameters	62
7.7	Cut Optimization	64

7.8	$L3$ filter parameters	65
7.9	TMVA cut parameters	66
7.10	Signal and Background p.d.f. at level $L5$	68
7.11	Solar search optimisation	70
7.12	Results for V_{eff}	73
7.13	Results for $\overline{\Phi}_{\mu}^{90\%}$	74
7.14	Relative cut efficiency at different filter level	75
8.1	Sensitivity for the spin-dependent cross section	79
8.2	Solar χ signal muon flux 90% upper limits	81
8.3	Deep Core position within the IceCube array	83
A.1	Results for V_{eff} for additional LKP signals	95
A.2	Results for $\overline{\Phi}_{\mu}^{90\%}$ for additional LKP signals	96

List of Tables

3.1	Table for the different $B^{(1)}B^{(1)}$ annihilation channels	17
6.1	Table of WimpSim input parameters	39
6.2	Simulated background datasets	47
6.3	LKP signals	48
6.4	Experimental datasets	50
7.1	Table of parameters in analysis	55
7.2	Filter settings at $L0 + L1$ level	59
7.3	Trigger rates at different filter levels	60
7.4	Cut efficiencies	69
7.5	Best fit values for solar search cone Ψ	69
7.6	Expectation values for different sensitivities	72
7.7	Sytematic uncertainties	74
A.1	Additional LKP signals	94
A.2	Cut efficiencies of additional LKP signals	94
A.3	Expectation values sensitivities of additional LKP signals	95
B.1	Good Run List 2007 for the combined detector	98

Appendix A

Additional Masses

Theories of universal extra dimensions favour together with the most recent observations a LKP mass around $800 \text{ GeV}/c^2$. The main analysis is consequently constructed and optimised for the most likely mass range from $500 \text{ GeV}/c^2$ to $1000 \text{ GeV}/c^2$. In addition, two further LKP signals at $250 \text{ GeV}/c^2$ and $3000 \text{ GeV}/c^2$ are investigated, to indicate what sensitivities can be placed by the combined detector 2007 on these particle masses. Therefore, the combined detector will set more restrictive limits on the LKP induced muon flux and the spin-dependent cross section component of the LKP-on-proton scattering, although the additional regions are strongly disfavoured by theory [21]. All details regarding the additional simulated LKP signals are listed in tables A.1, A.2, and A.3. The final results for the effective volume and the calculated sensitivity on the muon flux for the complete mass range are shown in figures A.1 and A.2. At $250 \text{ GeV}/c^2$, the two softest channels ($ch1(c\bar{c}), ch2(b\bar{b})$) do not result in a countable contribution towards the effective volume, because the different cut levels, optimised for the main region of interest and therefore designed for harder muon spectra, filter out all triggered events. For the high energy LKP signal with a mass of $3000 \text{ GeV}/c^2$, the nearly monochromatic direct neutrino channels ($ch16(\nu_e\bar{\nu}_e), ch17(\nu_\mu\bar{\nu}_\mu)$) result with one or respectively two triggered events in nearly no detection and are consequently discarded. This can be explained by the fact that $\nu_e(\bar{\nu}_e)$ and $\nu_\mu(\bar{\nu}_\mu)$ interactions in the Sun result in complete absorption of the initial neutrino, unlike $\nu_\tau(\bar{\nu}_\tau)$, which are regenerated at lower energies. The probability of neutrinos escaping the Sun without interacting is given by [13]

$$P = e^{-E_\nu/E_k} , \quad (\text{A.1})$$

where E_k is for example (130 GeV, 160 GeV) for $(\nu_\mu, \bar{\nu}_\mu)$. Consequently, at very high energies, the neutrino fluxes emitted from the core of the Sun are exponentially suppressed and do not contribute to the composed LKP signal.

$m_{B^{(1)}}$ in GeV/c^2	Annihilation Channel	N_{ann} in Sun	N_{trig}	$V_{eff,trig}$ in km^3
250	1	$2 \cdot 10^6$	73	—*
	2	$2 \cdot 10^6$	207	—*
	3	$2 \cdot 10^6$	$1.83 \cdot 10^3$	$2.5 \cdot 10^{-2}$
	4	$2 \cdot 10^6$	$7.41 \cdot 10^3$	$4.6 \cdot 10^{-2}$
	16	$2 \cdot 10^6$	$16.2 \cdot 10^3$	$1.7 \cdot 10^{-1}$
	17	$2 \cdot 10^6$	$14.5 \cdot 10^3$	$1.5 \cdot 10^{-1}$
	18	$2 \cdot 10^6$	$13.8 \cdot 10^3$	$1.4 \cdot 10^{-1}$
3000	1	$2 \cdot 10^6$	484	$5.1 \cdot 10^{-3}$
	2	$2 \cdot 10^6$	$1.27 \cdot 10^3$	$4.5 \cdot 10^{-2}$
	3	$2 \cdot 10^6$	$4.14 \cdot 10^3$	$1.2 \cdot 10^{-1}$
	4	$2 \cdot 10^6$	$10.0 \cdot 10^3$	$1.8 \cdot 10^{-1}$
	16	$2 \cdot 10^6$	1	—**
	17	$2 \cdot 10^6$	2	—**
	18	$2 \cdot 10^6$	$5.21 \cdot 10^3$	$1.1 \cdot 10^{-1}$

Table A.1: Number of triggered events, N_{trig} , effective volume at trigger level, $V_{eff,trig}$ and number of simulated annihilations, N_{ann} , given for each additional simulated LKP mass $m_{B^{(1)}}$ and annihilation channel. *- none of the triggered events survived the cuts, which are designed for hard signal distributions. **- the number of triggered events is too low, therefore the channels are discarded.

Dataset	ch	L0 + L1	L2	L3	L4	L5
250 GeV/c^2	1	—	—	—	—	—
	2	—	—	—	—	—
	3	0.61	0.29	0.29	0.07	0.04
	4	0.62	0.32	0.31	0.10	0.06
	16	0.67	0.43	0.42	0.19	0.13
	17	0.65	0.41	0.40	0.18	0.12
	18	0.66	0.41	0.40	0.18	0.12
3000 GeV/c^2	1	0.66	0.35	0.35	0.12	0.06
	2	0.64	0.33	0.32	0.11	0.06
	3	0.66	0.39	0.38	0.16	0.11
	4	0.66	0.41	0.40	0.17	0.11
	16	—	—	—	—	—
	17	—	—	—	—	—
	18	0.65	0.38	0.37	0.15	0.09

Table A.2: Cut efficiencies. For two additional LKP masses used in this analysis, the individual cut efficiencies of each cut level are summarised and normalised to 1 at trigger level.

$m_{B^{(1)}}$ in GeV/c^2	Annihil. Channel	Ψ in $[\circ]$	$\bar{\mu}_s^{90\%}$	V_{eff} in km^3	$\bar{\Gamma}_{\nu \rightarrow \mu}^{90\%}$ in $km^{-3}a^{-1}$	$\bar{\Gamma}_A^{90\%}$ in s^{-1}	$\bar{\Phi}_\mu^{90\%}$ in $km^{-2}a^{-1}$
250	1	3.75	11.8	—	—	—	—
	2			—	—	—	—
	3			$1.3 \cdot 10^{-3}$	$5.8 \cdot 10^4$	$1.2 \cdot 10^{23}$	$9.6 \cdot 10^3$
	4			$3.7 \cdot 10^{-3}$	$2.0 \cdot 10^4$	$1.4 \cdot 10^{22}$	$4.7 \cdot 10^3$
	16			$2.2 \cdot 10^{-2}$	$3.3 \cdot 10^3$	$1.9 \cdot 10^{21}$	$1.7 \cdot 10^3$
	17			$1.9 \cdot 10^{-2}$	$3.9 \cdot 10^3$	$2.3 \cdot 10^{21}$	$1.9 \cdot 10^3$
	18			$1.8 \cdot 10^{-2}$	$4.1 \cdot 10^3$	$2.2 \cdot 10^{20}$	$1.9 \cdot 10^3$
	LKP			$3.5 \cdot 10^{-3}$	$2.2 \cdot 10^4$	$2.4 \cdot 10^{22}$	$5.7 \cdot 10^3$
3000	1	4.0	12.5	$0.6 \cdot 10^{-3}$	$1.2 \cdot 10^5$	$9.0 \cdot 10^{23}$	$2.5 \cdot 10^4$
	2			$5.3 \cdot 10^{-3}$	$1.3 \cdot 10^4$	$4.2 \cdot 10^{22}$	$3.0 \cdot 10^3$
	3			$1.8 \cdot 10^{-2}$	$3.9 \cdot 10^3$	$5.1 \cdot 10^{21}$	$1.6 \cdot 10^3$
	4			$2.8 \cdot 10^{-2}$	$2.5 \cdot 10^3$	$1.7 \cdot 10^{21}$	$1.5 \cdot 10^3$
	16			—	—	—	—
	17			—	—	—	—
	18			$1.6 \cdot 10^{-2}$	$4.4 \cdot 10^3$	$6.0 \cdot 10^{21}$	$1.9 \cdot 10^3$
	LKP			$1.8 \cdot 10^{-2}$	$4.0 \cdot 10^3$	$4.6 \cdot 10^{21}$	$2.2 \cdot 10^3$

Table A.3: Expectation values for sensitivities on the effective volume, V_{eff} , the $\nu \rightarrow \mu$ conversion rate, $\bar{\Gamma}_{\nu \rightarrow \mu}^{90\%}$, the annihilation rate in the Sun per second, $\bar{\Gamma}_A^{90\%}$, and the muon flux, $\bar{\Phi}_\mu^{90\%}$, for all different annihilation channels separately and the combined true LKP signal. All results are scaled to a total branching ratio of 1 for the individual channel.

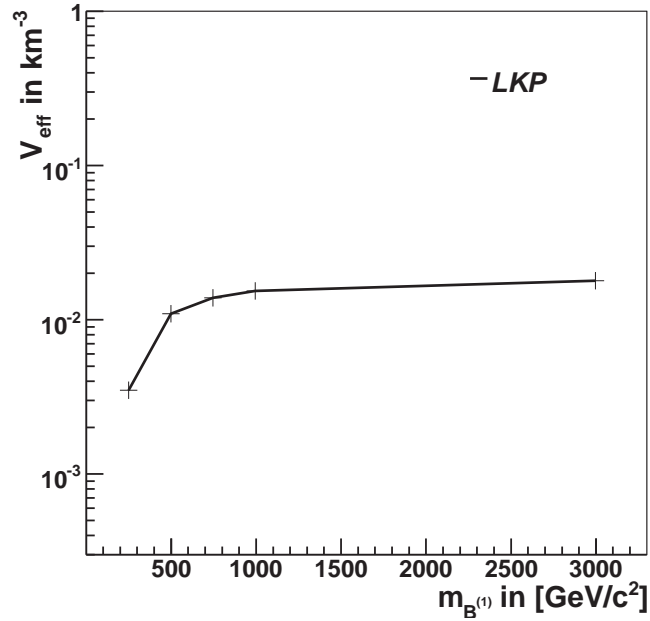


Figure A.1: Results for the final V_{eff} . This graph is plotted assuming a total branching ratio of 1 for the annihilation channels resulting in detectable neutrinos.

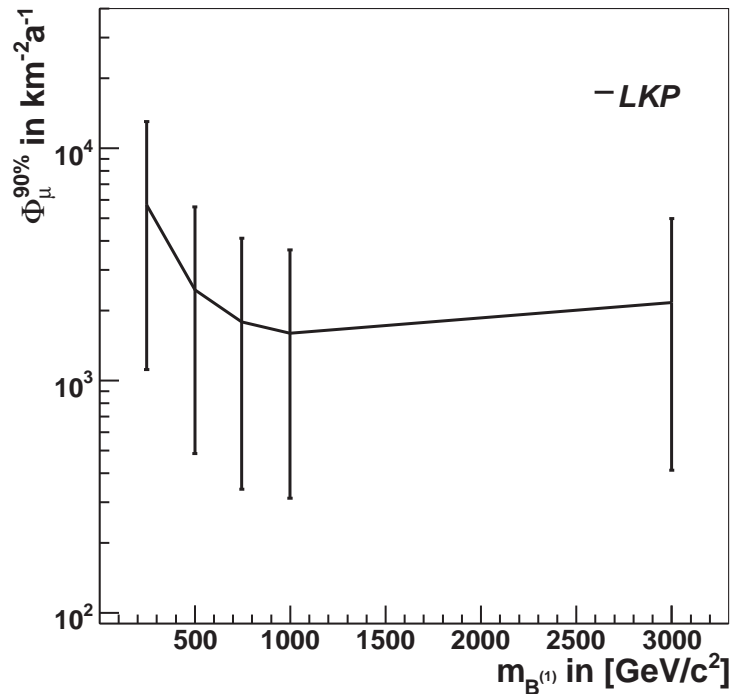


Figure A.2: Results for the minimal sensitive muon flux $\Phi_\mu^{90\%}$ of the combined detector together with the cuts applied in this work. This graph is plotted assuming a total branching ratio of 1 for the annihilation channels resulting in detectable neutrinos. The solid line, reflecting the true LKP spectrum is drawn including the systematic errors (indicated by solid vertical lines), which are estimated in section 7.4.

Appendix B

Good Run List 2007

LCspan02-008	108803	108880	109065	109174	109304
108727	108805	108881	109066	109177	109311
108729	108807	108882	109067	109178	109312
108732	108809	108883	109068	109179	109314
108734	108811	108885	109069	109180	109315
108736	108813	108886	109070	109181	109316
108738	108815	108887	109074	109182	109317
108740	108821	108888	109138	109183	109319
108742	108822	108889	109140	109184	109320
108743	108823	108890	109141	109185	109321
108745	108824	108891	109142	109269	109323
108747	108825	108892	109143	109271	109324
108749	108826	108893	109144	109272	109325
108751	108827	108894	109145	109273	109326
108753	108828	108897	109146	109275	109327
108755	108830	108898	109147	109276	109328
108757	108831	108899	109148	109277	109334
108759	108832	108902	109149	109279	109335
108761	108833	108903	109150	109281	109340
108763	108834	108905	109151	109282	109349
108765	108845	108906	109152	109283	109350
108767	108846	108907	109153	109284	109351
Alpaca010	108847	AlpacapairV012	109154	109285	109352
108768	108849	109004	109155	109286	109353
108770	Readout011	109005	109156	109288	109354
108772	108850	109006	109157	109289	109355
108774	108851	109009	109158	109290	109356
108776	108852	109011	109160	109292	109357
108778	108854	109014	109161	109294	109358
108780	108869	109015	109162	109295	109359
108782	108870	109017	109164	109296	109360
108784	108871	109018	109165	109297	109361
108786	108872	109032	109166	109298	109362
108788	108874	109033	109168	109299	
108790	108875	109034	109169	MinBiasV014	
108792	108876	109062	109170	109300	
108799	108878	109063	109171	109301	
108801	108879	109064	109173	109302	

Table B.1: *Good Run List 2007 for the combined detector. Runs marked in red are available at level0 filtering, but are identified as failed runs by the monitoring group. The different detector settings throughout the year are indicated by their names and underlined in bold.*

Bibliography

- [1] Scientific American.Com August 31, 2006 <http://www.sciam.com/article.cfm>
- [2] S. Perlmutter et al. Measurements of Ω and Λ from 42 High-Redshift Supernovae. *The Astrophysical Journal*, **517**, 565 (1991)
- [3] G. Bertone, D. Hooper and J. Silk. Particle Dark Matter: Evidence, Candidates and Constraints. *hep-ph/0404175*, [[arXiv:hep-ph/0404175v2](#)] (13 Aug 2004)
- [4] David L Wiltshire. Cosmic clocks, cosmic variance and cosmic averages *New Journal of Physics*, **Volume 9**, 377 (October 2007)
- [5] David L Wiltshire. Exact Solution to the Averaging Problem in Cosmology *Physical Review Letters*, **Vol 99** 251101 (December 2007)
- [6] D.J.Fixsens et al. The Cosmic Microwave Background Spectrum From the Full COBE FIRAS Data Set *astro-ph/0404175*, [[arXiv:astro-ph/9605054v1](#)] (10 May 1996)
- [7] C. Giunti and Ch. W. Kim. Fundamentals of Neutrino Physice and Astrophysics. *Oxford University Press* (2007)
- [8] F. Zwicky. Die Rotverschiebung von extragalaktischen Nebeln *F. Helvetica Physica Acta*, **6**, 110 (1933)
- [9] K.G. Begeman, A.H. Broeils and R.H. Sanders. *MNRAS*, **249**, 523 (1991)
- [10] C. J. Copi, D. N. Schramm, M. S. Turner. Big-Bang Nucleo-synthesis and the Baryon Density of the Universe. *Science*, **267**, 365 (1995)
- [11] M. Tegmark et al. Cosmological constraints from the SDSS luminous red galaxies. *Physical Review D*, **74**, 123507 (2006)
- [12] J. Diemand, M. Kuhlen and P. Madau. Dark Matter Substructure and gamma-ray annihilation in the Milky Way halo. *The Astrophysical Journal*, **657**, 262 (2007)
- [13] D. Hooper. Indirect Searches for Kaluza-Klein Dark Matter. *hep-ph/0409272*, [[arXiv:hep-ph/0409272v1](#)], (23 Sep 2004)

- [14] Th. Kaluza, Sitzungsber. Preuss. Akademische Wissenschaften Berlin *Math. Phys.*, **K1**, 966 (1921)
- [15] O. Klein *Z. Phys.*, **37**, 895 (1926)
- [16] T. Appelquist, H. Cheng and B. A. Dobrescu. Bounds on Universal Extra Dimensions. *Physical Review D*, **64**, 035002 (2001) [arXiv:hep-ph/0012100]
- [17] G. D. Kribs. TASI 2004 Lectures on the Phenomenology of extra Dimensions. *hep-ph*, [arXiv:hep-ph/0605325v1], (30 May 2006)
- [18] E. W. Kolb and R. Slansky. Dimensional Reduction in the early Universe: Where have the massive Particles Gone? *Physics Letters B*, **135**, 378 (1984)
- [19] K. R. Dienes, E. Dudas and T. Gherghetta. Grand Unification at Intermediate Mass Scales Through Extra Dimensions. *hep-ph/9806292*, **CERN-TH/98-100**, (June 1998)
- [20] H. Cheng, K. T. Matchev and M. Schmaltz. Radiative Corrections to Kaluza-Klein Masses *Phys. Rev.*, **D 66**, 036005 (2002)
- [21] G. Servant and T. M. P. Tait. Is the Lightest Kaluza-Klein Particle a Viable Dark Matter Candidate? *hep-ph*, [arXiv:hep-ph/0206071v2], (23 Sep 2002)
- [22] The IceCube Collaboration <http://icecube.wisc.edu/>
- [23] The Antares Collaboration <http://antares.in2p3.fr/>
- [24] D. Hooper. Indirect Searches for Kaluza-Klein Dark Matter. *hep-ph/0409272v1*, [arXiv:hep-ph/0409272v1], (23 Sep 2004)
- [25] D. Hooper and G. D. Kribs. Probing Kaluza-Klein Dark Matter with Neutrino Telescopes. *hep-ph/0208261*, [arXiv:hep-ph/0208261v3], (16 Feb 2003)
- [26] Nuclear and Particle Physics. Review of Particle Physics. *Journal of Physics*, **G33**, 445-471 (2006)
- [27] R. Gandhi, C. Quigg, M. H. Reno, and I. Sarcevic. Ultrahigh-energy neutrino interactions. *Astroparticle-Physics*, **5**, 81-110 (1996)
- [28] J.G. Learned, and K. Mannheim. HIGH-ENERGY NEUTRINO ASTROPHYSICS. *Annual Review of Nucl. Science*, **Vol. 50**, 679-749 (2000)
- [29] D. N. Perkins. Introduction to High Energy Physics. *Cambridge Univ. Press*, **4th. edition**, (2000)
- [30] W. R. Leo. Techniques for Nuclear and Particle Physics Experiments: How-to Approach. *Springer Verlag, Germany*, (1994)

- [31] P. Miocinovic. Muon Energy reconstruction in the AMANDA *Ph.D Thesis*, **Univ. of California, Berkeley**, (2001)
- [32] C.H. Wiesbusch. The detection of faint light in deep underwater neutrino telescopes. *Ph.D Thesis*, **Univ. of Aachen**, (1995)
- [33] D. Chirkin, and W. Rhode. Propagating leptons through matter with Muon Monte Carlo *hep-ph/0407075*, [**arXiv:hep-ph/0407075v2**], (19 Feb 2008)
- [34] The IceCube Collaboration (Ahrens et al). First Year Performance of the IceCube Neutrino Telescope. *astro-ph/0604450*, [**arXiv:astro-ph/0604450v2**], (25 April 2006)
- [35] The IceCube Collaboration (Ahrens et al). IceCube Project Preliminary Design Document <http://icecube.wisc.edu>
- [36] Internal IceCube wiki, maintained by Stephanie Hickford. Local Coincidence. http://wiki.icecube.wisc.edu/index.php/Local_Coincidence
- [37] G. Wikström. Methods of indirect detection of Dark Matter in IceCube *Licentiate thesis*, **Stockholm University**, (11 May 2007)
- [38] P. Lipari. Lepton spectra in the earth's atmosphere *Astroparticle Physics*, **1**, 195-227 (1993)
- [39] T. K. Gaisser, and M. Honda. Flux of Atmospheric Neutrinos *hep-ph/0203272*, [**arXiv:hep-ph/0203272v2**], (30 Mar 2002)
- [40] G. Ingelmann, and M. Thunman. High energy neutrino production by cosmic ray interactions in the Sun. *Phys. Rev.*, **D 54**, 4385 (1996)
- [41] Kenneth Greisen. End to the Cosmic-Ray Spectrum? *Phys. Rev. Lett.*, **16**, 748 - 750 (1966)
- [42] Dr Smoot's Group. Neutrino Astrophysics. <http://aether.lbl.gov/www/projects/neutrino/>
- [43] Troy D. Straszheim and the IceCube Collaboration. The IceTray offline software <http://software.icecube.wisc.edu/OFFLINE-SOFTWARE-V02-01-01/icetray/>
- [44] J. Lundberg, P. Miocinovic, T. Burgess, J. Adams, S. Hundertmark, P. Desiati, K. Woschnagg and P. Niessen. Light tracking through ice and water – Scattering and absorption in heterogeneous media with Photonics. *astro-ph/0702108v2*, [**arXiv:astro-ph/0702108v2**], (29 Aug 2007)
- [45] J. Lundberg. Photonics homepage <http://photonics.tsl.uu.se>

- [46] M. Blennow, J. Edsjö and T. Ohlsson. Neutrinos from WIMP annihilations in the Sun including neutrino oscillations. *SNOW 2006, Phys. Scr.*, **T127**, 19 (2006)
- [47] G. Wikström. WimpSim Reader: *Source Code in IceCube code repository*, <http://code.icecube.wisc.edu/svn/>, (2006)
- [48] P. Gondolo, J. Edsjö, P. Ullio, L. Bergström, M. Schelke and E.A. Baltz. DarkSUSY Computing Supersymmetric Dark Matter Properties Numerically. *JCAP*, **0407**, 008 (2004) [arXiv:astro-ph/0406204] Web: <http://www.physto.se/~edsjo/darksusy>
- [49] T. Sjöstrand, S. Mrenna and P. Skands. PYTHIA 6.4 physics and manual *JHEP*, **0605**, 026 (2006) [arXiv:hep-ph/0603175] Web: <http://www.thep.lu.se/~torbjorn/Pythia.html>
- [50] J. Edsjö. Calculation of neutrino cross sections and the nusigma neutrino-nucleon scattering Monte Carlo, nusigma-1.14 <http://copsosx03.physto.se/wimpsim/code/nucross3.pdf>, , (September 25, 2007)
- [51] M. Maltoni et al. Status of Global Fits to neutrino oscillations. *New Journal of Physics*, **6**, 122 (2004)
- [52] D. Heck et al. CORSIKA: A Monte Carlo Code to Simulate Extensive Air Showers. *Karlsruhe Report FZKA*, **6019**, (1998) Web: <http://www-ik.fzk.de/corsika/>
- [53] M. Kowalski et al. ANIS: High Energy Neutrino Generator for Neutrino Telescopes. *Comput Phys. Community*, **172**, 203 (2005) [arXiv:astro-ph/0406439v1]
- [54] G.D. Barr et al. Three-dimensional calculation of atmospheric neutrinos. *Phys. Review*, **D70**, 023006 (2004)
- [55] P. Steffen. IceJAMS- Just Another Muon Search *Source Code in IceCube code repository*, <http://code.icecube.wisc.edu/svn/>, (2006)
- [56] V. J. Stenger. Track Fitting for DUMAND-II Octagon Array, External Report *HDC-1-90 Unive. of Hawai'i*, (1990)
- [57] The AMANDA Collaboration. Muon Track Reconstruction and Data Selection Techniques in AMANDA *astro-ph/0407044v1*, [[arXiv:astro-ph/0407044v1](http://arxiv.org/abs/astro-ph/0407044v1)], (2. July 2004)
- [58] D. Pandel. Bestimmung von Wasser und Detector Parametern und Rekonstruktion von Myonen bis 100 TeV mit dem Baikal-Neutrino teleskop NT-72, Diploma thesis *Humboldt Univ. zu Berlin*, , (1996)

- [59] The Gulliver and Lilliput projects. Estimating the Angular Resolution of Tracks in Neutrino Telescopes Based on a Likelihood Analysis *Astroparticle Physics*, **25**, 220-225 (April 2006)
- [60] R. Brun and F. Rademakers. ROOT-v5.18.00 An Object Oriented Data Analysis Framework *Phys. Res.*, **A 389**, 81-86 (1997) <http://root.cern.ch/>
- [61] (TMVA-v3.9.4) Toolkit for Multivariate Data Analysis with ROOT. <http://tmva.sourceforge.net/>
- [62] G. J. Feldmann, and R. D. Cousins. Unified approach to the classical statistical analysis of small signals. *Phys. Rev.*, **D57**, 7 (1998)
- [63] G. C. Hill, and K. Rawlins. Unbiased cut selection for optimal upper limits in neutrino detectors: the model rejection potential technique *Astrop. Phys.*, **19**, 393-402 (2003)
- [64] M. Blennow, J. Edsjo, T. Ohlsson. Neutrinos from WIMP Annihilations Obtained Using a Full Three-Flavor Monte Carlo Approach *JCAP*, **010**, 21 (2008)
- [65] J. Edsjö, WimpSim Neutrino Monte Carlo. <http://www.physto.se/~edsjo/wimpsim/>
- [66] Lepton neutrino hadronic shower flux conversion. <http://copsosx03.physto.se/cgi-bin/edsjo/wimpsim/flxconv.cgi>
- [67] spase & AMANDA collaborations. Calibration and Survey of AMANDA with the spase Detectors. *Nucl. Instr. and Meth.*, **A522**, 347 (2004)
- [68] T. Burgess. A Search for Solar Neutralino Dark Matter with the amanda-II Neutrino Telescope. *Doctoral Dissertation*, **Stockholm University**, (2008)
- [69] Y. S. Minaeva. Search for Neutrino Dark Matter with the AMANDA-II Neutrino Telescope *Doctoral Dissertation*, **Stockholm University**, (2004)
- [70] G. Wikström. 2007 IC22 WIMP Analysis, and Unblinding Proposal <http://www.physto.se/~wikstrom/icecube/ic22/index.html>, (2008)
- [71] H.C. Cheng, J.L. Feng, and K. T. Matchev. Kaluza-Klein Dark Matter *Phys. Rev. Letters*, **89**, 21 (18. November 2002)
- [72] R. Gaitskell and J. Filippini. Direct Detection of WIMP Dark Matter, Sensitivity Plots. An interactive plotter for experimental and theoretical data. <http://dmttools.berkeley.edu/limitplots/>
- [73] C. P. de los Heros. Proceedings of the first Workshop on Exotic Physics with Neutrino Telescopes EPNT06 *Uppsala, Sweden*, [**arXiv:astro-ph/0701333v2**], (12 Jan 2007)

- [74] EDELWEISS Collaboration. Improved exclusion limits from the EDELWEISS WIMP search *Physics Letters B*, **545**, 43-49 (2002)
- [75] S. Desai, et al. The Super-Kamiokande Collaboration. Search for Dark Matter WIMPs using upward through-going muons in Super-Kamiokande. *Phys. Rev.*, **D60**, 109901 (2004)
- [76] J. Angle et al. The XENON Collaboration. First Results from the XENON10 Dark Matter Experiment at the Gran Sasso National Laboratory. *Phys. Rev. Lett.*, **100**, 021303 (2008) [arXiv:0706.0039]
- [77] G. Wikström. Evaluations of DeepCore.
<http://www.physto.se/~wikstrom/icecube/deepcore/>

Statement

With the submission of this diploma thesis I testify that I have written it independently and did not use other sources than the cited references.

Munich, 14 July

Matthias Danninger